
DEEP GENERATIVE SPATIOTEMPORAL ENGRESSION FOR PROBABILISTIC FORECASTING OF EPIDEMICS

PREPRINT

Rajdeep Pathak¹  Tanujit Chakraborty^{1*}

¹SAFIR, Sorbonne University Abu Dhabi, UAE

¹Sorbonne Center for Artificial Intelligence, Sorbonne University, Paris, France
{rajdeep.pathak, tanujit.chakraborty}@sorbonne.ae

ABSTRACT

Accurate and reliable forecasting of epidemic incidences is critical for public health preparedness, yet it remains a challenging task due to complex nonlinear temporal dependencies and heterogeneous spatial interactions. Often, point forecasts generated by spatiotemporal models are unreliable in assigning uncertainty to future epidemic events. Probabilistic forecasting of epidemics is therefore crucial for providing the best or worst-case scenarios rather than a simple, often inaccurate, point estimate. We present deep spatiotemporal engression methods to generate accurate and reliable probabilistic forecasts on low-frequency epidemic datasets. The proposed methods act as distributional lenses, and out-of-sample probabilistic forecasts are generated by sampling from the trained models. Our frameworks encapsulate lightweight deep generative architectures, wherein uncertainty is quantified endogenously, driven by a pre-additive noise component during model construction. We establish geometric ergodicity and asymptotic stationarity of the spatiotemporal engression processes under mild assumptions on the network weights and pre-additive noise process. Comprehensive evaluations across six epidemiological datasets over three forecast horizons demonstrate that the proposal consistently outperforms several temporal and spatiotemporal benchmarks in both point and probabilistic forecasting. Additionally, we explore the explainability of the proposal to enhance the models' practical application for informed, timely public health interventions. The `stengression` Python package provides an implementation of our proposed approaches.

Keywords Epidemics · Probabilistic forecasting · Spatiotemporal engression · Neural networks · Asymptotic stationarity

1 Introduction

Epidemics have persistently posed one of the most serious threats to global public health, societal stability, and economic sustainability. Throughout history, infectious diseases have periodically swept through populations, leaving behind devastating consequences. For instance, the bubonic plague or Black Death in the 14th century claimed nearly one-third of Europe's population ([Glatter and Finkelman \[2021\]](#)). The Great Influenza epidemic or Spanish Flu of 1918 ([Trilla et al. \[2008\]](#)) infected about one-third of the world's population and caused over 50 million deaths. More recent events such as the 2003 SARS epidemic ([Cherry and Krogstad \[2004\]](#)), the 2014-2016 West African Ebola outbreak ([Houlihan et al. \[2017\]](#)), the 2015 Zika epidemic ([Ferguson et al. \[2016\]](#)), and the COVID-19 pandemic ([Chakraborty and Ghosh \[2020\]](#)) have demonstrated that even in an era of advanced science and communication, humanity remains vulnerable to fast-evolving pathogens that can overwhelm healthcare systems, disrupt economies, and destabilize societies. The increasing pace of globalization, climate change, and human mobility has intensified the spatial reach and frequency of such outbreaks. Hence, epidemic forecasting is not merely an academic pursuit but an indispensable component of public health preparedness and response.

*Corresponding author.

The imperative to anticipate epidemic dynamics has driven the development of forecasting models essential for strategic resource allocation and the formulation of interventions. A plethora of forecasting models are available in the literature, and a vast majority of them can generate point forecasts based on the data of past epidemic incidence cases (Benidis et al. [2022], Panja et al. [2023]). However, public health officials can take better decisions with an estimate of the uncertainty in the forecasted target rather than solely relying on point forecasts (Ioannidis et al. [2022]). Due to this, probabilistic forecasts are more desirable for high-stakes decision making (Rumack et al. [2022]). A probabilistic forecast quantifies predictive uncertainty by providing prediction intervals or selected quantiles around a point forecast, capturing the range of plausible future outcomes. Epidemics are driven by highly nonlinear interacting processes, including pathogen mutation rates, spatiotemporal mobility patterns, and rapid shifts in human behavior following non-pharmaceutical interventions. It is therefore important for an epidemic forecaster (also for a wide variety of other applications) to produce spatiotemporal probabilistic forecasts, to inform public health officials for tailored responses to outbreaks of infectious disease.

Previous works on epidemic modeling generally bifurcate into mechanistic (compartmental) frameworks, which simulate the physical laws of disease transmission (Kermack and McKendrick [1927]), and phenomenological approaches, which utilize historical data to forecast future trends without explicit biological assumptions. Early approaches to forecast epidemics were predominantly temporal, focusing on time series forecasting of incidence data (Benvenuto et al. [2020], Ospina et al. [2023]). More recently, machine learning techniques such as Recurrent Neural Networks (RNNs) and Long Short-Term Memory (LSTM) networks (Hochreiter and Schmidhuber [1997]) have emerged as powerful nonlinear approximators capable of learning intricate patterns from epidemiological data (Datilo et al. [2019], Chimmula and Zhang [2020], Kara [2021]). However, most of these methods are suitable for producing point forecasts, which is just a scalar value for each target and has no measure of uncertainty. Model-agnostic methods such as conformal prediction (Shafer and Vovk [2008]) are often used to create post-hoc prediction intervals from a trained time series model (Barman et al. [2025], Panja et al. [2026]). However, they require exchangeability of data and rely on holdout calibration set for calculation of non-conformity scores. Current probabilistic time series models often depend on parametric distributions (Salinas et al. [2020], Herzen et al. [2022]), discrete conditional percentiles via quantile regression (Jensen et al. [2022]), or computationally exhaustive Markov Chain Monte Carlo (MCMC) sampling for Bayesian inference (Klein et al. [2023]). Crucially, these purely temporal architectures overlook the spatial factors of epidemic spread. By isolating single geographical units, they fail to model the complex diffusion of diseases across networks, effectively ignoring the spatial transmission pathways.

To overcome this limitation, recent works are focused on spatiotemporal modeling, which accounts for temporal dynamics under spatial dependence. Spatiotemporal models represent the epidemic process as a dynamic system evolving over a network or a spatial lattice. The Space-Time Autoregressive Moving Average (STARMA) model (Pfeifer and Deutch [1980]) provides a statistical framework for modeling spatiotemporal dependence, expressing the current state of a region as a function of its own past and that of its spatial neighbors. More recently, Graph Neural Networks (GNNs) have gained significant traction in modeling and forecasting epidemics (Liu et al. [2024]) and spatial time series in general. Models such as Graph-Structured RNN (GSRNN; Li et al. [2019]), Cross-location Attention based GNN (Cola-GNN; Deng et al. [2020]), and Epi-GNN (Xie et al. [2022]) have combined GCNs and RNNs for effectively forecasting infectious diseases such as the COVID-19 and influenza. However, a significant portion of current spatiotemporal literature focused on epidemics (Barman et al. [2025], Deng et al. [2020], Qiu et al. [2024]) remains restricted to point estimation. The existing probabilistic models in the spatiotemporal domain are predominantly tailored for climate and energy sectors, where high-frequency, high-volume data (e.g., sub-hourly intervals) are readily available. Notable examples include Spatio-temporal Neural Network (STNN) for wind-speed forecasting (Liu et al. [2020]), DiffSTG for traffic and air quality modeling (Wen et al. [2023]), and spatiotemporal echo-state networks (STESNs) for wind power prediction (Huang et al. [2022]). Conversely, epidemic datasets typically exhibit much lower temporal granularity - ranging from daily or weekly to monthly observations, and are often constrained by a paucity of data points. Moreover, the operational utility of models like DiffSTG and STESN is constrained by the high computational overhead of their sampling mechanisms, which renders the generation of forecast ensembles computationally expensive during inference. Thus, there is a critical need for spatiotemporal models for data-driven epidemic forecasting that performs well on low-frequency data, are lightweight, and offer model-intrinsic uncertainty quantification through a probabilistic framework.

This work focuses on building spatiotemporal frameworks based on deep generative architectures that can produce accurate and reliable probabilistic forecasts for low-frequency epidemic datasets. This is done via integrating the idea of pre-additive noise mechanism, a spatial module, temporal module (with LSTM as the base model), and energy score loss. Traditional post-additive noise models ($Y = g(X) + \eta$, discussed in Sec. 3) generally focus on the conditional mean estimation, operating under the restrictive assumption that error distributions are symmetric (typically Gaussian) and centered around the mean. Engression, a neural network-based distributional regression methodology (Shen and Meinshausen [2025]), vouches for pre-additive noise models and learns to sample from the training data

distribution via a transformation of a simple distribution. Building on this, we introduce three probabilistic frameworks for spatiotemporal forecasting of epidemics, namely *Multivariate Engression Network* (MVEN), *Graph Convolutional Engression Network* (GCEN), and *Spatio-Temporal Engression Network* (STEN). The MVEN architecture is purely temporal and based on LSTM-engression (Kraft et al. [2026]), comprising LSTM networks processing noise-perturbed inputs. In contrast, STEN and GCEN are probabilistic spatiotemporal frameworks that can capture both temporal dynamics and spatial correlation structures. STEN’s spatial module relies on prior knowledge of the spatial connectivity in terms of a distance-based weights matrix. This approach produces interpretable spatial embeddings by capturing the linear trajectory among the spatial locations. The graph convolution operations of GCEN offers higher flexibility in modeling the dynamic, complex, nonlinear spatial dependencies across several spatial units.

Our proposed models function as distributional lenses; multiple ‘plausible’ multi-step-ahead forecast trajectories can be sampled from the trained models to form a forecast ensemble, thereby quantifying the uncertainty of the disease dynamics. By integrating uncertainty quantification as an intrinsic feature of the architectures, the proposed frameworks provide prediction intervals (PIs) without the need for independent, model-agnostic wrappers like conformal prediction, or the prohibitive computational overhead inherent in Bayesian posterior sampling. Moreover, generating PIs directly from the forecast ensemble eliminates the necessity for external calibration using a holdout set. We further investigate the asymptotic properties of the spatiotemporal engression processes by formulating them as closed-loop Markov chains, demonstrating their geometric ergodicity and asymptotic stationarity under mild assumptions. This theoretical guarantee yields significant practical implications for reliable long-term epidemic forecasting. Finally, we conduct an explainability analysis by understanding the internal model dynamics; we explore how the latent stochasticity induced by the pre-additive noise propagates to generate a diverse ensemble of plausible forecast trajectories. Additionally, the spatial architecture of the proposed STEN inherently offers interpretability by explicitly quantifying the contribution of individual spatial lags to local epidemic incidence. This yields practical and actionable evidence for public health interventions, clearly separating the influence of ongoing local patterns from cross-regional spread.

To validate our models, we consider six diverse epidemic datasets consisting of airborne and vector-borne infectious diseases with daily, weekly, and monthly granularities. Each spatiotemporal dataset consists of disease incidence cases for all the states or prefectures for the respective countries with varying sample sizes. The proposed deep spatiotemporal engression methods, viz. MVEN, GCEN, and STEN are applied to these low-frequency datasets to produce multi-step-ahead probabilistic forecasts. These lightweight architectures are compared to existing spatiotemporal probabilistic architectures such as Fast Gaussian Process (GpGp), DiffSTG, and STESN, that are extremely computationally heavy. When compared to other distinct temporal and spatiotemporal state-of-the-art methods using multiple point and probabilistic performance metrics for different forecast horizons, the proposals either outperform the benchmarks, or remain highly competitive. Thus, deep spatiotemporal engression offers model-intrinsic uncertainty quantification on spatiotemporal data with theoretical guarantees, and consistently improves not only the prediction intervals, but also predictive accuracy for epidemic datasets.

The remainder of this paper is structured as follows. Sec. 2 discusses the probabilistic forecasting problem for an epidemic data and motivates the use of pre-additive noise for time series forecasting. Sec. 3 provides an overview of the engression framework. Sec. 4 details the proposed methodologies, including the spatiotemporal problem formulation and the MVEN, GCEN, and STEN architectures. Theoretical results regarding geometric ergodicity and asymptotic stationarity are established in Sec. 5.1 and verified through numerical simulations in Sec. 5.3. The experimental evaluation and comparative analyses on real-world epidemic datasets are presented in Sec. 6, followed by an analysis of model explainability in Sec. 7. In Sec. 8, we conclude the paper, highlighting the limitations of the proposal and directions for future research.

2 Motivating Example

Our work is motivated by real-world epidemic datasets where point forecasts are often inadequate to help decision makers in public health (Ioannidis et al. [2022]). To illustrate, we consider weekly dengue incidence data in Guainia, Colombia (Clarke et al. [2024]). To motivate the problem of probabilistic forecasting, we review a simple univariate time series forecasting task, where only the past lag $y_{t-1} \in \mathbb{R}$ is used to forecast the value for the next time-step, $y_t \in \mathbb{R}$ for the dengue dataset. One can observe the dependence of y_t on y_{t-1} using a lag plot, which is the visualization of y_t against y_{t-1} . A vertical slice of this plot at any fixed lag value y_{t-1} empirically reveals the conditional distribution of the future state y_t . Due to external factors driving the process, we may observe different future values for the same past lag. For example, in an epidemic process, the number of epidemic cases can jump from $y_{t-1} = 20$ to $y_t = 30$ in a given week, $y_t = 50$ in another week considering disease spread due to its contagious nature, and may dip to $y_t = 10$ in another, assuming effective control measures are imposed over time to curb the disease spread. Fig. 1 (A) illustrates this, with a lag plot on the dengue data of Guainia. With 835 observations in the range of $[0, 22]$ each, it is clear (in

fact, follows from the pigeonhole principle; [Rebman \[1979\]](#)) that (at least) one past lag (y_{t-1}) value will correspond to multiple values for the future observation y_t .

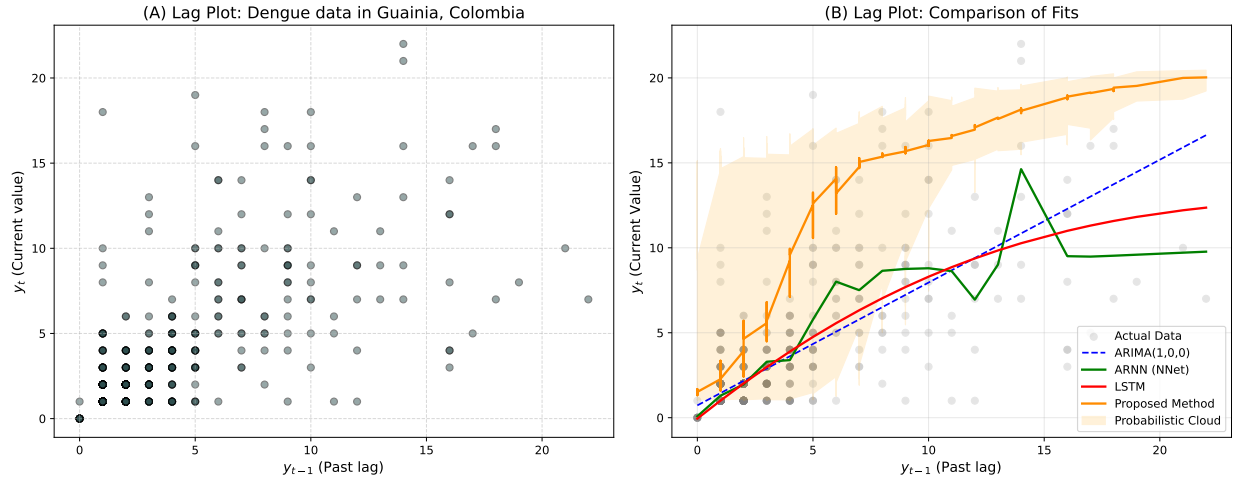


Fig. 1: (A) Lag plot y_t vs. y_{t-1} for weekly dengue data observed in Guainia, Colombia, and (B) ARIMA(1,0,0), ARNN, LSTM, and proposed MVEN (and a generated probabilistic cloud based on the proposal) fits on the data.

In standard forecasting frameworks, including classical AR(p) and autoregressive neural networks (ARNN), the modeling paradigm typically assumes a post-additive noise structure, formulated as $y_t = f(y_{t-1}) + \eta_t$. This formulation inherently imposes a rigid constraint on the predictive distribution. It presumes that the stochasticity of the system is invariant across the state space, manifesting as a symmetric, often Gaussian, error distribution centered around the conditional mean. Consequently, such models effectively enforce an uncertainty profile where the shape of the distribution remains constant regardless of the input. This limitation is visually evident in the inability of the mean fit to encompass the dispersion of incidence data (Fig. 1 (B)). In contrast, this work motivates a pre-additive noise mechanism: $y_t = f(y_{t-1} + \eta_t)$. By injecting stochasticity prior to the non-linear transformation f , the model empowers the neural network to function as a complex distributional lens by actively propagating noise through the model's non-linear layers. The resulting 'probabilistic cloud' (see Fig. 1 (B)) thus provides a rigorous approximation of the predictive density, ensuring that generated trajectories remain dynamically plausible and structurally consistent with the underlying physical process. Consequently, this work introduces spatiotemporal methods with a pre-additive noise structure, designed to generate reliable and accurate probabilistic forecasts for low-frequency epidemic datasets.

3 Background

Engression is a deep generative distributional regression methodology, developed recently by [Shen and Meinshausen \[2025\]](#). The primary goal of engression is to estimate the full conditional distribution of a target variable given a set of covariates, denoted as $P(Y|X = x)$, rather than focusing only on a specific functional such as the conditional mean or median. It is a generative model, meaning it can produce new samples from the fitted conditional distribution. A central innovation of the engression framework is its use of a pre-additive noise model (pre-ANM). For regression problems, this model assumes that noise η is added directly to the covariates X before they are passed through a nonlinear transformation g , represented as $Y = g(X + \eta)$. This is in contrast to the conventional post-additive noise model (post-ANM), where noise is added after the transformation, i.e., $Y = g(X) + \eta$. To learn the conditional distribution, the model is trained by minimizing a loss function based on the energy score (discussed in Sec. 4.4). The energy score is a proper scoring rule ([Gneiting and Raftery \[2007\]](#)) that evaluates the quality of probabilistic forecasts. The combination of a pre-ANM with a distributional fit provides engression with a significant advantage in extrapolation. By modeling the entire distribution, the fitted function is better constrained outside the support of the training data, addressing a notorious challenge in nonlinear regression where models like tree ensembles tend to predict constants and standard neural networks behave uncontrollably ([Shen and Meinshausen \[2025\]](#)).

The engression framework has been implemented for environmental time series forecasting. [Kraft et al. \[2026\]](#) integrated engression with LSTM networks to create an LSTM-engression model for rainfall-runoff prediction. An engression-based time series model can produce an entire ensemble of plausible future trajectories, providing a rich and

dynamically consistent characterization of predictive uncertainty. The pre-additive structure is what makes engression models generative. To generate a single sample from the trained model, one simply samples a random noise vector η from a pre-defined distribution (e.g., uniform or Gaussian), computes the perturbed input $X' = X + \eta$, and then passes X' through the learned function g to get a sample output $Y_{sample} = g(X')$. By repeating this process with different noise samples, one can generate an entire ensemble of plausible outputs, effectively sampling from the learned distribution. This work builds deep spatiotemporal engression frameworks for probabilistic forecasting of multivariate time series under spatial dependencies. Our proposed models produce model-intrinsic prediction intervals for forecasting spatiotemporal epidemic series.

4 Proposed Methodology

Spatiotemporal data, which archives measurements across both geographical locations and temporal intervals, is fundamental to the study of time series forecasting. This research focuses on predicting epidemic disease incidences, addressing the critical challenge of jointly modeling two distinct phenomena: the inherent temporal dependencies evident in historical cases data and the complex spatial relationships that exist between administrative regions, such as states or prefectures. The contagious nature of diseases like tuberculosis, COVID-19, dengue, and influenza-like illnesses necessitates this dual focus, as the transmission dynamics in one region are often influenced by its geographical neighbors. Assuming that there are N administrative regions, the spatiotemporal dataset is a three dimensional tensor, $\mathcal{Y} \in \mathbb{R}^{T \times N \times D}$, which encapsulates measurements of D features across N discrete spatial nodes over a sequence of T time-steps. An individual element in the tensor \mathcal{Y} , denoted as $y_{t,n,d}$, represents the value of the d^{th} feature ($d \in \{1, 2, \dots, D\}$), recorded at the n^{th} spatial node ($n \in \{1, 2, \dots, N\}$), at time-step t ($t \in \{1, 2, \dots, T\}$). A slice along the first axis at time t , denoted as \mathbf{Y}_t , is an $N \times D$ matrix representing a snapshot of all features across all nodes at that specific moment. In the current context, we have $D = 1$ as we are interested in modeling only the epidemic incidence cases for multiple spatial nodes; however, the setting can be generalized, where the last dimension can accommodate multiple target variables to forecast along with exogenous covariates (see Sec. 8). Then, given the historical epidemic data $\mathcal{Y} = \{\mathbf{Y}_t\}_{t=1}^T \in \mathbb{R}^{T \times N \times 1}$ up to time T , the aim is to design a model that can produce multi-step ahead forecasts for q future time-steps ($q \in \mathbb{N}$): $\hat{\mathcal{Y}} = \left\{ \hat{\mathbf{Y}}_t \right\}_{t=T+1}^{T+q} \in \mathbb{R}^{q \times N \times 1}$, where each $\hat{\mathbf{Y}}_t \in \mathbb{R}^N$ is the prediction for incidence cases at the t^{th} time-step across all N nodes.

In this section, we present three spatiotemporal probabilistic forecasting frameworks, motivated by the idea of engression (developed for regression examples in [Shen and Meinshausen \[2025\]](#)) and LSTM-engression (developed for temporal forecasting in [Kraft et al. \[2026\]](#)).

4.1 Graph Convolutional Engression Network

We propose Graph Convolutional Engression Network (GCEN), a deep learning architecture designed for probabilistic spatiotemporal forecasting, particularly on data exhibiting graphical or lattice structures. Its design, inspired by Spatio-Temporal Graph Convolutional Networks ([Yu et al. \[2018\]](#)), integrates spatial feature extraction with a probabilistic temporal forecasting mechanism. This creates a principled separation between the modeling of spatial dependencies and temporal dynamics. GCEN is made up of three key components: a spatial embedding function f_{GCN} , latent noise injection, and a temporal evolution function f_{Temp} . A visual illustration of the GCEN architecture is presented in [Fig. 13](#) in [Appendix G](#).

The spatial module of the GCEN architecture comprises GCNs, that functions as a spatial feature extractor. It learns a spatially-aware representation of the system's state at each point in time. The underlying spatial relationships between the nodes are encoded in a static adjacency matrix, $A \in \mathbb{R}^{N \times N}$, which represents an undirected graph. First, the weighted Haversine distance (d_{ij}) between the geographical locations of nodes i and j with latitude-longitude pair (lat_i, lon_i) and (lat_j, lon_j) , respectively, is computed as ([Panja et al. \[2026\]](#)):

$$d_{ij} = 2R \sin^{-1} \left(\sqrt{\sin^2 \left(\frac{lat_i - lat_j}{2} \right) + \cos(lon_i) \cos(lon_j) \sin^2 \left(\frac{lon_i - lon_j}{2} \right)} \right), \quad (1)$$

where R represents the radius of the Earth. The spatial interdependencies among the network nodes are formally characterized by a weighted adjacency matrix A , wherein the pairwise similarity a_{ij} between distinct nodes is derived from a thresholded Gaussian kernel:

$$a_{ij} = \exp \left(-\frac{d_{ij}^2}{\tilde{\sigma}^2} \right), \text{ when } i \neq j \text{ and } \exp \left(-\frac{d_{ij}^2}{\tilde{\sigma}^2} \right) \geq \epsilon,$$

where the hyperparameters $\tilde{\sigma}^2$ and ϵ serve as critical regulators of the matrix's distribution and sparsity, respectively. This Gaussian radial basis function effectively establishes a finite interaction radius; specifically, if the distance between two nodes exceeds the threshold $\sqrt{-\tilde{\sigma}^2 \ln \epsilon}$, the edge weight is truncated to zero, and thus no connectivity is considered between those nodes. By filtering out negligible dependencies, this approach ensures a localized and computationally efficient graph structure that accurately reflects the underlying spatial topology of the system.

The spatial module operates in a sequence-to-sequence paradigm, utilizing a window of p lagged time steps, $\mathbf{Y}_{t-p+1:t}$, as the input at time t . At each time-step t , it processes the feature slice $\mathbf{Y}_{t-p+1:t} \in \mathbb{R}^{p \times N \times D}$ and the adjacency matrix A , to produce a latent embedding $\mathbf{Z}_{t-p+1:t} \in \mathbb{R}^{p \times N \times D'}$, where D' is the dimension of the node features in the embedding domain. This transformation can be formally expressed as:

$$\mathbf{Z}_{t-p+1:t} = f_{GCN}(\mathbf{Y}_{t-p+1:t}, A; \Theta_{GCN}),$$

where Θ_{GCN} represents the learnable weight matrix of the GCN layers. The function f_{GCN} is typically a composition of graph convolution operations that propagate and transform node features across the graph, allowing each node's resulting representation to be informed by its local spatial context. To maintain localization and efficiency, GCNs approximate polynomial filters using a first-order Chebyshev expansion (Kipf [2016]). For an input signal $\mathbf{Y}_t \in \mathbb{R}^{N \times D}$, the graph convolution is defined as:

$$\mathbf{Y}'_t = \theta_0 \mathbf{Y}_t + \theta_1 \left(\frac{2L}{\lambda_{\max}} - I_N \right) \mathbf{Y}_t,$$

where θ_0, θ_1 are shared filter weights, L is the graph Laplacian, λ_{\max} is its largest eigenvalue, and I_N is the identity matrix of order N . By stacking K such layers and adhering to a neural message passing framework (Gilmer et al. [2017]), the model generates spatial embeddings. Each node i updates its representation $h_t^{i,(k)}$ through 1-hop mean aggregation of its neighborhood $\mathcal{N}(i)$ and its own prior state (Panja et al. [2026]):

$$\begin{aligned} h_t^{i,(0)} &= Y_t^i \\ h_t^{i,(k)} &= f_t^{(k)} \left(\Theta_t^{(k)} \frac{\sum_{j \in \mathcal{N}(i)} h_t^{j,(k-1)}}{|\mathcal{N}(i)|} + B_t^{(k)} h_t^{i,(k-1)} \right), \quad k = 1, \dots, K \\ Z_t^i &= \text{Dense} \left(h_t^{i,(K)} \right), \end{aligned}$$

where $f_t^{(k)}$ is the activation function and $\Theta_t^{(k)}$ and $B_t^{(k)}$ are learnable parameters. The final spatiotemporal representation Z_t^i is produced by a fully connected layer following the K^{th} iteration. The resultant embedding matrix, $\mathbf{Z}_t = [Z_t^1, \dots, Z_t^N]^\top \in \mathbb{R}^{N \times D'}$, thereby captures information from the $(K-1)$ -order neighborhood of each node combined with their temporal information.

A core architectural element, adapted from the engression methodology, is the injection of stochastic noise into the learned latent space, that helps the model to produce probabilistic forecasts. For each spatial embedding \mathbf{Z}_τ within the p -length historical sequence ($\tau = \{t-p+1, \dots, t\}$), a corresponding noise tensor $\boldsymbol{\eta}_\tau \in \mathbb{R}^{N \times D'}$ is sampled from a pre-defined distribution (e.g., standard Gaussian or Uniform). This noise is additively combined with the deterministic embedding to yield a perturbed latent state:

$$\mathbf{Z}'_\tau = \mathbf{Z}_\tau + \boldsymbol{\eta}_\tau.$$

This perturbation is applied to all time-steps in the lookback window, producing a stochastic embedding sequence, $\mathbf{Z}'_{t-p+1:t}$. An alternative injection method involves sampling a noise tensor $\boldsymbol{\eta}_\tau \in \mathbb{R}^{N \times D_{\text{noise}}}$ and concatenating it with the embedding, yielding a perturbed representation $\mathbf{Z}'_\tau \in \mathbb{R}^{N \times (D' + D_{\text{noise}})}$. For ease of presentation, this text will primarily assume the additive method; however, our model implementation flexibly supports both approaches. The choice of the noise distribution is data dependent; we empirically observe that datasets depicting (local) periodicity are better modeled using uniform distribution, whereas for more noisy spatiotemporal datasets, Gaussian distribution provides better coverage during prediction.

The sequence of perturbed spatial embeddings, $\mathbf{Z}'_{t-p+1:t}$, serves as the input to the second module: a temporal model. In the temporal module of GCEN, we use an LSTM network, following prior works (Panja et al. [2026], Kraft et al. [2026]). This module is responsible for capturing the complex temporal dynamics of the system's evolution and generating probabilistic forecasts through the noise injection mechanism. Hence, the temporal evolution governed by the function f_{Temp} and parameterized by Θ_{Temp} is given by:

$$\mathcal{H}_\tau = f_{Temp}(\mathbf{Z}'_\tau, \mathcal{H}_{\tau-1}; \Theta_{Temp}) = \text{LSTM}(\mathbf{Z}'_\tau, \mathcal{H}_{\tau-1}; \Theta_{\text{LSTM}}),$$

where $\mathcal{H}_\tau \in \mathbb{R}^{N \times D_{hidden}}$ denotes the hidden state of the temporal model at time-step $\tau = \{t - p + 1, \dots, t\}$ for all N nodes, and Θ_{LSTM} is the learnable weight matrix in LSTM. The final multi-step forecast for a future horizon of q steps (starting from time-step t), denoted by $\hat{\mathbf{Y}}_{t+1:t+q} \in \mathbb{R}^{q \times N \times D}$, is then generated from the final hidden state of the sequence via a fully connected (dense) output layer:

$$\hat{\mathbf{Y}}_{t+1:t+q} = \text{Dense}(\mathcal{H}_t).$$

The process from the noise sampling step is repeated M times, each with an independently drawn noise sequence $\{\boldsymbol{\eta}^{(j)}\}_{j=1}^M$ to generate an ensemble of M distinct future trajectories $\{\hat{\mathbf{Y}}_{t+1:t+q}^{(j)}\}_{j=1}^M$. This ensemble constitutes the model's probabilistic forecasts, where each $\hat{\mathbf{Y}}_{t+1:t+q}^{(j)}$ represents a sample forecast (trajectory) drawn from its learned distribution. The GCEN model can be viewed as a generative process, mapping a historical input sequence consisting of values for p time-steps, $\mathbf{Y}_{t-p+1:t}$, the graph structure A , and a sequence of M noise samples $\{\boldsymbol{\eta}_{t-p+1:t}^{(j)}\}_{j=1}^M$ to an ensemble of M forecast trajectories $\{\hat{\mathbf{Y}}_{t+1:t+q}^{(j)}\}_{j=1}^M$. A forward pass is the process of passing input data through a neural network's layers - input, hidden, and output - to generate a prediction. A single (j^{th}) forward pass of the GCEN model (pseudo code presented in Algorithm 1 in Appendix B) produces a single forecast trajectory

$$\hat{\mathbf{Y}}_{t+1:t+q}^{(j)} = f_{GCEN} \left(\mathbf{Y}_{t-p+1:t}, A, \boldsymbol{\eta}_{t-p+1:t}^{(j)} \right),$$

and this process is repeated M times (M forward passes) to generate M forecast trajectories for the same forecast horizon, which constitute the probabilistic forecast ensemble. If the model is trained with the entire available historical data $\mathbf{Y}_{1:T}$, then a forecast for the next q time-steps can be generated using the historical sequence $\mathbf{Y}_{T-p+1:T}$ as input to the trained model. The resulting forecast ensemble $\{\hat{\mathbf{Y}}_{T+1:T+q}^{(j)}\}_{j=1}^M$ facilitates the derivation of point forecast trajectory (e.g., the ensemble median), as well as the estimation of prediction intervals through specific quantiles. A detailed discussion about estimation of the model parameters using energy score-based backpropagation is given in Sec. 4.4.

4.2 Spatio-Temporal Engression Network

The STEN architecture incorporates spatial dependencies based on a predefined spatial weights matrix, motivated by the idea of Spatiotemporal Autoregressive Moving Average (STARMA; Pfeifer and Deutch [1980]) model. By adapting this framework into a differentiable neural layer, it becomes possible to explicitly define the nature of spatial dependencies, such as the influence of second-order neighbors or the relative importance of different spatial scales. The STEN model comprises two sequential modules - a STAR-layer: STAR-inspired spatial embedding layer (see Rathod et al. [2018] for details), and a probabilistic engression-LSTM layer.

The first module of the STEN architecture is a neural layer designed to directly implement the spatial aggregation principles of STAR, instead of the graph convolution operations used in GCEN. At each time-step τ , the STAR-layer receives the matrix of node features, $\mathbf{Y}_\tau \in \mathbb{R}^{N \times D}$, and a pre-computed, static $N \times N$ spatial weights matrix W . The Haversine distance d_{ij} is computed between each node using (1), and the weights matrix is constructed as $W_{ij} = \frac{1}{d_{ij}^\alpha}$, where α is the decay parameter which can be tuned using a holdout validation set.

The core operation of the layer is to compute a set of spatially lagged feature representations. For a pre-defined maximum spatial lag L , the layer calculates the sequence of matrices $\{\mathbf{Y}_\tau, W\mathbf{Y}_\tau, W^2\mathbf{Y}_\tau, \dots, W^L\mathbf{Y}_\tau\}$. Each matrix $W^l\mathbf{Y}_\tau \in \mathbb{R}^{N \times D}$ represents the features of the l^{th} -order neighbors aggregated to each node. These computations can be performed very efficiently, especially if W is a sparse matrix. The layer then combines these multi-scale spatial representations through a learnable, weighted aggregation. The final spatial embedding for time τ , denoted by $\tilde{\mathbf{Z}}_\tau \in \mathbb{R}^{N \times D'}$, is computed as:

$$\tilde{\mathbf{Z}}_\tau = \text{ReLU} \left(\sum_{l=0}^L (W^l \mathbf{Y}_\tau) \Phi_l \right), \quad (2)$$

where each $\Phi_l \in \mathbb{R}^{D \times D'}$ is a learnable weight matrix, effectively acting as a linear transformation specific to the l^{th} spatial lag and D' is the dimensionality of the learned spatial embedding. This formulation allows the model to learn the relative importance of information from different spatial scales when creating the final embedding. The STAR-layer is applied to a batch of input sequences of length p (for each batch) in each forward pass, transforming the raw input

sequence $\mathbf{Y}_{t-p+1:t}$ into a sequence of rich spatial embeddings, $\tilde{\mathbf{Z}}_{t-p+1:t}$. Each embedding $\tilde{\mathbf{Z}}_\tau$ ($\tau = \{t-p+1, \dots, t\}$), encodes not just the features at time τ , but also the learned multi-scale spatial context surrounding each node.

The spatial embeddings from the STAR-layer are then perturbed with noise before being passed to the temporal module. The complete, end-to-end process for a single forward pass of the STEN model is detailed in Algorithm 2 (Appendix B). It generates one sample trajectory $\hat{\mathbf{Y}}^{(j)}$ using the following sequence of operations. At each time-step t , the STAR-layer uses the input sequence $\mathbf{Y}_{t-p+1:t} \in \mathbb{R}^{p \times N \times D}$ and $W \in \mathbb{R}^{N \times N}$ to generate the spatial embedding sequence $\tilde{\mathbf{Z}}_{t-p+1:t} \in \mathbb{R}^{p \times N \times D'}$. A random noise tensor $\boldsymbol{\eta}$ is sampled from a pre-determined distribution and the embedding sequence is perturbed as

$$\tilde{\mathbf{Z}}'_{t-p+1:t} = \tilde{\mathbf{Z}}_{t-p+1:t} + \boldsymbol{\eta}.$$

The perturbed sequence is processed by the temporal module, an LSTM network, to generate a hidden state tensor $\mathcal{H}_{t-p+1:t} \in \mathbb{R}^{p \times N \times D_{hidden}}$, similar to GCEN. Finally, a single dense layer acts as the forecasting head, which takes the final hidden state of the temporal module as input and maps it to the desired output shape for a q -step-ahead forecast horizon:

$$\hat{\mathbf{Y}}_{t+1:t+q} = \text{Dense}(\mathcal{H}_t) \in \mathbb{R}^{q \times N \times D}.$$

To generate probabilistic forecasts, the entire process from the noise sampling step is repeated M times with different noise samples $\{\boldsymbol{\eta}^{(j)}\}_{j=1}^M$ to create an ensemble of trajectories $\{\hat{\mathbf{Y}}_{t+1:t+q}^{(j)}\}_{j=1}^M$. As discussed in Sec. 4.1, the parameter estimation procedure is detailed in Sec. 4.4.

4.3 Multivariate Engression Network

MVEN is a multivariate time series framework based on engression. It utilizes a generative approach characterized by the direct injection of stochastic noise into the input features instead of spatial embeddings, which are subsequently processed by LSTM layers for forecasting. LSTM-engression, proposed by Kraft et al. [2026], maps the LSTM hidden states to a single value and uses softplus activation to transform them into the positive domain. In contrast, MVEN utilizes a fully connected layer after the LSTM network as a forecasting head, which maps the LSTM hidden states into the final forecast shape. MVEN uses energy score loss (see Sec. 4.4) during backpropagation for model parameter estimation, and the forecast ensemble consisting of M trajectories is generated as a stacked tensor of shape (M, q, N, D) . Formulated as a sequence-to-sequence framework similar to GCEN and STEN, a single forward pass of MVEN ingests a historical observation tensor $\mathbf{Y}_{t-p+1:t} \in \mathbb{R}^{p \times N \times D}$ and generates a q -step ahead forecast $\hat{\mathbf{Y}}_{t+1:t+q} \in \mathbb{R}^{q \times N \times D}$ for all the nodes (see Algorithm 3 in Appendix B). As a purely (multivariate) temporal framework, this model can be viewed as a baseline for evaluating spatiotemporal architectures, as it skips spatial dependencies, thereby treating the nodes as independent, to isolate the contribution of temporal dynamics in the dataset. MVEN will be particularly useful for spatiotemporal forecasting problems where locational information are seldom available, such as movements of robots while performing manipulation tasks.

4.4 Optimization

The training dataset $\mathcal{D} = \{(\mathbf{Y}_{t-p+1:t}, \mathbf{Y}_{t+1:t+q})\}$, $p \leq t \leq T - q$, is constructed by taking sequential overlapping slices from the original multivariate time series, where each input sample $\mathbf{Y}_{t-p+1:t} \in \mathbb{R}^{p \times N \times D}$ and its corresponding ground truth $\mathbf{Y}_{t+1:t+q} \in \mathbb{R}^{q \times N \times D}$ are temporally contiguous. The proposed models are trained by minimizing the empirical energy score loss (Gneiting and Raftery [2007]), a proper scoring rule that evaluates the quality of the entire predictive distribution against the ground truth observation. The loss function comprises two terms: an accuracy term and a sharpness term, which allows the model to learn not just a single ‘best guess’ prediction, but the entire probable distribution of future states, while still ensuring the average prediction is accurate. This is similar to the idea of balancing exploration and exploitation in reinforcement learning (Sutton et al. [1998]). For a single slice of ground truth sequence and its prediction (an ensemble of M forecasts), the accuracy term is given by:

$$\mathcal{L}_{accuracy} = \frac{1}{M} \sum_{j=1}^M \left\| \mathbf{Y}_{t+1:t+q} - \hat{\mathbf{Y}}_{t+1:t+q}^{(j)} \right\|_2^\beta,$$

and the sharpness term is given by

$$\mathcal{L}_{sharpness} = \frac{1}{2M(M-1)} \sum_{j=1}^M \sum_{k=1}^M \left\| \hat{\mathbf{Y}}_{t+1:t+q}^{(j)} - \hat{\mathbf{Y}}_{t+1:t+q}^{(k)} \right\|_2^\beta,$$

where $\mathbf{Y}_{t+1:t+q}$ is the ground truth (observed target vector) during training, $\widehat{\mathbf{Y}}_{t+1:t+q}^{(j)}$ is the in-sample predicted j^{th} trajectory (an independent sample drawn from the model's predicted distribution), M is the total number of forecasts in the forecast ensemble ($j = 1, 2, \dots, M$), and the exponent $\beta \in (0, 2)$. The empirical energy score (ES) loss computes the loss between all (batches of) sequences of ground truth observations and in-sample predictions in \mathcal{D} as follows:

$$\mathcal{L}_{ES} = \frac{1}{|\mathcal{D}|} \sum_{i=1}^{|\mathcal{D}|} \left[\frac{1}{M} \sum_{j=1}^M \left\| \mathbf{Y}_i - \widehat{\mathbf{Y}}_i^{(j)} \right\|_2^\beta - \frac{1}{2M(M-1)} \sum_{j=1}^M \sum_{k=1}^M \left\| \widehat{\mathbf{Y}}_i^{(j)} - \widehat{\mathbf{Y}}_i^{(k)} \right\|_2^\beta \right], \quad (3)$$

where \mathbf{Y}_i is the ground truth sequence of length q (second element of the i^{th} tuple in \mathcal{D}) and $\widehat{\mathbf{Y}}_i^{(j)}$ is its predicted value.

We empirically illustrate the benefits of ES loss over standard data loss such as mean squared error (MSE) in probabilistic forecasting using a toy example in Appendix C. Since the loss function (3) is differentiable almost everywhere, standard backpropagation is used to optimize the objective and learn the weights of the proposed models. The full end-to-end training loop of the proposed models is given in Algorithm 4 in Appendix B.

Remark 1. Model selection among the proposed frameworks is contingent upon the specific trade-off between interpretability and the complexity of spatial dependencies inherent in the data. STEN is preferable when interpretability is paramount, as its predefined weights matrix elucidate specific spatial lag contributions (see Sec. 7.2). Conversely, GCEN is superior for capturing complex, nonlinear spatial heterogeneity through data-driven graph convolutions. Finally, MVEN is optimal for datasets with weak or noisy spatial signals, as it isolates temporal dynamics without imposing potentially confounding spatial structures.

5 Geometric Ergodicity and Asymptotic Stationarity

5.1 Theoretical Results

Geometric ergodicity is a fundamental property for evaluating the stability and predictive reliability of stochastic forecasting models. It confirms that the underlying Markov chain converges to a unique stationary distribution at an exponential rate (Meyn and Tweedie [2012]). This geometric convergence implies that the influence of initial conditions and distant past observations decays exponentially fast. Establishing this property is important, as it ensures the model is stable and its forecasts are asymptotically independent of arbitrary starting conditions, which is a prerequisite for reliable and statistically consistent long-term prediction. For the theoretical studies, we consider a closed-loop (i.e., no exogenous covariates) and 1-step recurrent (input and output sequence lengths $p, q = 1$) setup without loss of generality, for simplicity. The results can be extended for a setup with $p, q > 1$ and exogenous inputs. We first prove that such a temporal network process driven by pre-additive noise is geometrically ergodic, following Zhao et al. [2020]. Using that, we then proceed to formally demonstrate that the proposed MVEN, GCEN, and STEN processes, when formulated as homogeneous Markov chains in their closed-loop forms, are geometrically ergodic.

To establish the geometric ergodicity and asymptotic stationarity of the engression processes, we first show that they are irreducible, meaning that all the states in the Markov chain communicate with each other. The concept of irreducibility is essential when considering the structure of the Markov chain for any nonlinear time series model. By constructing a suitable non-negative continuous function and verifying Tweedie's drift criterion (Tweedie [1983]) along with irreducibility, we ensure the existence of a unique invariant distribution to which the process converges geometrically fast, thus establishing ergodicity. Before stating the main results, we formally define the notions of irreducibility and geometric ergodicity.

Definition 1 (Irreducibility). Let λ_k be the Lebesgue measure on the state space $\mathcal{S} \subseteq \mathbb{R}^k$. The Markov chain $\{S_t\}$ is λ_k -irreducible if, for every initial state $s \in \mathcal{S}$ and every set $A \subseteq \mathcal{S}$ with $\lambda_k(A) > 0$, there exists an integer $n \geq 1$ such that $P^n(s, A) > 0$. This means any set A with positive measure can eventually be reached from any starting state s .

Definition 2 (Geometric ergodicity). Let \mathcal{B} and λ denote the Borel σ -field and Lebesgue measure, respectively. A Markov chain $\{S_t\}$ is called geometrically ergodic if there exists a probability measure Π on a probability triple $(\mathcal{S}, \mathcal{B}, \lambda)$ and a constant $\rho > 1$ such that $\lim_{n \rightarrow \infty} \rho^n \|\mathbb{P}^n(s, \cdot) - \Pi(\cdot)\| = 0$, $\forall s \in \mathcal{S}$ where $\|\cdot\|$ denotes the total variation norm. Then, we say the distribution of S_t converges to Π and S_t is asymptotically stationary.

Denote by $\mathcal{S} \subseteq \mathbb{R}^k$ the state space, \mathcal{B}^k the class of Borel sets on \mathbb{R}^k , and λ_k the Lebesgue measure on $(\mathbb{R}^k, \mathcal{B}^k)$. Let $\{\mathbf{y}_t\}_{t \in \mathbb{N}}$ be the target sequence, where $\mathbf{y}_t \in \mathbb{R}^N$. Let $\mathbf{h}_t \in \mathbb{R}^{N'}$ denote general hidden states, so that $k = N + N'$. We define a network process with pre-additive noise and no exogenous inputs (for simplicity), where the input at the t^{th} step is the previous observed value \mathbf{y}_{t-1} . Let $\boldsymbol{\eta}_t$ be the noise added to the input at the t^{th} time-step. To establish irreducibility, without loss of generality, we add a vanishingly small noise $\boldsymbol{\xi}_t$ to the hidden states. This can be formulated

as a homogeneous Markov chain with transition function \mathcal{F} :

$$\begin{pmatrix} \mathbf{y}_t \\ \mathbf{h}_t \end{pmatrix} = \mathcal{F} \left(\begin{pmatrix} \mathbf{y}_{t-1} \\ \mathbf{h}_{t-1} \end{pmatrix} + \begin{pmatrix} \boldsymbol{\eta}_t \\ \boldsymbol{\xi}_t \end{pmatrix} \right),$$

or equivalently,

$$S_t = \mathcal{F}(S_{t-1} + \boldsymbol{\varepsilon}_t), \quad (4)$$

where $S_t = (\mathbf{y}_t^\top, \mathbf{h}_t^\top)^\top \in \mathbb{R}^k$ denotes the current state, $\boldsymbol{\eta}_t \in \mathbb{R}^N$ is a random noise vector sampled from a pre-determined distribution with pdf $f_{\boldsymbol{\eta}}(\cdot)$, and $\boldsymbol{\varepsilon}_t = (\boldsymbol{\eta}_t^\top; \boldsymbol{\xi}_t^\top)^\top$, where $\boldsymbol{\xi}_t \in \mathbb{R}^{N'}$, $\boldsymbol{\xi}_t \sim \mathcal{N}(\mathbf{0}_{N'}, \sigma^2 I)$, where σ_{ii}^2 are vanishingly small positive scalars.

To prove the geometric ergodicity of the temporal network process with pre-additive noise, we impose the following assumptions:

- (A1) The joint density function of $\boldsymbol{\eta}_t$ is continuous and positive everywhere.
- (A2) For any initial state $\mathbf{s} \in \mathbb{R}^k$ and any Borel set $A \in \mathcal{B}^k$ with positive Lebesgue measure ($\lambda_k(A) > 0$), the set $\{(\boldsymbol{\eta}, \boldsymbol{\xi}) \in \mathbb{R}^k : \mathcal{F}(\mathbf{s} + (\boldsymbol{\eta}, \boldsymbol{\xi})) \in A\}$ has positive Lebesgue measure.
- (A3) $\mathbb{E}(\|\boldsymbol{\eta}_t\|^c) < \infty$ for some $c \geq 1$.

(A1) and (A3) are standard assumptions in Zhao et al. [2020], that can be satisfied by, for example, standard Gaussian noise; hence, these assumptions trivially hold for $\boldsymbol{\xi}_t$. (A3) assumes that the noise term $\boldsymbol{\eta}_t$ has a finite c^{th} -order moment. In our case, it suffices to consider a finite first moment. (A2) is necessary to prove irreducibility in our pre-additive setup, which means that for any state $\mathbf{s} \in \mathbb{R}^k$ and any Borel set A with $\lambda_k(A) > 0$, the image set $\{\mathcal{F}(\mathbf{s} + (\boldsymbol{\eta}, \boldsymbol{\xi})) : (\boldsymbol{\eta}, \boldsymbol{\xi}) \in \mathbb{R}^k\}$ must intersect A such that the preimage of this intersection has a positive Lebesgue measure in \mathbb{R}^k .

The theorem below states that a recurrent network process with pre-additive noise is geometrically ergodic under the assumptions (A1)-(A3) stated above. The proof is given in Appendix A, and involves showing that the Markov chain $\{S_t\}$ is irreducible, followed by establishing Tweedie's drift criterion (Tweedie [1983]).

Theorem 1. *Suppose that Assumptions (A1)-(A3) hold. If there exist real numbers $a \in (0, 1)$ and b such that $\|\mathcal{F}(z)\| \leq a\|z\| + b$, then the pre-additive recurrent network process defined in (4) is geometrically ergodic.*

Next, we proceed to prove that closed-loop 1-step recurrent GCEN, STEN, and MVEN processes are geometrically ergodic under mild assumptions. The output of the GCEN and STEN processes are determined by an LSTM network, which processes (perturbed) spatial embeddings as input. The hidden unit computations in an LSTM network involve several gating operations, as outlined below.

$$\begin{aligned} \mathbf{f}_t &= \sigma(W_{fh}\mathbf{h}_{t-1} + W_{fy}\mathbf{y}_{t-1} + b_f) && \text{(forget gate)} \\ \mathbf{i}_t &= \sigma(W_{ih}\mathbf{h}_{t-1} + W_{iy}\mathbf{y}_{t-1} + b_i) && \text{(input gate)} \\ \mathbf{o}_t &= \sigma(W_{oh}\mathbf{h}_{t-1} + W_{oy}\mathbf{y}_{t-1} + b_o) && \text{(output gate)} \\ \tilde{\mathbf{c}}_t &= \tanh(W_{ch}\mathbf{h}_{t-1} + W_{cy}\mathbf{y}_{t-1} + b_c) && \text{(candidate cell state)} \\ \mathbf{c}_t &= \mathbf{i}_t \odot \tilde{\mathbf{c}}_t + \mathbf{f}_t \odot \mathbf{c}_{t-1} && \text{(cell state)} \\ \mathbf{h}_t &= \mathbf{o}_t \odot \tanh(\mathbf{c}_t) && \text{(hidden state)} \\ \mathbf{z}_t &= g(W_{zh}\mathbf{h}_t + b_z) && \text{(output)} \end{aligned}$$

where, $\mathbf{y}_0 = \mathbf{0}_N$, $\mathbf{h}_0 = \mathbf{0}_{N'}$, $\mathbf{y}_t, \mathbf{z}_t \in \mathbb{R}^N$, $\mathbf{h}_t, \mathbf{c}_t, \tilde{\mathbf{c}}_t, \mathbf{o}_t, \mathbf{i}_t, \mathbf{f}_t \in \mathbb{R}^{N'}$ for $t = \{1, \dots, T\}$, g, σ , and \tanh are respectively an elementwise output function and the elementwise sigmoid and hyperbolic tangent functions, and \odot is the elementwise (Hadamard) product. The hidden weight matrices $W_{fh}, W_{ih}, W_{oh}, W_{ch} \in \mathbb{R}^{N' \times N'}$, input weight matrices $W_{fy}, W_{iy}, W_{oy}, W_{cy} \in \mathbb{R}^{N' \times N}$, output weight matrix $W_{zh} \in \mathbb{R}^{N \times N'}$, and bias terms $b_f, b_i, b_o, b_c \in \mathbb{R}^{N'}$ and $b_z \in \mathbb{R}^N$. Let $f_{spatial} : \mathbb{R}^N \rightarrow \mathbb{R}^N (\mathbb{R}^{1 \times N \times 1} \rightarrow \mathbb{R}^{1 \times N \times 1})$ denote the transformation that maps the input sequence to spatial embeddings, which is achieved by the graph convolution operations in GCEN and STAR-layer in STEN. Hence, the GCEN and STEN processes can be defined as:

$$\begin{pmatrix} \mathbf{y}_t \\ \mathbf{h}_t \\ \mathbf{c}_t \end{pmatrix} = \mathcal{F}_{LSTM} \left(\begin{pmatrix} f_{spatial}(\mathbf{y}_{t-1}) \\ \mathbf{h}_{t-1} \\ \mathbf{c}_{t-1} \end{pmatrix} + \begin{pmatrix} \boldsymbol{\eta}_t \\ \boldsymbol{\xi}_t \\ \boldsymbol{\psi}_t \end{pmatrix} \right), \quad (5)$$

where \mathcal{F}_{LSTM} denotes the transition function of the LSTM network and $\psi_t \in \mathbb{R}^{N'}$ is a vanishingly small noise component added to the cell state, whose distribution follows that of ξ_t . To prove that the simplified versions of GCEN and STEN processes are geometrically ergodic, we make another set of assumptions as follows.

- (A4) The noise-perturbed output generated by the spatial function $f_{spatial}$ is bounded everywhere: $f_{spatial}(\mathbf{x}) + \boldsymbol{\eta} \in B_{\infty}^{N'}$.
- (A5) $\widetilde{M} := \sup_{x \in B_{\infty}^{N'}} \|g(W_{zh}x + b_z)\|_1 < \infty$.
- (A6) $\sigma(\|W_{fh}\|_{\infty} + \|W_{fy}\|_{\infty} + \|b_f\|_{\infty}) \leq a$ for some $a < 1$.

Assumption (A4) can be made true, for instance, with bounded activation functions such as tanh and sigmoidal, used inside $f_{spatial}$ (GCN or STAR layers). Assumption (A5) ensures that the ℓ_1 -norm of the final output from the process is finite, given that the hidden state value is in $B_{\infty}^{N'}$, which denotes the N' -dimensional ℓ_{∞} -ball. Assumption (A6) means that the forget gate is contractive with respect to the matrix ℓ_{∞} -norm, denoted by $\|\cdot\|_{\infty}$ and defined as $\|P_{m \times n}\|_{\infty} = \max_{1 \leq i \leq m} \sum_{j=1}^n |p_{ij}|$. Now, we state the main results for geometric ergodicity and asymptotic stationarity of the closed-loop spatiotemporal engression Markov processes.

Theorem 2. *Suppose that Assumptions (A1)-(A6) hold. Then the GCEN and STEN processes defined in (5) are geometrically ergodic.*

Corollary 1 (Asymptotic stationarity). *Let $S_t = (\mathbf{y}_t, \mathbf{h}_t, \mathbf{c}_t)$ be the GCEN or STEN process satisfying the conditions of Theorem 2, then $\{S_t\}$ is asymptotically stationary.*

Remark 2. If the spatial function $f_{spatial}$ is the identity function, then (5) represents the MVEN process.

Corollary 2. *Under assumptions (A1)-(A6), the MVEN process is geometrically ergodic and asymptotically stationary.*

Remark 3. 1. Corollaries 1 and 2 are a direct consequence of Theorem 2.

2. For theoretical analysis, we consider perturbing the hidden and cell state dynamics of the system with vanishingly small noise to ensure the required Markov chain properties; however, in the practical implementation of our models, no noise is explicitly added to the hidden states.

5.2 Practical Implications of Theoretical Results

The spatiotemporal results have significant practical implications for the application of MVEN, GCEN, and STEN in forecasting because they provide essential theoretical guarantees for these complex and nonlinear deep generative models. Irreducibility confirms that the models are not confined to a limited portion of the state space; it guarantees that the chain can, with positive probability, transition from any state (e.g., a low endemic period) to any other plausible epidemic state (e.g., a high-incidence outbreak) in a finite number of steps, during epidemic forecasting. This is crucial for any model that must capture sudden surges in disease forecasting. Theoretical results on geometric ergodicity establish that the autonomous versions of the models are stable and do not show ‘explosive behavior’ over time. This ensures that the influence of initial conditions and distant past observations decays exponentially fast, meaning long-term forecasts are not unduly biased by historical data from an arbitrary starting point. For public health agencies, these properties provide critical assurance and reliability of the forecasts generated by the proposed methods. They confirm that generated probabilistic forecasts are not artifacts of an unstable process, but rather the outputs of reliable, stable, and well-behaved systems, making them trustworthy tools for real-time decision-making and policy planning.

5.3 Simulation Study

To empirically verify the theoretical stability guarantees of the closed-loop processes, we modeled the generative processes as autonomous, homogeneous Markov chains. For each process, we conducted simulations consisting of 200 independent trials to empirically verify the asymptotic stationarity and geometric ergodicity. The 1-step recurrent GCEN and STEN architectures were instantiated with GCN and STAR spatial modules featuring hidden dimensions of $D_{hidden} = 16, 32, \text{ and } 64$, integrated with an LSTM cell for the temporal module. The MVEN architecture was instantiated with an LSTM cell, with the same settings for hidden units. For each trial in GCEN, we generated a random graph with a random number of spatial nodes N from 10 to 60. For STEN, we instantiated the $N \times N$ spatial weights matrix (where $N \in \{10, \dots, 60\}$) with random entries such that the diagonal elements are zero and each row sums to one. The hidden and cell states \mathbf{h}_0 and \mathbf{c}_0 , of shape $N \times D_{hidden}$, in all cases, were initialized with zeros. The input state vector \mathbf{Y}_0 of shape $1 \times N \times 1$ (the first dimension corresponds to time-step, and the last to that of input dimension) was also initialized with zeros. The noise injection was carried out with a standard Gaussian noise. The models were executed in a closed-loop autoregressive mode over a horizon of $T = 500$ time steps for each trial, after a burn-in period of 50.

The following analysis details the simulation results of the closed-loop GCEN process; results for the STEN and MVEN processes are substantially similar and are deferred to Appendix G (Figures 14 and 15, respectively). First, we verify the marginal asymptotic stationarity for each spatial node. We applied the Kwiatkowski-Phillips-Schmidt-Shin (KPSS) test to the generated trajectories of all N nodes, at a significance level of 0.05. Unlike standard unit root tests, the KPSS null hypothesis posits stationarity; thus, we aggregated the ‘pass rate’ defined as the proportion of nodal time series where the null hypothesis could not be rejected ($p > 0.05$), i.e., the proportion of time series that are stationary. We obtained pass rates of 92.8%, 92.9%, and 92.3%, respectively for GCEN models simulated with 16, 32, and 64 hidden dimensions, signifying strong evidence of asymptotic stationarity. In Fig. 2, panels (A)-(C) present the simulated values of the time series for an example node (the last node in the last trial) for each model (hidden dimension setting). Panels (D)-(F) illustrate the distribution of p -values of the KPSS test, with the dashed red vertical line denoting $p = 0.05$.

To verify geometric ergodicity, we employed a synchronous coupling strategy. In each of the 200 trials, two independent chains were initialized at divergent states, $\mathbf{S}_0 = (\mathbf{Y}_0, \mathbf{h}_0, \mathbf{c}_0)$ and $\mathbf{S}'_0 = (\mathbf{Y}'_0, \mathbf{h}'_0, \mathbf{c}'_0)$, but were driven by an identical sequence of noise realizations $\{\boldsymbol{\eta}_t\}_{t \geq 1}$. We monitored the Euclidean distance between the trajectories as additive norm, $d_t = \|\mathbf{Y}_t - \mathbf{Y}'_t\|_2 + \|\mathbf{h}_t - \mathbf{h}'_t\|_2 + \|\mathbf{c}_t - \mathbf{c}'_t\|_2$. Ideally, for a geometrically ergodic system, this distance should contract exponentially, adhering to $d_t \leq C\zeta^t$ for some $\zeta < 1$. We quantified this by fitting a linear regression to the logarithmic distance, $\ln(d_t) \approx \gamma t + \kappa$, and reporting the mean decay rate $\bar{\gamma}$ across all trials. The regression window was restricted to the regime where $d_t > 10^{-6}$ (an arbitrarily chosen small float) to avoid artifacts arising from floating-point machine precision floors. The resulting negative slopes of the mean logarithmic distance, $\bar{\gamma} \approx -0.56, -0.55$, and -0.54 , respectively, for the models with hidden dimensions 16, 32, and 64, confirms exponential contraction before the coupled chains effectively merge (Fig. 2 (J)-(L) and (G)-(I)), which indicates that the system forgets initial conditions at a geometric rate, validating the contractive drift of the GCEN process. Simulation analyses indicate that data generated from the closed-loop spatiotemporal engression processes exhibit asymptotic stationarity and temporal stability, lacking explosive divergence. Nevertheless, in practical applications, models trained on finite samples yield robust forecasts across both stationary and nonstationary time series dynamics.

6 Application to Real-World Epidemic Datasets

This section outlines the experimental framework for evaluating the proposed models on real-world epidemic datasets.

6.1 Datasets

To ensure a rigorous and comprehensive evaluation, the proposed models were benchmarked on six different spatiotemporal datasets encompassing diverse diseases and geographical regions. They vary in sizes, granularity, and number of nodes, as detailed in Table 1. We are particularly interested about five diseases characterized by diverse etiological agents and transmission mechanisms. Dengue is a vector-borne disease with a very high fatality rate (2-5%; Sah et al. [2023]); Tuberculosis (TB) is a bacterial infection, whereas COVID-19, influenza-like illnesses (ILI), and varicella (chickenpox) are viral pathogens. The latter four diseases spread predominantly through direct anthropogenic pathways, including aerosolized respiratory droplets, person-to-person contact, and fomite contact. Therefore, models that integrate human mobility and the underlying spatial topology of the region can produce near real-time risk maps and case projections.

Table 1: Datasets used in this study.

Country	Disease	No. of observations	No. of locations	Frequency	Time frame	Reference
Japan	Tuberculosis (TB)	216	47	Monthly	January 1998-December 2015	Sumi and Kobayashi [2019]
China	Tuberculosis (TB)	60	31	Monthly	January 2014-December 2018	Ma and Fan [2023]
USA	Influenza-Like Illnesses (ILI)	328	50	Weekly	October 2010-January 2017	CDC ²
Belgium	COVID-19	776	11	Daily	September 2020-October 2022	Epistat ³
Colombia	Dengue	835	33	Weekly	January 2007-December 2022	Clarke et al. [2024]
Hungary	Chickenpox	522	20	Weekly	January 2005-December 2014	Rozemberczki et al. [2021a]

Fig. 3 presents the spatial distribution of incidence cases at all locations for different datasets considered in this study, utilizing a color gradient to represent the mean case counts at each node. The global statistical properties of each dataset such as mean, standard deviation, range, skewness, kurtosis, stationarity tests, and nonlinearity tests are presented in Tables 3-8 in Appendix D, along with a brief discussion on the temporal properties. The historical data of incidence cases at four random nodes of each dataset is presented in Fig. 16 in Appendix G.

²<https://gis.cdc.gov/grasp/fluview/fluportaldashboard.html>

³<https://epistat.sciensano.be/covid/>

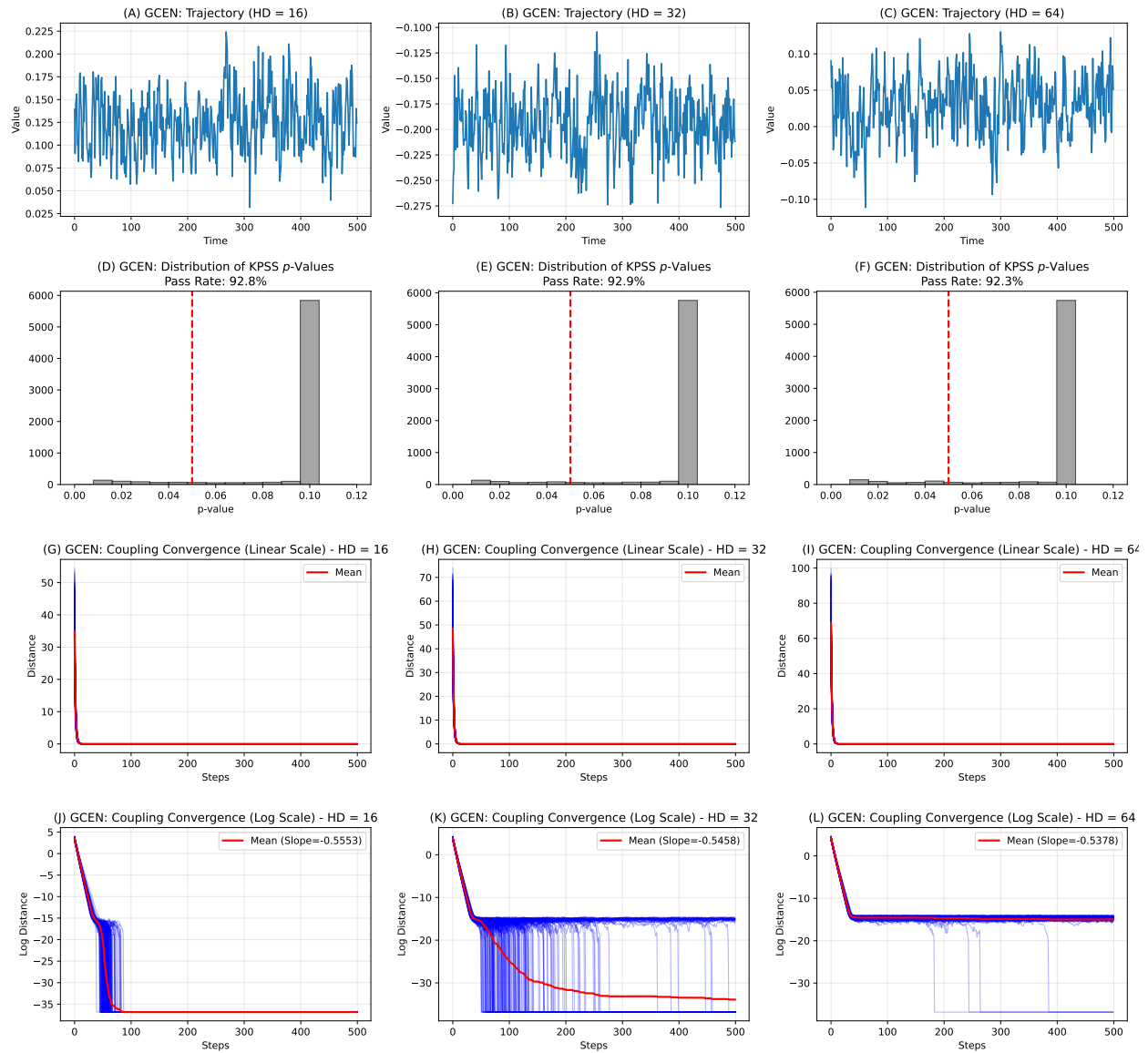


Fig. 2: Simulation results for GCEN: empirical verification of (marginal) asymptotic stationarity and geometric ergodicity of the GCEN process through simulations for 500 time steps and 200 trials.

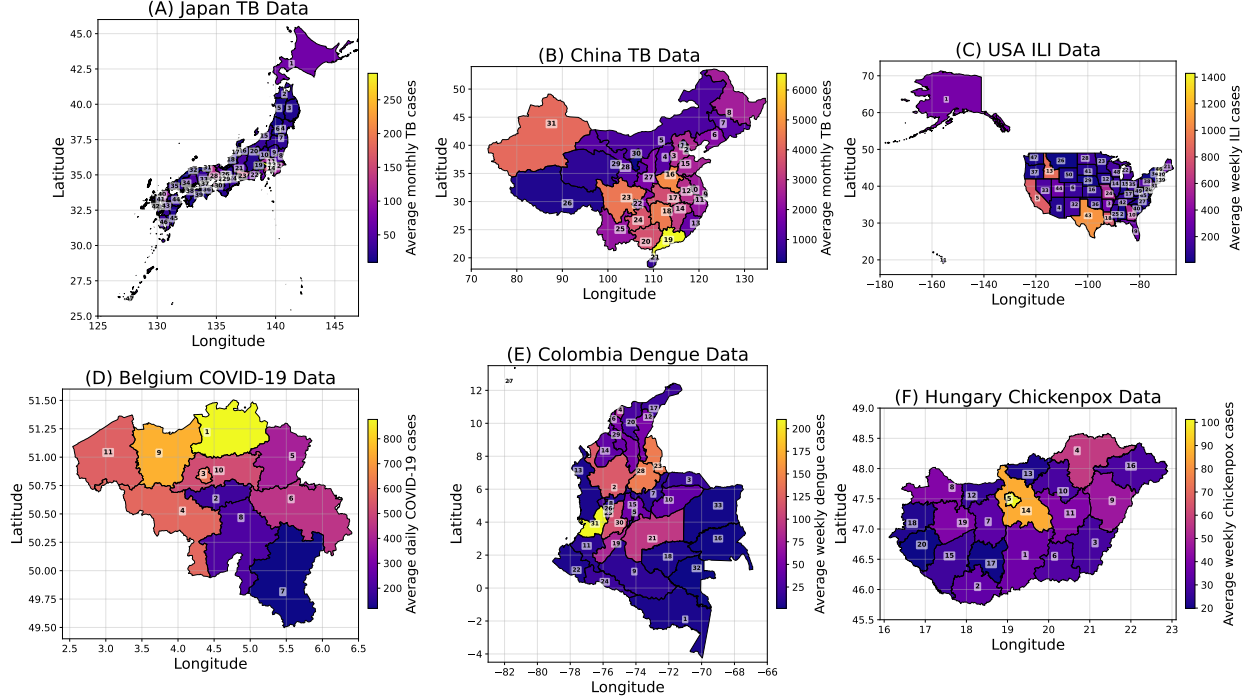


Fig. 3: Geographical maps of the countries under study: (A) Japan, (B) China, (C) USA, (D) Belgium, (E) Colombia, and (F) Hungary - illustrating the mean incidence cases at each labeled node (see Tables 3-8 in Appendix D for the corresponding node names). The territorial boundaries of the countries are shown for illustrative purposes only, without implying any political assertions.

6.1.1 Spatial Autocorrelation

We study the evolution of spatial autocorrelation over time for all the datasets. Spatial autocorrelation measures the extent to which a variable's geographic distribution deviates from spatial randomness. Moran's I is the definitive global statistic for this assessment, yielding a standardized coefficient typically ranging from -1 to $+1$. Positive values signify spatial clustering, i.e., nodes with high (low) values are surrounded by neighbors that also have high (low) values; negative values denote dispersion, and values near the expected null indicate randomness (Moraga [2023]). The statistic is defined as:

$$I = \frac{n \sum_i \sum_j w_{ij} (Y_i - \bar{Y})(Y_j - \bar{Y})}{(\sum_{i \neq j} w_{ij}) \sum_i (Y_i - \bar{Y})^2}$$

where n is the number of spatial nodes, Y_i is the observed value in region i , and \bar{Y} is the global mean. The connectivity between units is defined by a weights matrix $W \in \mathbb{R}^{N \times N}$ (where $w_{ii} = 0$), constructed as in STEN (see Sec. 4.2). To capture the dynamic behavior of spatiotemporal systems, calculating Moran's I for each discrete interval reveals the temporal evolution of spatial structure. As illustrated in Fig. 4, this approach identifies critical transitions, showing how clustering patterns emerge, stabilize, or fragment over time. Each plot reveals a unique spatial pattern for the respective region and disease. Japan (TB) exhibits a gradually intensifying positive spatial autocorrelation from 1998 to 2016, while China (TB) maintains a lower, stable clustering pattern from 2014 to 2019. Conversely, the USA (ILI) shows significant volatility, with Moran's I frequently fluctuating between positive clustering and spatial randomness. Belgium (COVID-19) displays oscillatory cycles, where autocorrelation peaks during infection waves and dips into negative territory during troughs. Colombia (dengue) is characterized by high-intensity clustering spikes, with deep spatial dispersion (negative Moran's I) in majority of the period (2007-2022). Finally, Hungary (chickenpox) demonstrates extreme volatility, with rapid transitions between strong clustering and dispersion throughout the decade.

The analysis suggests a significant neighborhood effect in disease transmission. Accurate probabilistic forecasting of such infectious diseases is of our main interest since it is often difficult for the government and public health officials to know the exact disease mutation and transmission mechanism, and anticipate outbreaks while taking decisions. Data-driven statistical and machine learning systems can work with temporal dynamics in the presence of spatial

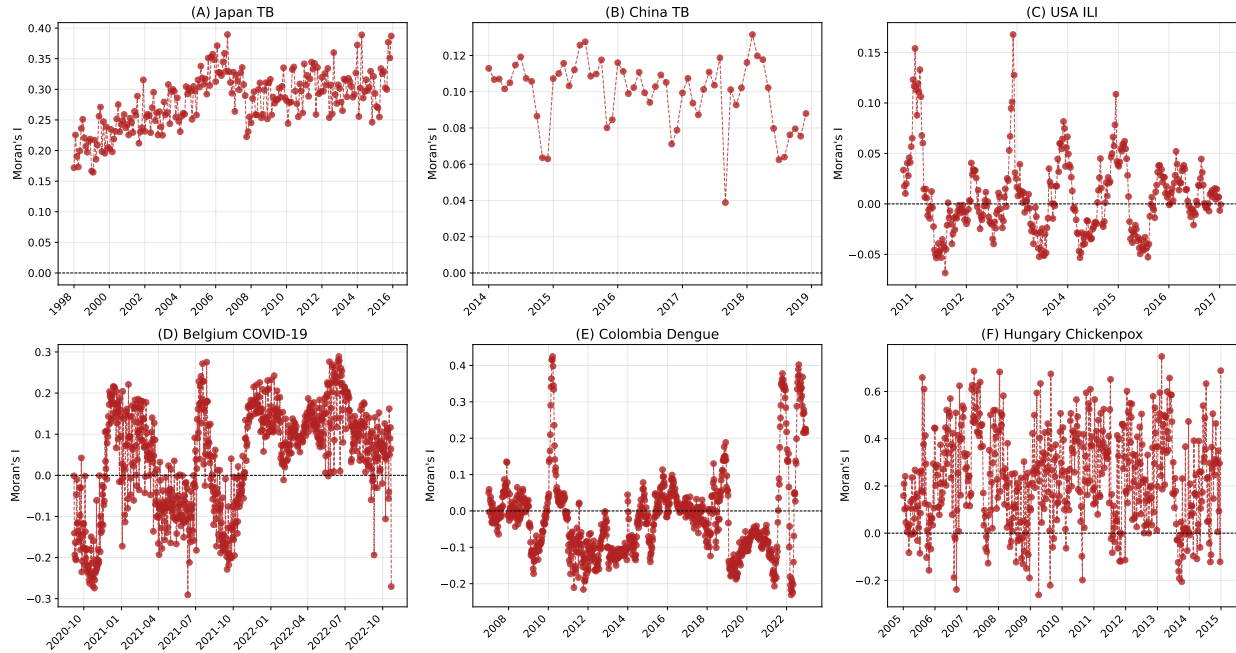


Fig. 4: Temporal evolution of global spatial autocorrelation (Moran's I) across the six epidemiological datasets.

dependencies to produce multi-step-ahead forecasts of the disease cases in a real-time setting. Moreover, effective epidemic forecasting necessitates robust probabilistic frameworks and uncertainty quantification to provide actionable insights for public health policy.

6.2 Experimental Setup

The experimental framework is designed for a rigorous, multi-horizon evaluation tailored to the temporal granularity of each dataset. The monthly datasets (Japan and China TB) are evaluated on 6, 12, and 24-month forecast horizons by producing out-of-sample multi-step-ahead forecasts, with the 24-month horizon excluded for China due to its limited length. The daily dataset (Belgium COVID-19) is assessed over 30, 60, and 90-day forecast horizons, while the weekly datasets (USA ILI, Colombia dengue, and Hungary chickenpox) are evaluated over 4, 9, and 13-week horizons. To prevent data leakage, a strict temporal split is employed (as shown in Fig. 5), where the final segment of each time series corresponding to the forecast horizon is held out as the test set. The training data is standardized before training the deep learning models. Specifically, each column is standardized using the individual mean and standard deviation of the corresponding column (node). The training process for the proposed models incorporated uniform noise for the Belgium dataset (due to pronounced localized sinusoidal patterns; see Fig. 7, panels (I)-(L)) and Gaussian noise for all other datasets, for comprehensive prediction interval coverage. Selecting the noise distribution was based on a validation approach. More implementation details such as the choice of validation set lengths and hyperparameter optimization are provided in Appendix E.1. The spatial topology used in GCEN is encoded in a static adjacency matrix A for each country as depicted in Fig. 17 in Appendix G. For all the datasets, the connectivity between nodes was determined using the Haversine distance, calculated as per (1) and the adjacency matrix was formed using the methodology described in Sec. 4.1.

Model performance is evaluated against a suite of competitive baselines, presented in Table 2. Brief specifications for these baseline architectures along with relevant references and implementation details are provided in Appendix E. We use a set of 10 metrics (see Appendix F for details) to assess both point and probabilistic forecast accuracy. Metrics used to evaluate point forecast performance are Symmetric Mean Absolute Percentage Error (SMAPE), Mean Absolute Error (MAE), Root Mean Squared Error (RMSE), Mean Absolute Scaled Error (MASE), and Root Mean Squared Scaled Error (RMSSE). Probabilistic metrics include Pinball loss at the 80th and 95th percentiles (Pinball-80, Pinball-95), ρ -risks at $\rho = 0.5$ and 0.9, Continuous Ranked Probability Score (CRPS), Winkler Score, and visualization of calibration through Probability Integral Transform (PIT) Q-Q plots. For the sake of completeness, we also report the

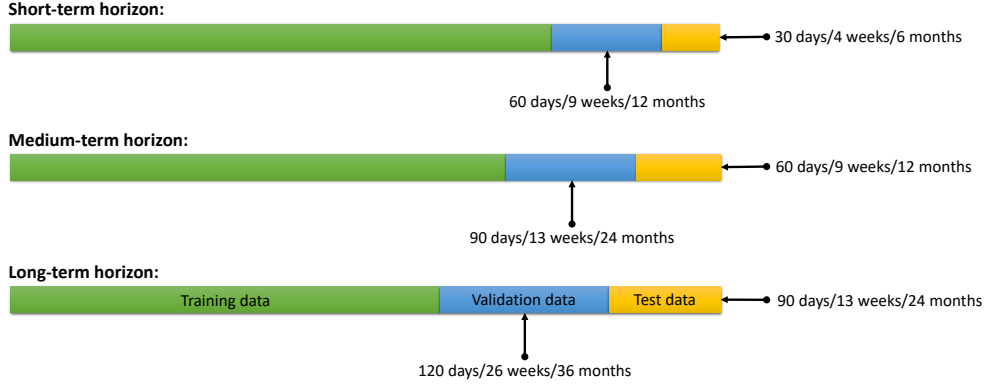


Fig. 5: Schematic of the training, validation, and test set splits across various forecast evaluation windows.

Table 2: Comparison of forecasting models. The columns assess whether each model can handle non-linearity, non-stationarity, low frequency data, is spatiotemporal and scalable, computationally lightweight, and finally can produce probabilistic forecasts.

Models	Non-linear	Non-stationarity	Scalability	Low-frequency	Spatiotemporal	Computationally lightweight	Probabilistic forecasting
LSTM (Hochreiter and Schmidhuber [1997])	✓	✓	✓	✓	✗	✓	✗
NHiTS (Challu et al. [2023])	✓	✓	✓	✓	✗	✓	✗
Transformers (Vaswani et al. [2017])	✓	✓	✓	✗	✗	✓	✗
TCN (Bai [2018])	✓	✓	✓	✓	✗	✓	✗
GSTAR (Ruchjana et al. [2012])	✗	✓	✗	✓	✓	✓	✗
STARMA (Pfeifer and Deutch [1980])	✗	✗	✗	✓	✓	✓	✗
STGCN (Yu et al. [2018])	✓	✓	✓	✗	✓	✗	✗
DeepAR (Salinas et al. [2020])	✓	✓	✓	✓	✗	✓	✓
Prob-iTransformer (Liu et al. [2023])	✓	✓	✓	✗	✗	✗	✓
GpGp (Guinness [2018])	✗	✗	✓	✓	✓	✗	✓
DiffSTG (Wen et al. [2023])	✓	✓	✓	✗	✓	✗	✓
STESN (Huang et al. [2022])	✓	✓	✓	✗	✓	✗	✓
MVEN (Proposed)	✓	✓	✓	✓	✓	✓	✓
GCEN (Proposed)	✓	✓	✓	✓	✓	✓	✓
STEN (Proposed)	✓	✓	✓	✓	✓	✓	✓

empirical coverage obtained by the 95% prediction intervals (PIs) produced by the probabilistic frameworks, although we argue that it is a misleading metric.

We observe that setting $\beta = 1$ in the energy score loss (3) gives the best results for our use-case. We use $M = 2$ during the training process, following prior works (Kraft et al. [2026], Shen and Meinshausen [2025]). This means that in the training loop, we call the model’s forward pass $M = 2$ times. Hence, two independent noise tensors are sampled and two distinct (in-sample) forecast trajectories $\hat{Y}^{(1)}$ and $\hat{Y}^{(2)}$ are generated, with which the loss is calculated. Essentially, the training time depends on the value of M ; a larger value of M will correspond to more training time. For evaluation, an ensemble of 100 forecast trajectories is generated, from which the median is extracted as the point prediction. Consistent with prior literature (Kraft et al. [2026]), we employ the median rather than the mean due to its superior robustness against outliers, thereby ensuring a more reliable point forecast trajectory.

Due to the inherent stochasticity of an engression model, a single trained instance yields non-deterministic forecasts. To ensure a robust and rigorous evaluation, we account for this variability by generating 50 independent prediction ensembles from the single trained model for each test case. The final results obtained by the performance metrics across three distinct forecast horizons, presented in Tables 10–12 (Appendix G), are reported as the mean and standard deviation computed across these 50 runs. To summarize, we repeat the process from forecast generation to metric calculation for 50 times and report the mean value for the metrics; for each forecast, we generate 100 trajectories and take the median as the point prediction. We also report the total computational time (both training and inference) measured in seconds in Table 9 in Appendix E.1. Time consumption by the proposed models in the total training-to-evaluation loop is significantly less, as compared to baselines such as STGCN, Prob-iTransformer, GpGp, DiffSTG, and STESN.

Moreover, the generation of multiple forecast trajectories to form a forecast ensemble leads to model-intrinsic uncertainty quantification. This property is leveraged to construct 95% PIs, with the lower and upper bounds defined by the 2.5th and 97.5th quantiles of the empirical forecast distribution (ensemble of 100 trajectories), respectively. The quality of

the intervals produced by MVEN, GCEN, and STEN are assessed on the test set using the Winkler score (Winkler et al. [1996]), PIT analysis, and empirical coverage, all of which are briefly described in Appendix F. The experimental results demonstrate the superiority of the proposed models in both point and probabilistic forecasting. Fig. 6 presents a comparative analysis with respect to CRPS, illustrating the performance of the proposed methods relative to the benchmark models across the six epidemic datasets. It is observed that, based on CRPS, the proposed models consistently outperform the state-of-the-art temporal and spatiotemporal methods.

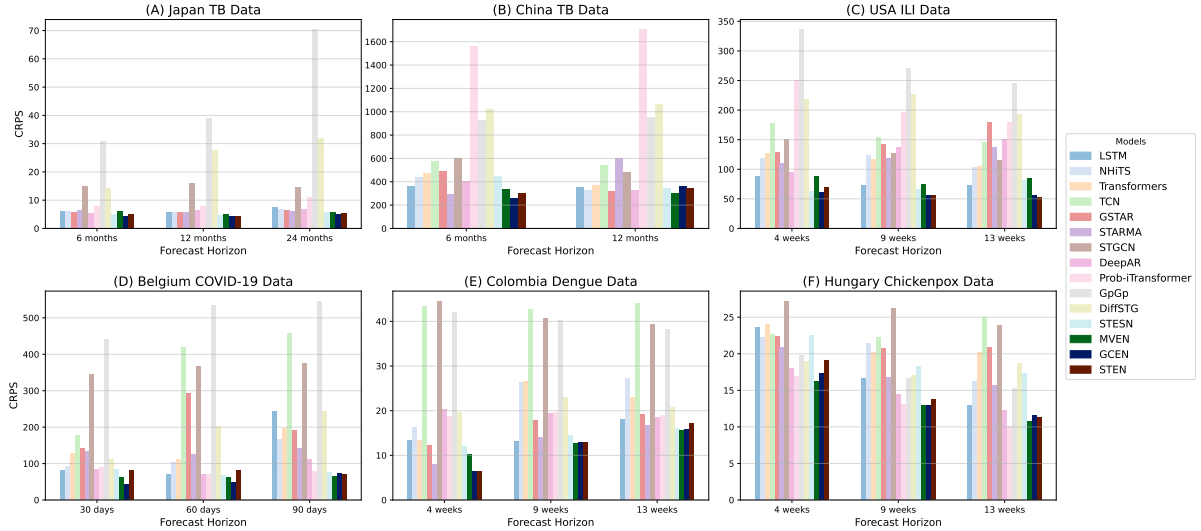


Fig. 6: CRPS of the proposed and benchmark models on the test sets of the (A) Japan TB, (B) China TB, (C) USA ILI, (D) Belgium COVID-19, (E) Colombia Dengue, and (F) Hungary Chickenpox datasets. Lower values indicate better performance. To maintain a comprehensible scale, results for TCN and Transformers on the Japan TB data are not shown due to their significantly larger CRPS magnitudes.

6.3 Point Forecast Performance

To compute the point forecasts in MVEN, GCEN, and STEN, we consider the median of the forecast ensemble. Experimental results on the point forecast metrics are reported in Tables 10-12, which depict that overall, the proposed methods either outperform the benchmarks, or remain competitive for short, medium, and long-term forecasting.

For Japan’s TB dataset, GCEN achieved the lowest SMAPE and MASE scores for the 6- and 12-month horizons, as well as the best MAE in all horizons. At the 24-month horizon, Transformers exhibited signs of instability with extremely high MAE and RMSE values (475.54 and 516.28, respectively). China’s TB dataset is characterized by low-frequency monthly observations and a restricted volume of 60 data points per province. In such data-constrained contexts, statistical models conventionally outperform deep learning architectures. For the 6-month forecast horizon, STARMA yielded the optimal values across several point metrics. Notably, GCEN remained highly competitive, frequently achieving the first and second ranks.

Our proposed models achieved high predictive accuracy on USA’s ILI and Belgium’s COVID-19 datasets. At the 4-week horizon for USA’s ILI data, STESN showed highly competitive performance, achieving the best scores in all point metrics. STEN performed the best at the 9-week horizon, excelling in all point metrics except SMAPE, where it is shy of LSTM by a very short margin. At the 13-week horizon, STEN attained the best scores in all metrics but RMSE. Across all the horizons, GCEN and STEN achieved better scores than MVEN in terms of metrics such as MAE and RMSE, reflecting the importance of the spatial modules. For 30- and 60-day forecasts on Belgium’s COVID-19 dataset, GCEN was unequivocally the best model, achieving the best scores in terms of all the point metrics. For the longest horizon of 90 days, GCEN and MVEN showed highly competitive performance, where MVEN frequently achieved the best and second best scores.

For Colombia’s dengue data, model performance varied across metrics and forecasting horizons. On the 4-week horizon, GCEN outperformed others in terms of SMAPE, and achieved the second best RMSE, MASE, and RMSSE. Overall, MVEN exhibited strong and consistent performance at the 9- and 13-week horizons, ranking first in five and two metrics respectively. In this particular context, the spatial modules (in GCEN and STEN) exhibit suboptimal performance, likely attributable to high levels of noise or the sparse spatial dependencies characteristic of the Colombia Dengue dataset (Fig. 4 (E)). On Hungary’s chickenpox data, MVEN achieved the best SMAPE, and GCEN scored the lowest MAE and MASE for the 4-week horizon. NHITS achieved the best RMSE, MASE (jointly with GCEN), and RMSSE scores. The 13-week horizon was characterized by mixed performance, with STEN achieving the best SMAPE, LSTM the best MAE and MASE, and NHITS the best RMSE and RMSSE.

6.4 Probabilistic Forecast Performance

Beyond point predictions, metrics like Pinball scores, ρ -risks, and CRPS evaluates probabilistic forecasts. The proposed models offer a natural way of uncertainty quantification through a probabilistic framework underpinned by a pre-additive noise-driven stochastic formulation. Fig. 7 presents the forecasts along with 95% PIs generated by MVEN, GCEN, and STEN on selected nodes across the datasets. The quality of the generated PIs is crucial for decision-making under uncertainty, and are evaluated using Winkler score and PIT Q-Q plots. Winkler score is a reliable metric for evaluating prediction intervals, which simultaneously penalizes both excessively wide intervals and low coverage. Overall, the point forecasts are well-aligned with the ground truth and the intervals provide sufficient coverage, as shown in Fig. 7.

Across all evaluated datasets and temporal horizons, the proposed engression-based models demonstrated superior performance, achieving the best Pinball scores, ρ -risks, and CRPS values in 70.59%, 67.65%, and 94.11% of the instances, respectively. GpGp, DiffSTG, and STESN showed diminished performance on Winkler scores. Furthermore, although GpGp attained high empirical coverage (97–100%; see Table 13 in Appendix G), its intervals were characterized by excessive width, resulting in suboptimal Winkler scores. The iTransformer architecture also frequently produced excessively wide intervals (which is not useful in decision making), especially for Colombia’s dengue dataset. A visualization of the forecasts and uncertainty intervals for DeepAR, Prob-iTransformer, and GpGp, for the same nodes as in Fig. 7, is provided in Fig. 18 in Appendix G. It is clear from the plots on the out-of-sample examples that our proposed models produced reasonable probabilistic bands (Fig. 7) as compared to the wide and uninformative bands produced by the benchmark spatiotemporal probabilistic models (Fig. 18).

To qualitatively evaluate the probabilistic calibration of our forecasting models, we employ PIT Q-Q plots and visualize the empirical PIT values against a theoretical Uniform(0, 1) distribution (see Appendix F for details on PIT). If the forecast ensembles are perfectly calibrated, these PIT values will follow a standard Uniform(0, 1) distribution. The Q-Q plots visualize this by mapping the empirical quantiles of these calculated PIT values (y-axis) against the theoretical quantiles of the Uniform distribution (x-axis). The plots are presented in Fig. 8. Points falling on the $y = x$ diagonal (dashed red line) indicate perfect calibration. Deviations into an S-shaped curve suggest overconfidence where PIs are narrow, while an inverse S-shape reveals underconfidence due to excessively wide intervals. The proposed models exhibit a characteristic S-shaped calibration curve, reflecting a high-precision forecasting approach that yields narrow, informative prediction intervals. While this indicates a degree of overconfidence, the curves remain closely aligned with the ideal diagonal across all datasets without requiring calibration using a validation set.

6.5 Statistical Test for Model Comparison

To evaluate the comparative performance of the forecasting models across all datasets and horizons, we employ the non-parametric Multiple Comparisons with the Best (MCB) test (Koning et al. [2005]). The MCB test is a statistical procedure used to identify which models are significantly better than others by computing their mean ranks and establishing a critical distance (Nemenyi [1963]). Any model whose critical distance does not overlap with the best-performing model is considered statistically inferior at the specified confidence level. This analysis is conducted across three distinct evaluation metrics: CRPS, SMAPE, and ρ -0.9 Risk, considering all datasets and forecast horizons. As illustrated in Fig. 9, our proposed models demonstrate superior robustness by consistently remaining within the top three positions across all of these metrics. Specifically, in terms of CRPS, GCEN achieved the lowest average rank of 2.18, establishing it as the overall best performer for probabilistic forecasting. MVEN and STEN secured the second and third spots respectively for the CRPS metric. For SMAPE, GCEN secured the top position with an average rank of 2.35. Finally, in the ρ -0.9 Risk evaluation, which emphasizes tail performance and high-quantile accuracy, the GCEN and STEN models maintain their competitive edge by achieving the second and third best ranks, following MVEN. The MCB analysis indicates that LSTM and NHITS remain competitive among temporal forecasting methods. In contrast, the remaining baseline models such as Transformers, STGCN, DiffSTG, and GpGp, exhibit mean ranks that exceed the critical threshold, signifying statistically inferior performance relative to the proposed models across the three

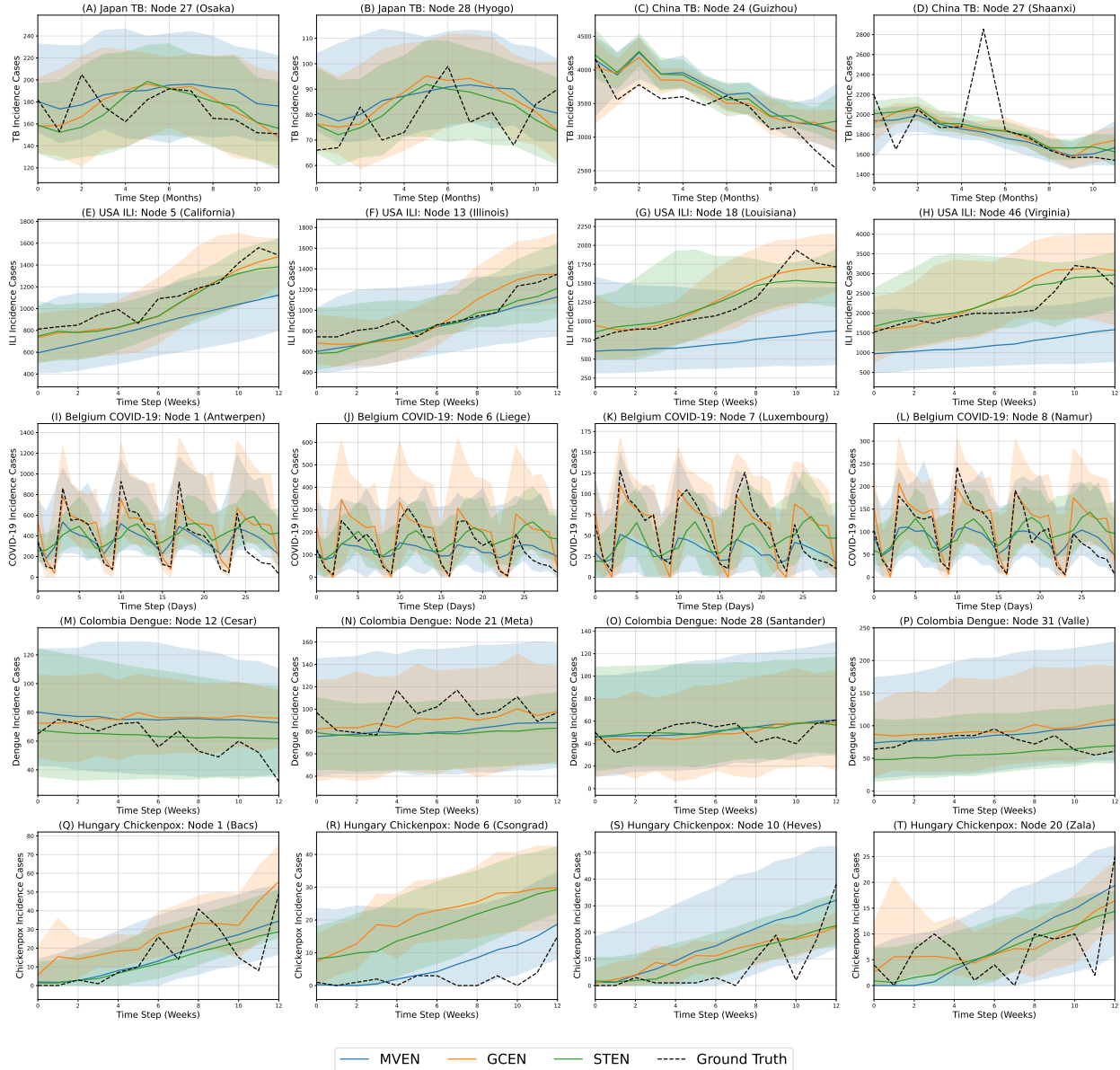


Fig. 7: Comparison of out-of-sample forecasts produced by MVEN (blue), GCEN (orange), and STEN (green) against the ground truth (test data) on selected nodes across the six datasets. The shaded regions denote the 95% PIs produced by the respective models.

evaluation metrics. This is due to the fact that most of these models work well with high-frequency (and high volume) data, as opposed to the nature of epidemic datasets.

7 Model Explainability

Temporal dependencies in our spatiotemporal engression models are handled using LSTM networks, which are generally less interpretable and considered as ‘black-box’ architectures (Guo et al. [2019]). Since the proposed architectures (MVEN, GCEN, and STEN) comprise pre-additive noise structure, we can look into the dynamics of the random noise values that are driving the non-linear layers of the model to produce an ensemble of forecast trajectories. Moreover, the

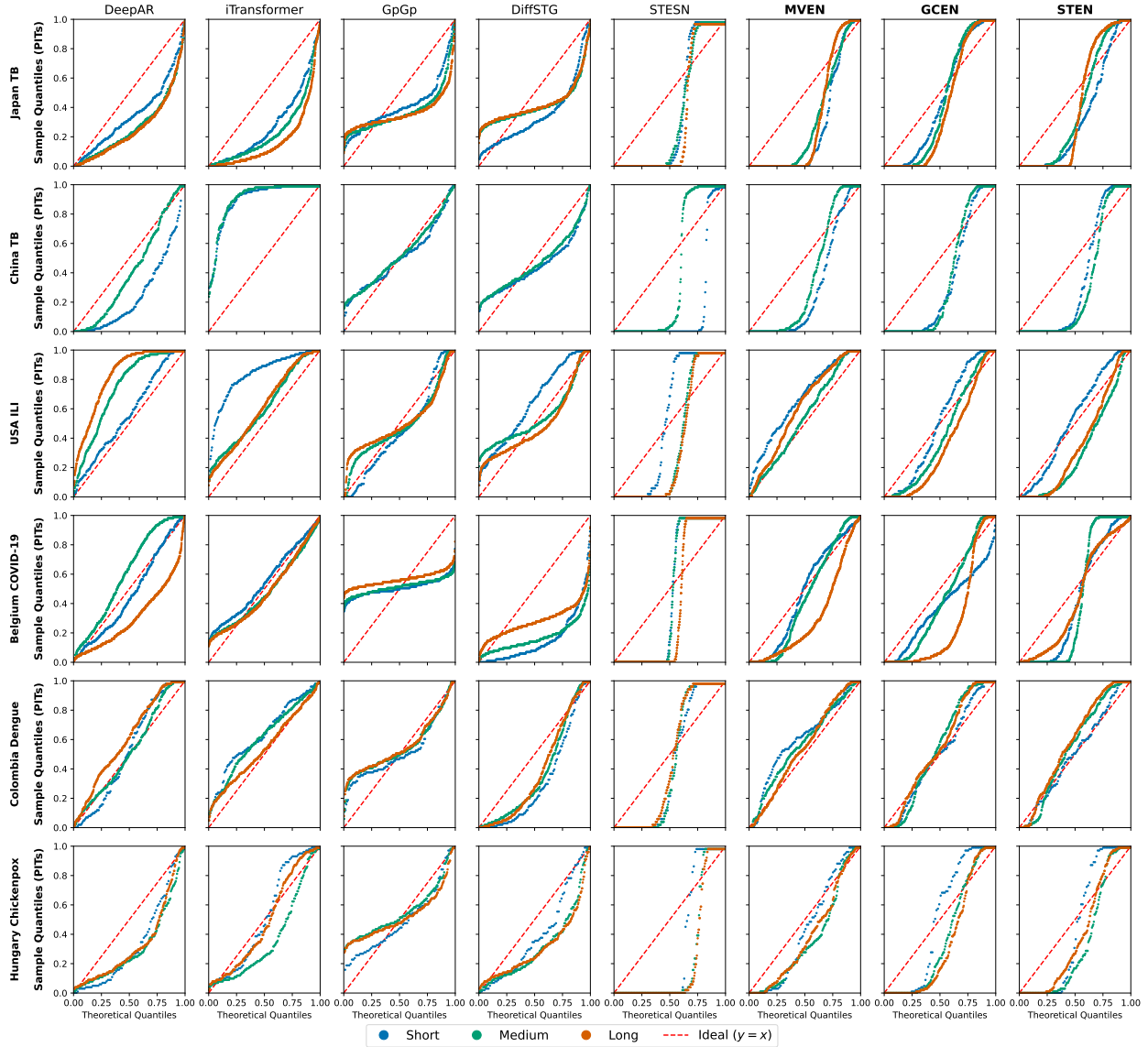


Fig. 8: Multi-horizon PIT Q-Q plots for qualitative evaluation of the probabilistic calibration of the proposed models across six epidemic datasets. Each subplot maps the empirical quantiles of the calculated PIT values (y-axis) against the theoretical quantiles of a standard Uniform(0,1) distribution (x-axis). The dashed red diagonal line ($y = x$) represents ideal calibration. The solid lines are color-coded by forecast horizons: short (blue), medium (green), and long (orange), to illustrate the stability of calibration over time. The China TB dataset excludes the long (24-month) horizon due to limited data length.

learned weights of the STAR-layer in STEN can also produce insights on the learned importance of each spatial lag, as discussed below.

7.1 Noise-Driven Generation of Forecast Trajectories

We take a peek into the internal dynamics of how injecting random noise values to the spatial embeddings (inputs to the temporal module) results in different plausible forecast trajectories for the same horizon. For the visualization, we sample $M = 30$ forecast trajectories from the trained GCEN, STEN, and MVEN models across three specific spatial nodes for demonstration purposes: Illinois (Node 13) for USA ILI, Santander (Node 28) for Colombia Dengue, and Osaka (Node 27) for Japan TB, respectively.

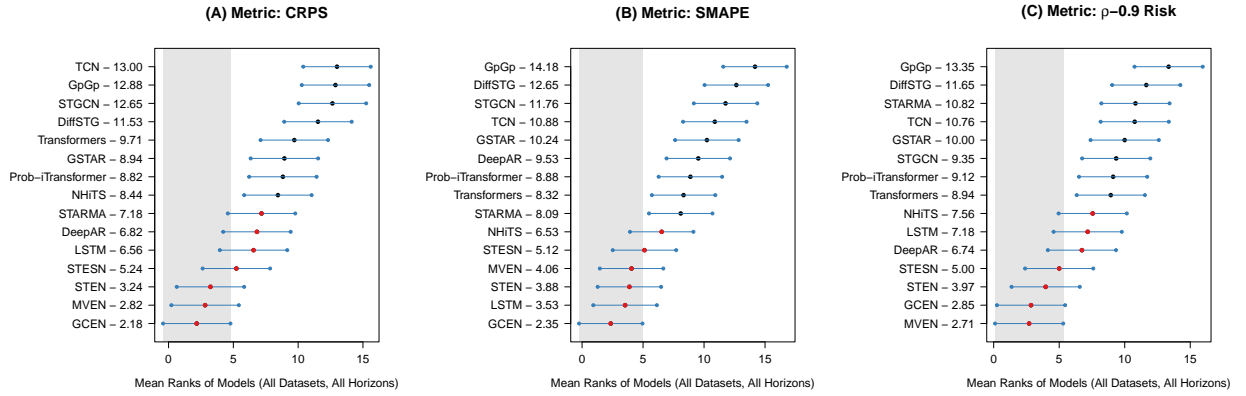


Fig. 9: MCB test results based on average ranks across six datasets and multiple forecast horizons for (A) CRPS, (B) SMAPE, and (C) $\rho-0.9$ Risk. ‘ $\mu-r$ ’ in the y-axis of each plot indicates that model μ ’s average rank is r according to that metric. The gray shaded region denotes the zone of statistical insignificance; any model whose interval overlaps with this region is not significantly different from the best-performing model at the $\alpha = 0.05$ level.

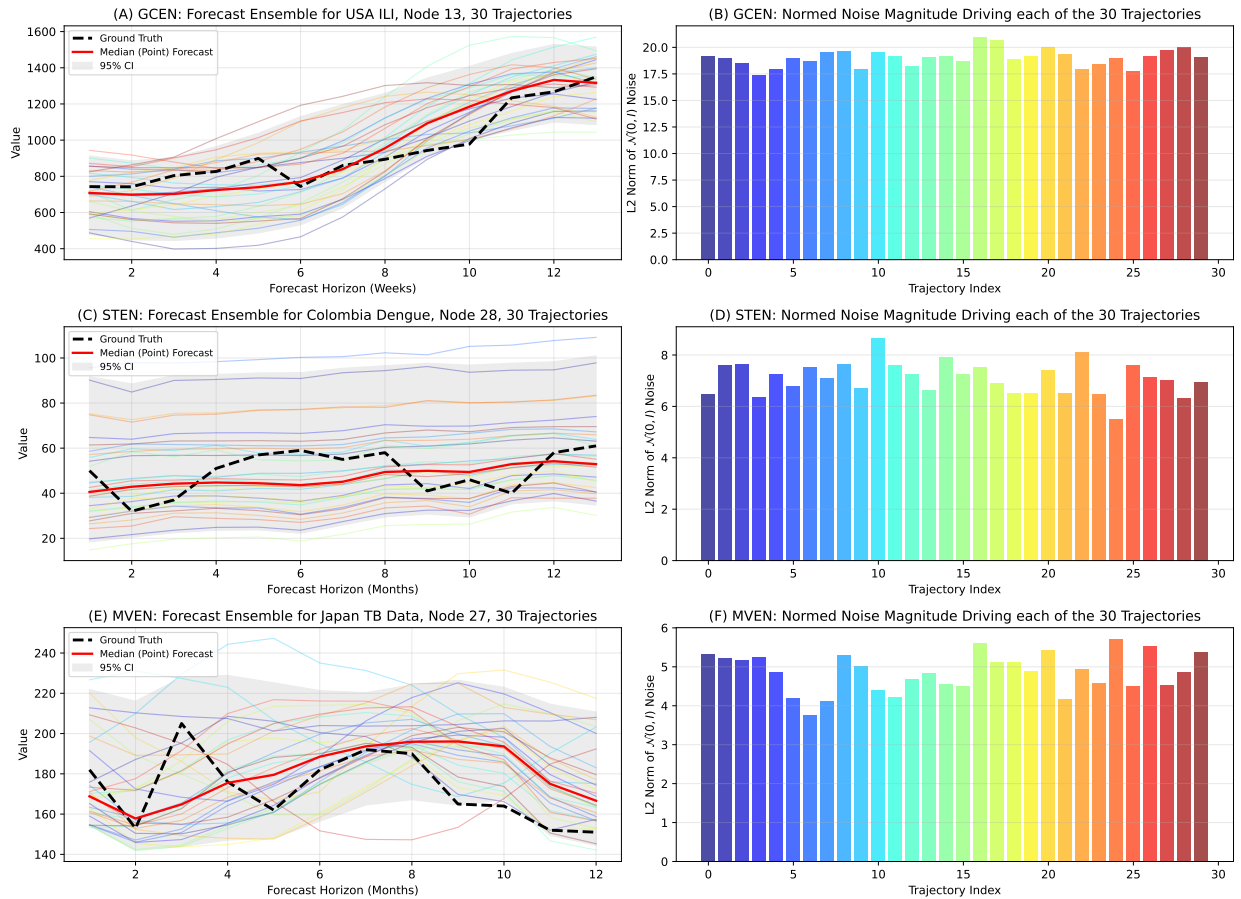


Fig. 10: Analysis of ensemble forecast dispersion and latent stochasticity in GCEN, STEN, and MVEN.

In each forward pass for GCEN and STEN, the stochastic driving force for each trajectory is derived from the exogenous random noise tensor $\boldsymbol{\eta} \sim \mathcal{N}(\mathbf{0}, \mathbf{I})^{p \times N \times D'}$ (for MVEN, $\boldsymbol{\eta} \sim \mathcal{N}(\mathbf{0}, \mathbf{I})^{p \times N \times D}$), where p is the temporal lag, N is the number of nodes, and D' (D) is the dimension of spatial embeddings (inputs). By isolating a specific node i , the noise contribution is reduced to a tensor $\boldsymbol{\eta}_i \in \mathbb{R}^{p \times D'}$. To quantify the magnitude of the perturbation driving each ensemble member, we compute the Frobenius norm (L_2 norm across the temporal and embedding dimensions):

$$\varepsilon_m = \|\boldsymbol{\eta}_i\|_F = \sqrt{\sum_{j=1}^p \sum_{k=1}^{D'} (\eta_{j,k})^2}.$$

This is done for all $M = 30$ trajectories, and we end up with a magnitude of noise value per trajectory, $\{\varepsilon_m\}_{m=1}^M$. Each noise ε_m is responsible for the generation of the m^{th} forecast trajectory. We visualize these dynamics in a dual-panel framework in Fig. 10: the left panel (A, C, E) presents the ensemble spaghetti plots, superimposing the median (solid red line), 95% confidence interval (gray shaded region), and ground truth (dashed black line) in original units; while the right panel (B, D, F) depicts the corresponding noise magnitudes ε_m that produces each of the 30 trajectories. A unified color scheme enables a direct visual mapping between the latent noise intensity and the resulting forecast dispersion. The noise tensors are integrated into the standardized feature space during the forward pass. While the right panel depicts the Frobenius norms of these raw noise tensors, the forecast trajectories in the left panel are unstandardized to their original units to maintain physical interpretability and facilitate direct comparison with the ground truth. From the plots, it is evident that noise tensors with higher magnitudes produce forecasts that generally lie above the median, and vice versa.

7.2 Importance of Spatial Lags in STEN

A key feature of STEN is the set of learnable weight matrices ($\Phi_l \in \mathbb{R}^{D \times D'}$) that combine multi-scale spatial lags $W^l \mathbf{Y}_t$ (the notations are as before). The explanation of spatial lag importance offers a transparent view into the specific spatiotemporal dynamics learned by the STEN model for each epidemic. To quantify this, the importance score for each spatial lag l is calculated as the Frobenius norm (Nie et al. [2010]) of its corresponding learned weight matrix, Φ_l :

$$\|\Phi_l\|_F = \sqrt{\sum_{i=1}^D \sum_{j=1}^{D'} (\phi_{i,j}^{(l)})^2}.$$

These scores are then normalized by dividing each lag's individual score by the sum of all scores and converting it to a percentage, which represents its relative contribution to the final embedding:

$$P_l = \left(\frac{\|\Phi_l\|_F}{\sum_{k=0}^L \|\Phi_k\|_F} \right) \times 100\%,$$

where L is the maximum number of spatial lags considered, and P_l represents the normalized percentage importance of lag l to the final spatiotemporal embedding. A high importance at the $l = 0$ (self) lag indicates a strong autoregressive component, suggesting that a region's future incidence is predominantly driven by its own historical momentum and internal dynamics. In contrast, high importance at $l = 1$ (neighbors) signifies a classic spatial diffusion effect, where the epidemic is primarily spread through contagion from immediately adjacent regions. Finally, significant importance at higher-order lags ($l > 1$) reveals more complex, non-local transmission routes, which can be attributed to multiple factors, such as transportation routes, hierarchical spread, and shared environmental or demographic factors.

Fig. 11 presents a comparative analysis of the learned spatial dependencies within the STEN model, visualized for each of the six epidemic datasets. The forecast horizons chosen are 30-day, 13-week, and 12-month for the daily, weekly, and monthly datasets, respectively. The $l = 0$ lag serves as the primary predictor for USA ILI (43.8%) and China TB (40.3%), indicating that these diseases are driven largely by local historical incidence. In contrast, Belgium COVID-19 exhibits a clear spatial diffusion profile, where the influence of first-order ($l = 1$, 35.2%) and second-order neighbors ($l = 2$, 35.3%) outweighs local history ($l = 0$, 29.6%). A more balanced importance distribution across all spatial lags is observed in Japan TB and Hungary chickenpox. For the Colombia dengue dataset, the prevalence of significant weights at $l = 0$ and $l = 2$ suggests that the forecast is driven by a combination of strong local autoregressive dependencies ($l = 0$) and second-order spatial influences ($l = 2$), the latter potentially reflecting shared regional climatic drivers across non-immediate neighbors. These results validate the STEN architecture's capability as an explainable framework, successfully learning and quantifying the diverse, disease-specific spatial contagion patterns inherent in the data.

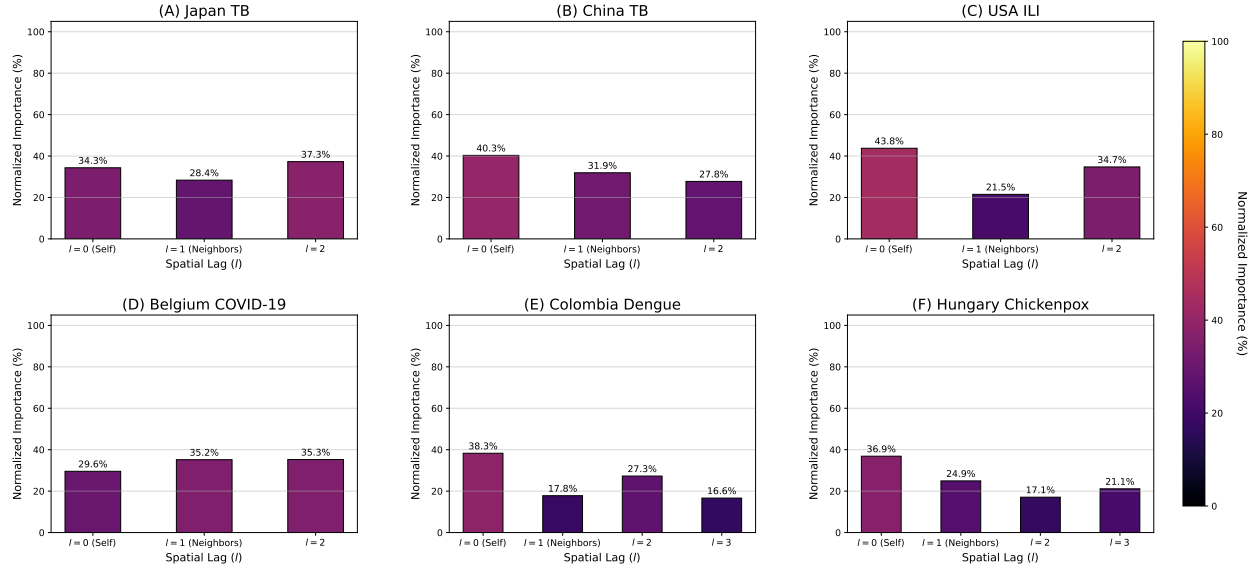


Fig. 11: Analysis of learned spatial lag importance from the STEN model across all six epidemic datasets. The maximum lag shown for each subplot (e.g., $l = 2$ for (A) and (D), $l = 3$ for (E)) corresponds to the `max_spatial_lag` hyperparameter selected for that specific dataset’s model.

8 Conclusion

This study addresses the challenge of probabilistic spatiotemporal forecasting by introducing three lightweight and generative deep learning frameworks: MVEN, GCEN, and STEN. By integrating the engression methodology with robust neural architectures, we established probabilistic frameworks capable of modeling both spatial and temporal dependencies while quantifying uncertainty. A theoretical contribution of this work is the formal derivation of geometric ergodicity and asymptotic stationarity for the proposed generative processes. These proofs provide essential mathematical guarantees regarding the stability of the models. Empirically, the models were rigorously benchmarked across six diverse epidemiological datasets, covering various diseases and geographical topologies with varying sizes and granularities. The results consistently demonstrated the superiority of the spatiotemporal engression approaches over state-of-the-art baselines, even when data is scarce. Furthermore, the probabilistic nature of these frameworks enabled the generation of well-calibrated model-intrinsic PIs, as evidenced by the PIT analysis and Winkler scores. Our models consistently achieved better CRPS, Pinball scores, and Winkler scores against the baseline probabilistic models. More recently developed models such as NBeats (Oreshkin et al. [2019]) and NHiTS (Challu et al. [2023]) can also be used instead of LSTM as the temporal module for the proposed models. Moreover, the construction of the spatial weights matrix for STEN can be made flexible. Instead of using the inverse of Haversine distances, one may use other established techniques, such as the k -nearest neighbors, or neighbors of order k based on contiguity (Moraga [2023]).

A primary advantage of the proposed engression-based models lies in their computational parsimony during both the training and inference phases. The popularly used STGCN (Yu et al. [2018]) requires a large number of training samples, and is computationally heavy, registering the longest training times of all models evaluated in this study. The baseline spatiotemporal probabilistic frameworks such as GpGp, DiffSTG, and STESN, encounter prohibitive temporal overhead during ensemble generation from the trained models (see Table 9 in Appendix E.1). Consequently, the high latency inherent in traditional models precludes their effective deployment in near-real-time epidemiological surveillance and forecasting.

The STEN model, in particular, demonstrated distinct explainability advantages. By leveraging a STAR-inspired spatial layer, it allowed for the quantification of specific spatial lag importances, offering public health officials actionable insights into the relative dominance of local autoregressive trends versus spatial diffusion mechanisms. While the MCB test establishes the statistical superiority of GCEN in terms of predictive accuracy, STEN provides a more explainable framework for characterizing the underlying spatial dynamics of the process. These findings establish MVEN, GCEN, and STEN as robust, computationally viable tools for real-time disease surveillance, offering a reliable methodology for policy formulation under uncertainty. Beyond the current scope, these methodologies possess the inherent flexibility to model various phenomena, such as traffic flow dynamics and air quality forecasting in spatiotemporal domain.

Limitations and Future Directions

While the proposed frameworks offer distinct advantages in terms of intrinsic uncertainty quantification and computational efficiency, they are not without limitations. A primary constraint lies in the models' diminished capacity to accurately forecast extreme peaks, which is often a requirement in epidemiological modeling for anticipating and managing peak outbreak scenarios. This behavior is empirically evident in the results (for example, Shaanxi in China TB data; see Fig. 7 (D)). This can be considered as a future scope of research where extreme value modeling of epidemics can be integrated with spatiotemporal engression models to capture extremes.

Second, the current study exclusively relies on historical epidemic incidence data, which omits the influence of exogenous determinants that fundamentally drive disease dynamics. While factors such as climatic variability for dengue or demographic density for COVID-19 and TB are known to modulate transmission, this work does not consider them as exogenous features. However, the proposed architecture is designed to be inherently generalizable to a multifaceted input space $\mathcal{Y} \in \mathbb{R}^{T \times N \times D}$, where the last dimension may encompass both the primary endogenous variables intended for forecasting and auxiliary exogenous covariates that provide supportive contextual information. Fully connected layers can be utilized to project the high-dimensional hidden states back into a refined output space that corresponds strictly to the target variables of interest.

Furthermore, our proposals are data-centric models. However, in epidemic forecasting, deep learning models integrated with epidemic knowledge (Barman et al. [2025]) are often of interest. The current work can be extended to include epidemiological factors and integrated with compartmental models in future research. Such an integration would likely enhance predictive accuracy and provide more robust contextual information for public health decision-making under uncertainty.

Finally, in engression, the discrepancy between the target and the functional space is sensitive to the choice of the distance metric. For example, Shen and Meinshausen [2025], Kraft et al. [2026], and the present work utilizes the L_2 norm in the energy score loss. Copula-based density regression might be viewed as an alternative. A copula operates on a topological space, avoiding such a choice of specific distance metric.

Competing Interests

No competing interest is declared.

Data and Code Availability

The datasets and codes used in this study are available in our GitHub repository <https://github.com/PyCoder913/stengression>. The `stengression` Python package offers an end-to-end implementation of our approaches.

References

- Kathryn A Glatter and Paul Finkelman. History of the plague: An ancient pandemic for the age of COVID-19. *The American Journal of Medicine*, 134(2):176–181, 2021.
- Antoni Trilla, Guillem Trilla, and Carolyn Daer. The 1918 “spanish flu” in spain. *Clinical infectious diseases*, 47(5): 668–673, 2008.
- James D Cherry and Paul Krogstad. SARS: the First Pandemic of the 21st Century. *Pediatric research*, 56(1):1–5, 2004.
- Catherine F Houlihan, Catherine R McGowan, Steve Dicks, Marc Baguelin, David AJ Moore, David Mabey, Chrissy H Roberts, Alex Kumar, Dhan Samuel, Richard Tedder, et al. Ebola exposure, illness experience, and ebola antibody prevalence in international responders to the west african ebola epidemic 2014–2016: A cross-sectional study. *PLoS medicine*, 14(5):e1002300, 2017.
- Neil M Ferguson, Zulma M Cucunubá, Ilaria Dorigatti, Gemma L Nedjati-Gilani, Christl A Donnelly, Maria-Gloria Basáñez, Pierre Nouvellet, and Justin Lessler. Countering the Zika epidemic in Latin America. *Science*, 353(6297): 353–354, 2016.
- Tanujit Chakraborty and Indrajit Ghosh. Real-time forecasts and risk assessment of novel coronavirus (COVID-19) cases: A data-driven analysis. *Chaos, Solitons & Fractals*, 135:109850, 2020.
- Konstantinos Benidis, Syama Sundar Rangapuram, Valentin Flunkert, Yuyang Wang, Danielle Maddix, Caner Turkmen, Jan Gasthaus, Michael Bohlke-Schneider, David Salinas, Lorenzo Stella, et al. Deep learning for time series forecasting: Tutorial and literature survey. *ACM Computing Surveys*, 55(6):1–36, 2022.

- Madhurima Panja, Tanujit Chakraborty, Uttam Kumar, and Nan Liu. Epicasting: an ensemble wavelet neural network for forecasting epidemics. *Neural Networks*, 165:185–212, 2023.
- John PA Ioannidis, Sally Cripps, and Martin A Tanner. Forecasting for COVID-19 has failed. *International Journal of Forecasting*, 38(2):423–438, 2022.
- Aaron Rumack, Ryan J Tibshirani, and Roni Rosenfeld. Recalibrating probabilistic forecasts of epidemics. *PLOS Computational Biology*, 18(12):e1010771, 2022.
- William Ogilvy Kermack and Anderson G McKendrick. A contribution to the Mathematical Theory of Epidemics. *Proceedings of the Royal Society of London. Series A, Containing papers of a mathematical and physical character*, 115(772):700–721, 1927.
- Domenico Benvenuto, Marta Giovanetti, Lazzaro Vassallo, Silvia Angeletti, and Massimo Ciccozzi. Application of the ARIMA model on the COVID-2019 epidemic dataset. *Data in brief*, 29:105340, 2020.
- Raydonal Ospina, João AM Gondim, Víctor Leiva, and Cecilia Castro. An overview of forecast analysis with ARIMA models during the COVID-19 pandemic: Methodology and case study in Brazil. *Mathematics*, 11(14):3069, 2023.
- Sepp Hochreiter and Jürgen Schmidhuber. Long short-term memory. *Neural computation*, 9(8):1735–1780, 1997.
- Philemon Manliura Datilo, Zuhaimy Ismail, and Jayeola Dare. A review of epidemic forecasting using artificial neural networks. *Epidemiology and Health System Journal*, 6(3):132–143, 2019.
- Vinay Kumar Reddy Chimmula and Lei Zhang. Time series forecasting of COVID-19 transmission in Canada using LSTM networks. *Chaos, solitons & fractals*, 135:109864, 2020.
- Ahmet Kara. Multi-step influenza outbreak forecasting using deep LSTM network and genetic algorithm. *Expert Systems with Applications*, 180:115153, 2021.
- Glenn Shafer and Vladimir Vovk. A tutorial on conformal prediction. *Journal of Machine Learning Research*, 9(3), 2008.
- Madhab Barman, Madhurima Panja, Nachiketa Mishra, and Tanujit Chakraborty. Epidemic-guided deep learning for spatiotemporal forecasting of tuberculosis outbreak. *Machine Learning*, 114(10):213, 2025.
- Madhurima Panja, Tanujit Chakraborty, Anubhab Biswas, and Soudeep Deb. E-STGCN: extreme spatio-temporal graph convolutional networks for air quality forecasting. *Journal of the Royal Statistical Society Series A: Statistics in Society*, pages 1–51, 2026.
- David Salinas, Valentin Flunkert, Jan Gasthaus, and Tim Januschowski. DeepAR: Probabilistic forecasting with autoregressive recurrent networks. *International Journal of Forecasting*, 36(3):1181–1191, 2020.
- Julien Herzen, Francesco Lässig, Samuele Giuliano Piazzetta, Thomas Neuer, Léo Tafti, Guillaume Raille, Tomas Van Pottelbergh, Marek Pasięka, Andrzej Skrodzki, Nicolas Huguenin, et al. Darts: User-friendly modern machine learning for time series. *Journal of Machine Learning Research*, 23(124):1–6, 2022.
- Vilde Jensen, Filippo Maria Bianchi, and Stian Normann Anfinsen. Ensemble conformalized quantile regression for probabilistic time series forecasting. *IEEE Transactions on Neural Networks and Learning Systems*, 35(7):9014–9025, 2022.
- Nadja Klein, Michael Stanley Smith, and David J Nott. Deep distributional time series models and the probabilistic forecasting of intraday electricity prices. *Journal of Applied Econometrics*, 38(4):493–511, 2023.
- Phillip E Pfeifer and Stuart Jay Deutch. A three-stage iterative procedure for space-time modeling phillip. *Technometrics*, 22(1):35–47, 1980.
- Zewen Liu, Guancheng Wan, B Aditya Prakash, Max SY Lau, and Wei Jin. A review of graph neural networks in epidemic modeling. In *Proceedings of the 30th ACM SIGKDD conference on knowledge discovery and data mining*, pages 6577–6587, 2024.
- Zhijian Li, Xiyang Luo, Bao Wang, Andrea L Bertozzi, and Jack Xin. A study on graph-structured recurrent neural networks and sparsification with application to epidemic forecasting. In *World congress on global optimization*, pages 730–739. Springer, 2019.
- Songgaojun Deng, Shusen Wang, Huzefa Rangwala, Lijing Wang, and Yue Ning. Cola-GNN: Cross-location Attention based Graph Neural Networks for long-term ILI prediction. In *Proceedings of the 29th ACM International Conference on Information & Knowledge Management*, pages 245–254, 2020.
- Feng Xie, Zhong Zhang, Liang Li, Bin Zhou, and Yusong Tan. EpiGNN: Exploring spatial transmission with graph neural network for regional epidemic forecasting. In *Joint European Conference on Machine Learning and Knowledge Discovery in Databases*, pages 469–485. Springer, 2022.

- Mingjie Qiu, Zhiyi Tan, and Bing-Kun Bao. MSGNN: Multi-scale Spatio-temporal Graph Neural Network for epidemic forecasting. *Data Mining and Knowledge Discovery*, 38(4):2348–2376, 2024.
- Yongqi Liu, Hui Qin, Zhendong Zhang, Shaoqian Pei, Zhiqiang Jiang, Zhongkai Feng, and Jianzhong Zhou. Probabilistic spatiotemporal wind speed forecasting based on a variational bayesian deep learning model. *Applied Energy*, 260: 114259, 2020.
- Haomin Wen, Youfang Lin, Yutong Xia, Huaiyu Wan, Qingsong Wen, Roger Zimmermann, and Yuxuan Liang. DiffSTG: Probabilistic spatio-temporal graph forecasting with denoising diffusion models. In *Proceedings of the 31st ACM International Conference on Advances in Geographic Information Systems*, pages 1–12, 2023.
- Huang Huang, Stefano Castruccio, and Marc G Genton. Forecasting high-frequency spatio-temporal wind power with dimensionally reduced echo state networks. *Journal of the Royal Statistical Society Series C: Applied Statistics*, 71(2):449–466, 2022.
- Xinwei Shen and Nicolai Meinshausen. Engression: extrapolation through the lens of distributional regression. *Journal of the Royal Statistical Society Series B: Statistical Methodology*, 87(3):653–677, 2025.
- Basil Kraft, Steven Stalder, William H Aeberhard, Nicolás Harrington Ruiz, Nicolai Meinshausen, Xinwei Shen, and Lukas Gudmundsson. Modeling uncertainty with engression: A deep generative time-series approach. *Geophysical Research Letters*, 53(2):e2025GL120122, 2026.
- J Clarke, A Lim, P Gupte, DM Pigott, WG Van Panhuis, and OJ Brady. A global dataset of publicly available dengue case count data. *Scientific Data*, 11(1):296, 2024.
- Kenneth R Rebman. The Pigeonhole Principle (What it is, how it works, and how it applies to map coloring). *The Two-Year College Mathematics Journal*, 10(1):3–13, 1979.
- Tilmann Gneiting and Adrian E Raftery. Strictly proper scoring rules, prediction, and estimation. *Journal of the American statistical Association*, 102(477):359–378, 2007.
- Bing Yu, Haoteng Yin, and Zhanxing Zhu. Spatio-temporal graph convolutional networks: a deep learning framework for traffic forecasting. In *Proceedings of the 27th International Joint Conference on Artificial Intelligence*, pages 3634–3640, 2018.
- TN Kipf. Semi-supervised classification with Graph Convolutional Networks. *arXiv preprint arXiv:1609.02907*, 2016.
- Justin Gilmer, Samuel S Schoenholz, Patrick F Riley, Oriol Vinyals, and George E Dahl. Neural message passing for quantum chemistry. In *International Conference on Machine Learning*, pages 1263–1272. Pmlr, 2017.
- Santosha Rathod, Bishal Gurung, KN Singh, and Mrinmoy Ray. An improved space-time autoregressive moving average (STARMA) model for modelling and forecasting of spatio-temporal time-series data. *Journal of the Indian Society of Agricultural Statistics*, 72(3):239–253, 2018.
- Richard S Sutton, Andrew G Barto, et al. *Reinforcement learning: An introduction*, volume 1. MIT press Cambridge, 1998.
- Sean P Meyn and Richard L Tweedie. *Markov chains and stochastic stability*. Springer Science & Business Media, 2012.
- Jingyu Zhao, Feiqing Huang, Jia Lv, Yanjie Duan, Zhen Qin, Guodong Li, and Guangjian Tian. Do RNN and LSTM have long memory? In *International Conference on Machine Learning*, pages 11365–11375. PMLR, 2020.
- RL Tweedie. Criteria for rates of convergence of markov chains, with application to queueing and storage theory. In *Probability, statistics and analysis*, volume 79, page 260. Cambridge University Press Cambridge, 1983.
- Ranjit Sah, Abdelmonem Siddiq, Bijaya K Padhi, Aroop Mohanty, Ali A Rabaan, Deepak Chandran, Chiranjib Chakraborty, and Kuldeep Dhama. Dengue virus and its recent outbreaks: current scenario and counteracting strategies. *International Journal of Surgery*, 109(9):2841–2845, 2023.
- Ayako Sumi and Nobumichi Kobayashi. Time-series analysis of geographically specific monthly number of newly registered cases of active tuberculosis in japan. *PLoS One*, 14(3):e0213856, 2019.
- Zhipeng Ma and Hong Fan. Influential factors of tuberculosis in mainland China based on MGWR model. *Plos one*, 18(8):e0290978, 2023.
- Benedek Rozemberczki, Paul Scherer, Oliver Kiss, Rik Sarkar, and Tamas Ferenci. Chickenpox cases in hungary: a benchmark dataset for spatiotemporal signal processing with graph neural networks. *arXiv preprint arXiv:2102.08100*, 2021a.
- Paula Moraga. *Spatial statistics for data science: theory and practice with R*. Chapman and Hall/CRC, 2023.

- Cristian Challu, Kin G Olivares, Boris N Oreshkin, Federico Garza Ramirez, Max Mergenthaler Canseco, and Artur Dubrawski. Nhits: Neural hierarchical interpolation for time series forecasting. In *Proceedings of the AAAI conference on artificial intelligence*, volume 37 (6), pages 6989–6997, 2023.
- Ashish Vaswani, Noam Shazeer, Niki Parmar, Jakob Uszkoreit, Llion Jones, Aidan N Gomez, Łukasz Kaiser, and Illia Polosukhin. Attention is all you need. *Advances in neural information processing systems*, 30, 2017.
- Shaojie Bai. An Empirical Evaluation of Generic Convolutional and Recurrent Networks for Sequence Modeling. *arXiv preprint arXiv:1803.01271*, 2018.
- Budi Nurani Ruchjana, Svetlana A Borovkova, HP Lopuhaa, Edy Tri Baskoro, and Djoko Suprijanto. Least squares estimation of Generalized Space Time AutoRegressive (GSTAR) model and its properties. In *AIP Conference Proceedings-American Institute of Physics*, volume 1450 (1), page 61, 2012.
- Yong Liu, Tengge Hu, Haoran Zhang, Haixu Wu, Shiyu Wang, Lintao Ma, and Mingsheng Long. iTransformer: Inverted transformers are effective for time series forecasting. *arXiv preprint arXiv:2310.06625*, 2023.
- Joseph Guinness. Permutation and grouping methods for sharpening gaussian process approximations. *Technometrics*, 60(4):415–429, 2018.
- Robert L Winkler, Javier Munoz, José L Cervera, José M Bernardo, Gail Blattenberger, Joseph B Kadane, Dennis V Lindley, Allan H Murphy, Robert M Oliver, and David Ríos-Insua. Scoring rules and the evaluation of probabilities. *Test*, 5(1):1–60, 1996.
- Alex J Koning, Philip Hans Franses, Michele Hibon, and Herman O Stekler. The M3 competition: Statistical tests of the results. *International Journal of Forecasting*, 21(3):397–409, 2005.
- Peter Bjorn Nemenyi. *Distribution-free multiple comparisons*. Princeton University, 1963.
- Tian Guo, Tao Lin, and Nino Antulov-Fantulin. Exploring interpretable LSTM neural networks over multi-variable data. In *International Conference on Machine Learning*, pages 2494–2504. PMLR, 2019.
- Feiping Nie, Heng Huang, Xiao Cai, and Chris Ding. Efficient and robust feature selection via joint ℓ_2 , 1-norms minimization. *Advances in neural information processing systems*, 23, 2010.
- Boris N Oreshkin, Dmitri Carпов, Nicolas Chapados, and Yoshua Bengio. N-BEATS: Neural basis expansion analysis for interpretable time series forecasting. *arXiv preprint arXiv:1905.10437*, 2019.
- Paul D Feigin and Richard L Tweedie. Random coefficient autoregressive processes: a Markov chain analysis of stationarity and finiteness of moments. *Journal of time series analysis*, 6(1):1–14, 1985.
- David A Dickey and Wayne A Fuller. Distribution of the Estimators for Autoregressive Time Series With a Unit Root. *Journal of the American Statistical Association*, 74(366a):427–431, 1979.
- Timo Teräsvirta, Chien-Fu Lin, and Clive WJ Granger. Power of the neural network linearity test. *Journal of time series analysis*, 14(2):209–220, 1993.
- Alexander Alexandrov, Konstantinos Benidis, Michael Bohlke-Schneider, Valentin Flunkert, Jan Gasthaus, Tim Januschowski, Danielle C Maddix, Syama Rangapuram, David Salinas, Jasper Schulz, et al. GluonTS: Probabilistic and neural time series modeling in python. *Journal of Machine Learning Research*, 21(116):1–6, 2020.
- Aldo V Vecchia. Estimation and model identification for continuous spatial processes. *Journal of the Royal Statistical Society Series B: Statistical Methodology*, 50(2):297–312, 1988.
- Benedek Rozemberczki, Paul Scherer, Yixuan He, George Panagopoulos, Alexander Riedel, Maria Astefanoaei, Oliver Kiss, Ferenc Beres, Guzman Lopez, Nicolas Collignon, et al. Pytorch geometric temporal: Spatiotemporal signal processing with neural machine learning models. In *Proceedings of the 30th ACM International Conference on Information & Knowledge Management*, pages 4564–4573, 2021b.
- Takuya Akiba, Shotaro Sano, Toshihiko Yanase, Takeru Ohta, and Masanori Koyama. Optuna: A next-generation hyperparameter optimization framework. In *Proceedings of the 25th ACM SIGKDD International Conference on Knowledge Discovery & Data Mining*, pages 2623–2631, 2019.
- Diederik P Kingma and Jimmy Ba. Adam: A method for stochastic optimization. *arXiv preprint arXiv:1412.6980*, 2014.
- Tilmann Gneiting, Daniel Wolfram, Johannes Resin, Kristof Kraus, Johannes Bracher, Timo Dimitriadis, Veit Hagenmeyer, Alexander I Jordan, Sebastian Lerch, Kaleb Phipps, et al. Model diagnostics and forecast evaluation for quantiles. *Annual Review of Statistics and Its Application*, 10(1):597–621, 2023.
- Matthias W Seeger, David Salinas, and Valentin Flunkert. Bayesian intermittent demand forecasting for large inventories. *Advances in neural information processing systems*, 29, 2016.

Appendix

A Mathematical Proofs for Section 5.1

A.1 Proof of Theorem 1

Proof. This proof follows a similar structure to that of Theorem 1 in Zhao et al. [2020], albeit they considered a post-additive noise process. Given that $S_t = (\mathbf{y}_t, \mathbf{h}_t) \in \mathbb{R}^k$, where $k = N + N'$. The process is defined as $S_t = \mathcal{F}(S_{t-1} + \varepsilon_t)$, where $\mathcal{F} : \mathbb{R}^k \rightarrow \mathbb{R}^k$ is a general non-linear function and $\varepsilon_t = (\boldsymbol{\eta}_t^\top; \boldsymbol{\xi}_t^\top)^\top$, where $\boldsymbol{\eta}_t \in \mathbb{R}^N$, $\boldsymbol{\xi}_t \in \mathbb{R}^{N'}$. $\{S_t\}$ is a homogeneous Markov chain on the state space $(\mathbb{R}^k, \mathcal{B}^k, \lambda_k)$. We shall establish geometric ergodicity by first showing that $\{S_t\}$ is λ_k -irreducible, followed by proving that it satisfies Tweedie's drift criterion (6) (Tweedie [1983]).

For a set $A \in \mathcal{B}^k$ and $\mathbf{s} \in \mathbb{R}^k$, the transition probability is given by

$$\mathbb{P}(\mathbf{s}, A) = \mathbb{P}(S_t \in A | S_{t-1} = \mathbf{s}) = \int_{\mathbb{R}^k} \mathbb{I}_A(\mathcal{F}(\mathbf{s} + z)) f_\varepsilon(z) dz,$$

where $f_\varepsilon(\cdot)$ denotes the density of ε_t , which is given by $f_\varepsilon(z) = \prod_{i=1}^N f_\eta(z_i) \prod_{j=N+1}^k f_\xi(z_j)$, because the noise coordinates are independent. By assumptions (A1) and (A2), the transition kernel admits a density that is positive on sets of positive Lebesgue measure. Thus, $\{S_t\}$ is λ_k -irreducible.

Finally, it remains to show that there exists a small set G with $\lambda_k(G) > 0$ and a non-negative continuous function $V(\mathbf{s})$ such that

$$\mathbb{E}[V(S_t) | S_{t-1} = \mathbf{s}] \leq \begin{cases} (1 - \delta)V(\mathbf{s}), & \mathbf{s} \notin G, \\ \widehat{M}, & \mathbf{s} \in G \end{cases} \quad (6)$$

for some $0 < \delta < 1$ and $0 < \widehat{M} < \infty$. By hypothesis, we have constants $0 < a < 1$ and b such that $\|\mathcal{F}(z)\| \leq a\|z\| + b$. Define test function $V(\mathbf{s}) = 1 + \|\mathbf{s}\| > 0$. Then,

$$\begin{aligned} \mathbb{E}[V(S_t) | S_{t-1} = \mathbf{s}] &= \mathbb{E}[V(\mathcal{F}(\mathbf{s} + \varepsilon_t))] \\ &= \mathbb{E}[1 + \|\mathcal{F}(\mathbf{s} + \varepsilon_t)\|] \\ &\leq 1 + \mathbb{E}[a\|\mathbf{s} + \varepsilon_t\| + b] \quad (\text{by hypothesis}) \\ &\leq 1 + \mathbb{E}[a\|\mathbf{s}\| + a\|\varepsilon_t\| + b] \quad (\text{triangle inequality}) \\ &= 1 + a\|\mathbf{s}\| + b + a\mathbb{E}(\|\varepsilon_t\|) \\ &= aV(\mathbf{s}) + 1 - a + b + a\mathbb{E}(\|\varepsilon_t\|) \end{aligned}$$

Define

$$\delta = 1 - a - \frac{1 - a + b + a\mathbb{E}(\|\varepsilon_t\|)}{V(\mathbf{s})}$$

and $G = \{\mathbf{s} : \|\mathbf{s}\| \leq L\}$ such that $V(\mathbf{s}) > 1 + \frac{b + \mathbb{E}(\|\varepsilon_t\|)}{1 - a} \forall \|\mathbf{s}\| > L$, which ensures that (6) holds true. Finally, as $\mathbb{E}[g(S_t) | S_{t-1} = \mathbf{s}]$ is continuous with respect to \mathbf{s} for any bounded and continuous function g , it follows that $\{S_t\}$ is a Feller chain (Feigin and Tweedie [1985]). As G is compact, by Feigin and Tweedie [1985], we have that G is a small set. Hence, by Theorem 4(ii) and 1 in Tweedie [1983] and Feigin and Tweedie [1985] respectively, it follows that $\{S_t\}$ is geometrically ergodic. \square

A.2 Proof of Theorem 2

Proof. This proof focuses on showing that the LSTM update equation satisfies the contraction property required by Theorem 1. Let $u = f_{\text{spatial}}(\mathbf{y}_{t-1}) + \boldsymbol{\eta}_t \in B_\infty^N$ by assumption (A4), $v = \mathbf{h}_{t-1} + \boldsymbol{\xi}_t \in B_\infty^{N'}$, $w = \mathbf{c}_{t-1} + \boldsymbol{\psi}_t$, and $x = o(u, v) \odot \tanh[i(u, v)] \odot \tanh(W_{ch}v + W_{cy}u + b_c) + f(u, v) \odot w \in B_\infty^{N'}$. Note that $x \in B_\infty^{N'} \implies \|x\|_1 \leq N'$. Our objective is to find $0 < a < 1$ and b such that $\|\mathcal{F}_{LSTM}(u, v, w)\|_1 \leq a\|(u, v, w)\|_1 + b$. Let $a = a_0 \in (0, 1)$ and $b = \widetilde{M} + 2N'$, where $\widetilde{M} := \sup_{x \in B_\infty^{N'}} \|g(W_{zh}x + b_z)\|_1 < \infty$, under assumption (A5). Thus, we have

$$\begin{aligned} &\|\mathcal{F}_{LSTM}(u, v, w)\|_1 - a_0\|(u, v, w)\|_1 \\ &\leq \|g(W_{zh}x + b_z)\|_1 + \|x\|_1 + \|\mathbf{1}_{N'} + f(u, v) \odot w\|_1 - a_0\|(u, v, w)\|_1 \\ &\leq \widetilde{M} + 2N' + \|f(u, v)\|_\infty \|w\|_1 - a_0(\|u\|_1 + \|v\|_1 + \|w\|_1) \\ &\leq \widetilde{M} + 2N' - a_0\|u\|_1 - a_0\|v\|_1 + (\|f(u, v)\|_\infty - a_0)\|w\|_1 \end{aligned}$$

We have by Assumption (A6), that

$$\begin{aligned} \|f(u, v)\|_\infty &= \|\sigma(W_{fh}v + W_{fy}u + b_f)\|_\infty \\ &\leq \sigma(\|W_{fh}\|_\infty + \|W_{fy}\|_\infty + \|b_f\|_\infty) \\ &\leq a_0. \end{aligned}$$

Putting together, we have

$$\|\mathcal{F}_{LSTM}(u, v, w)\|_1 - a_0 \|(u, v, w)\|_1 \leq \widetilde{M} + 2N' = b.$$

By Theorem 1, the GCEN and STEN processes as defined in (5) is geometrically ergodic. \square

B Algorithms

Algorithms 1, 2, and 3 present the pseudo codes for the forward passes of GCEN, STEN, and MVEN respectively. Algorithm for the training procedure is provided in Algorithm 4.

Algorithm 1 Graph Convolutional Engression Network (GCEN) Forward Pass

Require: Input tensor $\mathbf{Y} = \mathbf{Y}_{t-p+1:t} \in \mathbb{R}^{B \times p \times N \times D}$ (Batch, Lag, Nodes, Features); Adjacency info $\mathcal{G} = (\mathcal{V}, \mathcal{E})$; Noise distribution $\eta \sim \mathcal{P}_z$.

Ensure: Single forecast trajectory $\widehat{\mathbf{Y}} = \widehat{\mathbf{Y}}_{t+1:t+q} \in \mathbb{R}^{B \times q \times N \times D}$.

```

// Phase 1: Spatial feature extraction (GCN)
1: Permute  $\mathbf{Y}$  to node-first format:  $\mathbf{Y} \leftarrow \text{Permute}(\mathbf{Y}, (N, B, p, D))$ 
2: Compute transformed node features:  $\mathbf{H}_{nodes} = \mathbf{Y}\Theta_{GCN}$ 
3: Gather neighbor features  $\widetilde{\mathbf{Y}}$  based on edges  $\mathcal{E} \in \mathcal{G}$ 
4: Aggregate neighbor messages:  $\mathbf{M} = \text{Aggregate}(\mathbf{Y}, \widetilde{\mathbf{Y}})$  ▷ Mean, Sum, or Max
5: Combine and apply non-linearity:  $\mathbf{Z} = \sigma(\text{Combine}(\mathbf{H}_{nodes}, \mathbf{M}\Theta_{GCN}))$  ▷ Add or Concat
6: Permute back to batch-first format:  $\mathbf{Z} \leftarrow \text{Permute}(\mathbf{Z}, (B, p, N, D'))$ 
// Phase 2: Stochastic noise injection (Engression)
7: if NoiseMode is Additive then
8:   Sample  $\eta \sim \mathcal{P}_z$  with shape of  $\mathbf{Z}$ 
9:    $\mathbf{Z}_{noisy} = \mathbf{Z} + \eta$ 
10: else
11:   if NoiseMode is Concatenation then
12:     Sample  $\eta \sim \mathcal{P}_z$  with shape  $(B, p, N, D_{noise})$ 
13:      $\mathbf{Z}_{noisy} = [\mathbf{Z} \parallel \eta]$  ▷ Concatenate along feature dimension
14:   end if
15: end if
// Phase 3: Temporal processing (LSTM)
16: Reshape  $\mathbf{Z}_{noisy}$  for sequential processing:  $\mathbf{Z}_{noisy} \in \mathbb{R}^{p \times (B \cdot N) \times D_{net}}$ 
17: ▷  $D_{net} = D'$  if NoiseMode is Additive, else  $D_{net} = D' + D_{noise}$ 
18:  $(\mathbf{h}_n, \mathbf{c}_n) = \text{LSTM}(\mathbf{Z}_{noisy})$ 
19: Extract final hidden state:  $\mathbf{h}_{final} = \mathbf{h}_n[-1]$  ▷ Shape:  $(B \cdot N) \times D_{hidden}$ 
// Phase 4: Forecast generation
20: Project to forecast horizon:  $\widehat{\mathbf{Y}} = \text{Dense}(\mathbf{h}_{final})$  ▷ Shape:  $(B \cdot N) \times (q \cdot D)$ 
21: Reshape and permute:  $\widehat{\mathbf{Y}} \leftarrow \text{Reshape}(\widehat{\mathbf{Y}}, (B, q, N, D))$ 
22: return  $\widehat{\mathbf{Y}}$ 

```

C Energy Score Loss

Fig. 12 illustrates the components of the energy score loss in contrast to MSE. In the figure, the ground truth data points (blue) are generated using $y_t = 3 \sin(t) + \epsilon_t$, where $t = \{1, \dots, 5\}$ and $\epsilon_t \sim \mathcal{N}(0, 0.5)$. The corresponding predictions (orange) are generated using $\widehat{y}_t = y_t + \eta_t$, where $\eta_t \sim \mathcal{N}(0, 1.5)$. In panel (B), for each prediction \widehat{y}_t , the ensemble points constituting the orange shaded region is created by sampling 15 random points from $\mathcal{N}(\widehat{y}_t, 0.6)$.

The accuracy (first) term in the ES loss, analogous to MSE, minimizes the distance between the ground truth and predictions, effectively centering the sample cloud around the observed outcome. Conversely, the sharpness (second)

Algorithm 2 Spatio-Temporal Engression Network (STEN) Forward Pass

Require: Input tensor $\mathbf{Y} = \mathbf{Y}_{t-p+1:t} \in \mathbb{R}^{B \times p \times N \times D}$ (Batch, Lag, Nodes, Features); Spatial weights matrices $\{W^l\}_{l=0}^L$ for spatial lags 0 to L ; Noise distribution $\boldsymbol{\eta} \sim \mathcal{P}_z$.

Ensure: Single forecast trajectory $\hat{\mathbf{Y}} = \hat{\mathbf{Y}}_{t+1:t+q} \in \mathbb{R}^{B \times q \times N \times D}$.

// Phase 1: Spatial embedding (STAR-layer)

- 1: $\mathbf{Z}_{total} \leftarrow \mathbf{0} \in \mathbb{R}^{B \times p \times N \times D'}$
- 2: **for** $l = 0$ **to** L **do** ▷ Iterate through spatial lags
- 3: Compute spatial aggregation: $\mathbf{Y}_\tau^{(l)} = W^l \mathbf{Y}_\tau$ ▷ Performed for each $\tau \in \{t-p+1, \dots, t\}$; $\mathbf{Y}_\tau \in \mathbb{R}^{N \times D}$
- 4: Apply learnable transformation: $\mathbf{H}^{(l)} = \mathbf{Y}_\tau^{(l)} \Phi_l$ ▷ $\Phi_l \in \mathbb{R}^{D \times D'}$ is weight matrix for lag l
- 5: $\mathbf{Z}_{total} = \mathbf{Z}_{total} + \mathbf{H}^{(l)}$ ▷ Summation across all spatial lags
- 6: **end for**
- 7: $\mathbf{Z} = \text{ReLU}(\mathbf{Z}_{total})$ ▷ Final spatial embedding
- 8: Phase 2 to Phase 4 with the spatial embedding $\tilde{\mathbf{Z}}$ follows from Steps 7-22 in Algorithm 1.

Algorithm 3 Multivariate Engression Network (MVEN) Forward Pass

Require: Input tensor $\mathbf{Y} = \mathbf{Y}_{t-p+1:t} \in \mathbb{R}^{B \times p \times N \times D}$ (Batch, Lag, Nodes, Features); Noise distribution $\boldsymbol{\eta} \sim \mathcal{P}_z$.

Ensure: Single forecast trajectory $\hat{\mathbf{Y}} = \hat{\mathbf{Y}}_{t+1:t+q} \in \mathbb{R}^{B \times q \times N \times D}$.

// Phase 1: Stochastic noise injection (Engression)

- 1: **if** NoiseMode is *Additive* **then**
- 2: Sample $\boldsymbol{\eta} \sim \mathcal{P}_z$ with shape (B, p, N, D)
- 3: $\mathbf{Y}_{noisy} = \mathbf{Y} + \boldsymbol{\eta}$
- 4: **else**
- 5: **if** NoiseMode is *Concatenation* **then**
- 6: Sample $\boldsymbol{\eta} \sim \mathcal{P}_z$ with shape (B, p, N, D_{noise})
- 7: $\mathbf{Y}_{noisy} = [\mathbf{Y} \parallel \boldsymbol{\eta}]$ ▷ Concatenate along feature dimension D
- 8: **end if**
- 9: **end if**
- 10: The rest of the algorithm follows from steps 16-22 in Algorithm 1 with \mathbf{Y}_{noisy} instead of \mathbf{Z}_{noisy} .

Algorithm 4 Training Procedure of the Proposed Models

Require: Training dataset: $\mathcal{D} = \{(\mathbf{Y}_{t-p+1:t}, \mathbf{Y}_{t+1:t+q})\}$, $p \leq t \leq T - q$; Ensemble size: M ; Number of epochs: E ; Learning rate: ε ; Loss function: \mathcal{L} (energy score loss).

Ensure: Trained model parameters $\Theta = \{\Theta_{\text{Spatial}}, \Theta_{\text{LSTM}}, W_{\text{out}}\}$, where Θ_{Spatial} , Θ_{LSTM} , and W_{out} are the weight matrices for the spatial component (GCN/STAR; ignore for MVEN), LSTM, and dense layers respectively.

- 1: Initialize Θ using Xavier initialization;
- 2: Form batches of inputs and targets. Denote by $\mathcal{X} = [\mathbf{Y}_{t-p+1:t}] \in \mathbb{R}^{B \times p \times N \times D}$ the input sequences for different time points t stacked over the first (batch) dimension, and let $\mathcal{Y} = [\mathbf{Y}_{t+1:t+q}] \in \mathbb{R}^{B \times q \times N \times D}$ be the corresponding batch of target sequences;
- 3: **for** epoch = 1 **to** E **do**
- 4: **for** each batch $(\mathcal{X}, \mathcal{Y}) \in \mathcal{D}$ **do**
- 5: $\mathbf{S} \leftarrow \emptyset$ ▷ Initialize empty ensemble list
- 6: **// Ensemble generation during in-sample prediction. Typically, set $M = 2$**
- 7: **for** $m = 1$ **to** M **do**
- 8: $\hat{\mathcal{Y}}^{(m)} \leftarrow \text{Model}(\mathcal{X}; \Theta)$ ▷ Forward pass through GCEN/STEN/MVEN
- 9: $\mathbf{S} \leftarrow \mathbf{S} \cup \{\hat{\mathcal{Y}}^{(m)}\}$ ▷ Append to ensemble list; each forward pass produces a different forecast trajectory
- 10: **end for**
- 11: Form the forecast ensemble tensor by stacking the elements of \mathbf{S} along the first dimension: $\hat{\mathcal{Y}}_{ensemble} \in \mathbb{R}^{M \times B \times q \times N \times D}$
- 12: **// Loss computation and backpropagation**
- 13: loss $\leftarrow \mathcal{L}(\mathcal{Y}, \hat{\mathcal{Y}}_{ensemble})$ ▷ Probabilistic loss over ensemble
- 14: $\Theta \leftarrow \Theta - \varepsilon \cdot \nabla_{\Theta}(\text{loss})$ ▷ Update weights via Adam/SGD
- 15: **end for**
- 16: Record loss per epoch for convergence monitoring;
- 17: **end for**
- 18: **return** Θ

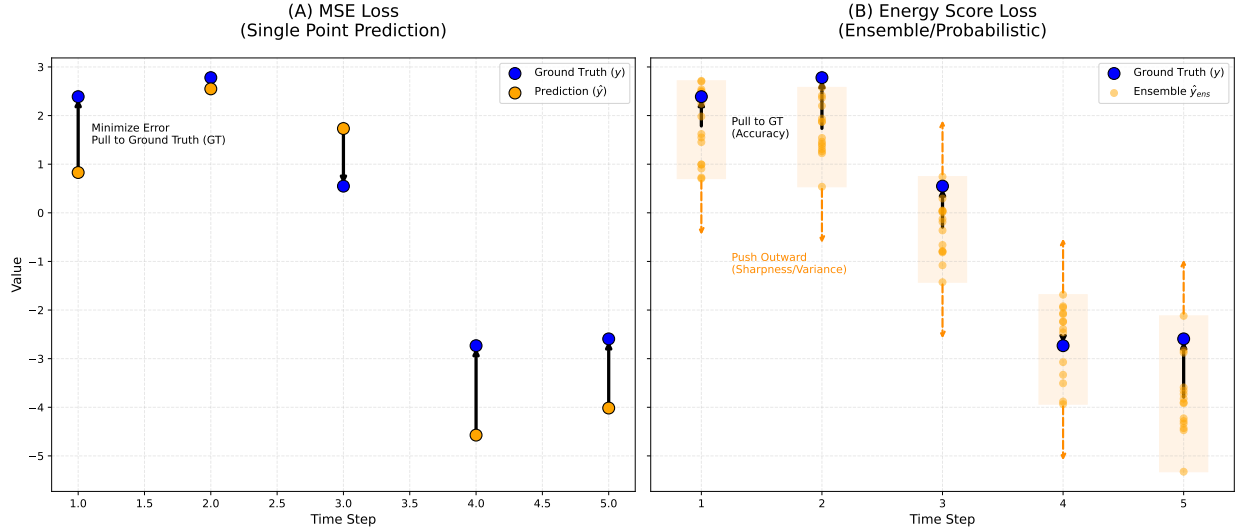


Fig. 12: A visual comparison between MSE and energy score loss using toy data. The accuracy term ($\mathcal{L}_{accuracy}$) in ES loss is analogous to MSE. The sharpness term is what makes energy score a probabilistic loss function.

term is the average distance between prediction pairs. This is subtracted within the loss function. Maximizing this distance during training encourages predictive diversity and prevents mode collapse, where the model might otherwise converge on identical values. This forces the model to generate a spread of plausible futures that accurately reflect underlying uncertainty. The energy score loss inherently balances exploitation - anchoring the predictive distribution to the ground truth via the accuracy term, with exploration - effectively penalizing mode collapse to ensure the ensemble adequately spans the underlying stochasticity.

D Global Temporal Properties of the Datasets

We present the tables summarizing the global temporal properties for the datasets used in our experimental setup in Tables 3-8.

Our characterization included standard descriptive statistics (mean, standard deviation, skewness, and kurtosis) for each nodal time series. We also assessed three global characteristics for each node: stationarity, long-range dependence, and nonlinearity. Stationarity, a key assumption for classical forecasting models like ARMA, was evaluated using the Augmented Dickey-Fuller (ADF) test (Dickey and Fuller [1979]) at a significance level of 0.05; a time series is considered non-stationary for a p -value > 0.05 . Long-range dependence, which reflects the self-similarity of a time series and is crucial for probabilistic modeling, was quantified using the Hurst exponent. Values below 0.5 indicate mean-reverting (anti-persistent) behavior, 0.5 suggests a random walk (Brownian motion), and values above 0.5 indicate a trending (persistent) series. Finally, to assess the presence of nonlinear dynamics at each node, Teräsvirta's neural network test (Teräsvirta et al. [1993]) at a significance level of 0.05 was employed. Under this framework, the null hypothesis postulates linearity; therefore, a p -value < 0.05 signifies a statistically significant departure from linearity, confirming the nonlinear nature of the time series.

The analysis revealed distinct behaviors across the datasets. The tuberculosis time series for both Japan and China were found to be predominantly non-stationary while uniformly exhibiting long-range dependence. Specifically, all prefectures in Japan (except Yamagata, Kyoto, and Okinawa) and all provinces in China (except Jiangxi and Hainan) were non-stationary. Japan's TB data typically exhibits a decreasing trend (and hence, linearity in many nodes), reflecting Japan's effective and aggressive combat against the disease⁴. In contrast, the majority of nodes in the remaining datasets were stationary, with the exception of New Jersey, and most exhibited long-range dependence. Similarly, all provinces in Belgium's COVID-19 data and all counties in Hungary's chickenpox data were stationary and showed strong long-range dependence, with only a few locations in Belgium (Brabant Wallon, Luxembourg, and Namur) identified as mean-reverting series.

⁴https://www.mofa.go.jp/announce/announce/2008/7/1182066_1030.html

Table 3: Global characteristics of Japan’s TB dataset.

Node No.	Node Name	Mean	STD	Range	Skewness	Kurtosis	ADF p-value	Hurst Exponent	Teräsvirta p-value
1	Hokkaido	71	25.74	[26, 163]	0.8	0	0.24	0.81	0.00
2	Aomori	24.05	9.98	[8, 61]	0.87	0.56	0.45	0.76	0.59
3	Iwate	17.5	7.86	[5, 48]	1.1	1.51	0.32	0.71	0.09
4	Miyagi	27.59	11.55	[6, 71]	0.92	0.6	0.5	0.73	0.01
5	Akita	14.52	6.91	[2, 38]	0.82	0.47	0.27	0.71	0.63
6	Yamagata	13.43	5.99	[3, 36]	1.31	2.08	0.01	0.72	0.49
7	Fukushima	26.02	11.3	[7, 75]	1.11	1.65	0.71	0.73	0.02
8	Ibaragi	43.38	13.17	[22, 84]	0.68	-0.19	0.77	0.71	0.39
9	Tochigi	27.51	9.59	[9, 59]	0.77	0.21	0.07	0.67	0.07
10	Gunnma	25.23	10.08	[10, 70]	1.18	1.99	0.59	0.7	0.24
11	Saitama	111.5	27.39	[53, 232]	0.91	1.35	0.81	0.74	0.13
12	Chiba	106.15	30.01	[53, 190]	0.64	-0.15	0.48	0.78	0.09
13	Tokyo	289.13	63.62	[165, 544]	0.5	0.51	0.95	0.77	0.44
14	Kanagawa	150.27	37.59	[89, 306]	0.94	1.11	0.71	0.76	0.50
15	Niigata	31.31	11.97	[11, 65]	0.66	-0.18	0.69	0.72	0.09
16	Toyoama	17.44	7.54	[5, 48]	0.9	0.77	0.5	0.7	0.01
17	Ishikawa	18.12	7.35	[4, 47]	1.01	1.31	0.63	0.69	0.13
18	Fukui	11.81	4.76	[2, 29]	0.69	0.63	0.87	0.64	0.24
19	Yamanashi	9.9	4.38	[2, 28]	0.76	0.85	0.05	0.7	0.71
20	Nagano	20.34	6.33	[7, 42]	0.68	1.05	0.23	0.66	0.44
21	Gifu	42.79	14.53	[18, 107]	1.05	1.65	0.65	0.73	0.10
22	Shizuoka	61.15	17.83	[30, 130]	0.45	0	0.55	0.72	0.11
23	Aichi	151.2	37.73	[76, 280]	0.64	0.21	0.67	0.82	0.00
24	Mie	30.3	10.87	[8, 68]	0.7	0.23	0.69	0.69	0.01
25	Shiga	20.75	7.46	[6, 49]	0.79	0.85	0.58	0.71	0.01
26	Kyoto	59.57	28.43	[20, 178]	1.98	4.58	0.03	0.76	0.22
27	Osaka	280.49	113.18	[119, 623]	0.94	-0.11	0.4	0.87	0.01
28	Hyogo	127.13	48.09	[57, 320]	1.1	0.63	0.42	0.8	0.00
29	Nara	27.9	9.69	[9, 58]	0.68	-0.11	0.58	0.73	0.04
30	Wakayama	22.69	9.41	[4, 57]	1.03	0.93	0.56	0.73	0.00
31	Tottori	9.38	4.35	[1, 27]	0.91	1.32	0.23	0.61	0.23
32	Shimane	11.66	4.28	[3, 27]	0.56	0.36	0.42	0.66	0.64
33	Okayama	30.54	10.85	[11, 63]	0.75	0.34	0.7	0.72	0.26
34	Hiroshima	44.77	14.48	[17, 91]	0.77	0.03	0.7	0.76	0.62
35	Yamaguchi	27.09	12.09	[9, 71]	1.05	0.83	0.46	0.78	0.26
36	Tokushima	16.94	7.43	[5, 42]	1.08	1.06	0.46	0.75	0.03
37	Kagawa	19.31	7.87	[4, 52]	0.84	0.91	0.44	0.72	0.02
38	Ehime	23.14	8.83	[8, 49]	0.83	0.42	0.4	0.75	0.34
39	Kochi	14.84	6.82	[1, 40]	0.82	0.34	0.34	0.7	0.13
40	Fukuoka	97.16	30.8	[38, 201]	0.81	0.24	0.67	0.81	0.10
41	Saga	15.06	5.29	[2, 33]	0.36	0.2	0.37	0.62	0.08
42	Nagasaki	31.32	10.01	[11, 63]	0.63	0.02	0.64	0.69	0.65
43	Kumamoto	30.69	8.46	[14, 60]	0.64	0.3	0.76	0.64	0.08
44	Oita	24.4	9.64	[9, 69]	1.5	3.08	0.22	0.72	0.14
45	Miyazaki	19.09	8.2	[4, 50]	1.05	0.91	0.21	0.66	6.54E-07
46	Kagoshima	34.04	11.7	[10, 65]	0.58	-0.26	0.37	0.74	0.45
47	Okinawa	24.51	6.86	[9, 45]	0.35	-0.28	0	0.63	0.31

E Baseline Models

In this section, we briefly describe the baseline models used to compare the model performances on real datasets.

1. **LSTM:** The Long Short-Term Memory (LSTM) network ([Hochreiter and Schmidhuber \[1997\]](#)) is a specialized architecture of RNNs designed to overcome the vanishing gradient problem, thereby enabling the modeling of long-range temporal dependencies. The memory cell state in LSTM is regulated by three distinct gating mechanisms:

Table 4: Global characteristics of China’s TB dataset.

Node No.	Node Name	Mean	STD	Range	Skewness	Kurtosis	ADF p-value	Hurst Exponent	Teräsvirta p-value
1	Beijing	576.68	70.15	[397, 706]	-0.29	-0.61	0.62	0.56	0.00
2	Tianjin	266	38.01	[171, 344]	-0.4	0.1	0.63	0.58	0.59
3	Hebei	2731.63	341.66	[1755, 3369]	-0.42	-0.06	0.99	0.6	0.00
4	Shanxi	1218.1	193.28	[854, 1625]	0	-0.63	0.78	0.64	0.00
5	Inner Mongolia	1040.45	168.35	[733, 1433]	0.47	-0.4	0.97	0.76	0.00
6	Liaoning	1986.65	258.02	[1357, 2584]	0.12	-0.41	0.63	0.69	0.00
7	Jilin	1209.37	231.38	[737, 1732]	0.3	-0.49	0.68	0.65	0.00
8	Heilongjiang	2507.3	488.15	[1489, 3598]	0.05	-0.62	1	0.56	0.00
9	Shanghai	547.65	65.84	[388, 657]	-0.3	-0.8	0.66	0.55	0.02
10	Jiangsu	2418.22	371.02	[1609, 3193]	-0.18	-0.43	0.96	0.57	0.00
11	Zhejiang	2281.55	301.3	[1731, 2825]	-0.11	-1.11	0.49	0.57	0.00
12	Anhui	2893.8	353.49	[2094, 3721]	0.16	-0.5	0.98	0.63	0.00
13	Fujian	1425.73	177.96	[1046, 1807]	-0.14	-0.62	0.82	0.63	0.00
14	Jiangxi	3101.47	2882.15	[1976, 24882]	7.37	53.22	0	0.55	0.51
15	Shandong	2588.25	459.76	[1670, 4059]	0.73	0.95	0.75	0.57	0.00
16	Henan	4780.77	522.39	[3242, 5769]	-0.34	0.25	0.84	0.62	0.00
17	Hubei	3549.92	497.49	[2518, 4550]	-0.14	-0.7	1	0.6	0.00
18	Hunan	4507.5	566.54	[3443, 5801]	0.22	-0.77	0.69	0.63	0.00
19	Guangdong	6556.75	795.79	[4484, 7976]	-0.44	-0.54	0.97	0.61	0.00
20	Guangxi	3626.18	556.43	[2623, 5086]	0.35	-0.37	0.82	0.59	0.00
21	Hainan	693.97	84.28	[485, 857]	-0.34	-0.42	0	0.58	0.30
22	Chongqing	1889.9	289.03	[1328, 2645]	0.32	0.03	0.81	0.63	0.00
23	Sichuan	4412.45	571.64	[3307, 6044]	0.36	-0.02	1	0.6	0.00
24	Guizhou	3708.45	545.25	[2530, 5251]	0.32	0.43	1	0.55	0.00
25	Yunnan	2237.87	297.6	[1616, 3004]	0.29	0.57	0.99	0.59	0.00
26	Tibet	413.55	85.75	[176, 593]	-0.44	0.3	0.98	0.67	0.00
27	Shaanxi	1821.4	242.03	[1462, 2855]	1.38	3.68	0.72	0.62	0.06
28	Gansu	1181.68	282.9	[622, 2039]	0.37	0.24	1	0.74	0.00
29	Qinghai	616.07	116.13	[375, 964]	0.35	-0.01	0.1	0.71	0.06
30	Ningxia	236.67	49.81	[144, 394]	0.74	0.97	0.62	0.73	0.04
31	Xinjiang	4153.5	1370.1	[2212, 8628]	1.46	1.87	1	0.69	0.43

the forget gate, which determines what information to discard from the previous state; the input gate, which controls the integration of new information; and the output gate, which modulates the information passed to the next hidden state. Although LSTMs are popular for modeling long-range dependencies, [Zhao et al. \[2020\]](#) show that they are short memory processes under mild assumptions.

- NHiTS:** The Neural Hierarchical Interpolation for Time Series (NHiTS) ([Challu et al. \[2023\]](#)) is an advanced neural forecasting architecture designed to address the challenges of long-horizon forecasting by significantly reducing computational complexity and mitigating the effects of high-frequency noise. Building upon the basis-expansion principles of NBeats ([Oreshkin et al. \[2019\]](#)), NHiTS introduces a hierarchical multi-rate sampling approach that employs distinct interpolation layers at various scales. This architecture decomposes the signal by processing different frequency components across its blocks, utilizing subsampling and subsequent interpolation to reconstruct the forecast.
- Transformers:** The Transformer architecture, originally introduced by [Vaswani et al. \[2017\]](#) in the context of natural language processing, has revolutionized time series forecasting by replacing recurrent structures with self-attention mechanisms. Unlike sequential models, Transformers process entire sequences in parallel, utilizing multi-head attention to capture dependencies between time steps regardless of their temporal distance. This allows the model to assign dynamic weights to past observations based on their relevance to the current forecast horizon. To preserve temporal order, the architecture incorporates positional encodings into the input embeddings.
- TCN:** The Temporal Convolutional Network (TCN) ([Bai \[2018\]](#)) is a specialized 1D convolutional architecture designed for sequence modeling that serves as an alternative to RNNs. TCNs are defined by two primary characteristics: the use of causal convolutions, which ensure no information leakage from the future to the past, and dilated convolutions, which allow the network’s receptive field to grow exponentially with its depth. This enables the model to capture long-range temporal dependencies with significantly fewer layers than standard convolutions. Moreover, the architecture incorporates residual blocks to facilitate the training of deeper networks and mitigate the vanishing

Table 5: Global characteristics of USA's ILI dataset.

Node No.	Node Name	Mean	STD	Range	Skewness	Kurtosis	ADF p-value	Hurst Exponent	Teräsvirta p-value
1	Alabama	336.61	347.18	[13, 1938]	2.13	4.93	0	0.76	0.01
2	Alaska	18.16	18.87	[0, 116]	2.11	5.28	0	0.72	0.04
3	Arizona	304.68	225.1	[56, 1297]	1.6	2.93	0	0.77	0.02
4	Arkansas	65.26	87.15	[0, 525]	2.13	4.83	0	0.72	2.52E-09
5	California	833.96	461.23	[91, 2452]	1.07	0.8	0	0.72	0.20
6	Colorado	123.79	145.14	[0, 891]	2.29	5.86	0	0.78	0.02
7	Connecticut	42.34	53.39	[0, 272]	1.85	3.59	0	0	0.29
8	Delaware	15.71	27.57	[0, 157]	2.69	7.77	0	0	0.33
9	Florida	284.18	194.97	[9, 1165]	1.29	2.34	0	0.77	0.46
10	Georgia	557.41	468.69	[1, 2489]	1.5	2.17	0.05	0.82	0.02
11	Hawaii	87.91	100.43	[2, 603]	2.05	4.77	0	0.88	0.00
12	Idaho	54.03	59.9	[0, 301]	1.73	3.1	0	0	0.42
13	Illinois	901.93	511.59	[244, 3569]	1.5	3.69	0	0.71	0.00
14	Indiana	109.56	135.33	[5, 902]	3.12	11.77	0	0.74	0.11
15	Iowa	33.11	45.32	[0, 302]	2.41	7.89	0	0	0.08
16	Kansas	94.88	117.49	[0, 555]	1.87	2.97	0	0.74	0.01
17	Kentucky	96.84	133.63	[0, 746]	2.21	5.45	0	0.73	0.00
18	Louisiana	810.6	620.94	[35, 3473]	1.61	2.94	0	0.8	0.01
19	Maine	45.82	32.63	[2, 213]	2.12	6	0	0.79	0.00
20	Maryland	125.27	77.21	[4, 467]	1.4	2.52	0	0.74	0.00
21	Massachusetts	263.47	152.1	[22, 961]	1.49	2.77	0	0.77	1.69E-05
22	Michigan	173.43	142.71	[10, 720]	1.48	2.07	0	0.78	0.10
23	Minnesota	61.06	47.31	[2, 302]	1.55	3.2	0	0.76	0.69
24	Mississippi	559.02	354.32	[104, 2359]	1.76	3.92	0	0.79	0.00
25	Missouri	106.36	111.77	[0, 528]	1.37	1.49	0	0.72	0.05
26	Montana	6.69	10.78	[0, 71]	2.67	8.43	0	0	0.12
27	Nebraska	46.29	63.62	[1, 454]	3.18	13.1	0	0.79	0.79
28	Nevada	160.62	163.92	[6, 784]	1.78	2.84	0	0.79	0.67
29	New Hampshire	13.37	18.4	[0, 149]	3.18	13.92	0	0.75	0.00
30	New Jersey	138.89	136.78	[1, 894]	2.1	6.9	0.1	0.86	0.07
31	New Mexico	190.13	140.28	[8, 699]	1.55	2.04	0	0.72	0.05
32	New York	163.67	164.81	[0, 744]	1.41	1.36	0	0.82	0.01
33	North Carolina	194.97	230.75	[0, 1406]	2.72	9.11	0	0.73	0.03
34	North Dakota	17.51	24.58	[0, 170]	2.58	9.21	0	0.79	2.29E-06
35	Ohio	116.13	120.59	[1, 835]	2.27	6.64	0	0.73	1.21E-07
36	Oklahoma	88.88	96.08	[0, 511]	1.45	1.86	0	0.72	2.45E-05
37	Oregon	31.74	35.21	[0, 219]	1.96	4.67	0	0.74	0.00
38	Pennsylvania	208.09	158.48	[40, 893]	1.85	3.68	0	0.77	4.89E-06
39	Rhode Island	28.74	43.1	[0, 286]	2.87	9.79	0	0.73	1.70E-05
40	South Carolina	49.02	80.72	[0, 726]	4.28	25.24	0	0.73	0.01
41	South Dakota	65.56	53.84	[0, 275]	1.21	1.38	0	0.77	0.01
42	Tennessee	123.9	147.2	[0, 841]	2.08	5.02	0	0.75	0.01
43	Texas	1068.6	756.48	[189, 4821]	1.97	4.51	0	0.78	5.17E-07
44	Utah	303.95	233.37	[0, 1282]	1.47	2.6	0	0.8	0.21
45	Vermont	48.3	41.75	[0, 259]	1.96	4.99	0	0.79	0.07
46	Virginia	1428.67	1159.25	[155, 9716]	2.97	13.43	0	0.71	4.51E-06
47	Washington	38.9	38.63	[0, 231]	1.76	3.57	0	0.75	0.18
48	West Virginia	165.21	190.98	[5, 1116]	2.49	7.19	0	0.75	0.10
49	Wisconsin	58.05	62.59	[0, 428]	1.67	3.96	0	0.81	0.00
50	Wyoming	40.34	52.5	[0, 336]	2.41	6.97	0	0.76	1.08E-08

gradient problem. TCNs benefit from massive parallelism during training, as convolutions can be computed across the entire sequence simultaneously, making them highly efficient for large-scale temporal forecasting tasks.

5. **STARMA:** The Space-Time Autoregressive Moving Average (STARMA; Pfeifer and Deutch [1980]) model is a specialized class of spatiotemporal models designed to capture systematic dependencies in data observed across both space and time. It extends the univariate Box-Jenkins ARIMA framework by representing a single variable as a linear combination of its past observations and errors, lagged in both dimensions. STARMA incorporates $N \times N$

Table 6: Global characteristics of Belgium's COVID-19 dataset.

Node No.	Node Name	Mean	STD	Range	Skewness	Kurtosis	ADF p-value	Hurst Exponent	Teräsvirta p-value
1	Antwerpen	877.6	1391.49	[9, 11873]	3.67	17.68	0.01	0.86	0.19
2	BrabantWallon	191.16	334.6	[0, 3004]	3.93	19.73	0.01	0	0.78
3	Brussels	615.33	925.16	[0, 6839]	3.88	17.54	0	0.87	0.81
4	Hainaut	581.7	1040.44	[0, 8706]	4.09	20.69	0	0.85	0.14
5	Limburg	395.23	689.45	[0, 5711]	3.78	18.05	0.03	0.86	0.04
6	Liege	451.17	846.35	[0, 6996]	3.68	16.24	0	0.85	0.00
7	Luxembourg	118.84	235.89	[0, 1958]	4.42	24.11	0	0	0.44
8	Namur	219.06	388.4	[0, 3198]	3.97	19.92	0	0	0.02
9	OostVlaanderen	744.99	1222.12	[0, 11526]	3.94	20.83	0.01	0.86	0.34
10	VlaamsBrabant	515.82	847.77	[0, 6931]	3.53	16.31	0.01	0.86	0.72
11	WestVlaanderen	564.27	993.44	[0, 8858]	4.22	23.7	0	0.86	0.21

Table 7: Global characteristics of Colombia's dengue dataset.

Node No.	Node Name	Mean	STD	Range	Skewness	Kurtosis	ADF p-value	Hurst Exponent	Teräsvirta p-value
1	Amazonas	6.05	11.32	[0, 126]	5.86	45.88	0	0	0.02
2	Antioquia	119.1	193.49	[1, 1335]	3.51	13.37	0	0	0.12
3	Arauca	16.94	20.47	[1, 186]	3.49	15.98	0	0.85	0.00
4	Atlantico	80.23	89.61	[2, 674]	2.75	10.03	0	0.85	0.02
5	Bogota	4.49	2.79	[0, 13]	-0.22	-1.45	0.49	0	0.00
6	Bolivar	52.43	66.43	[1, 520]	3.16	14.09	0.07	0.89	0.55
7	Boyaca	11.44	13.32	[1, 103]	2.55	8.18	0.01	0.9	7.31E-13
8	Caldas	9.33	11.21	[1, 93]	2.79	11.63	0	0	7.25E-07
9	Caqueta	14.33	17.52	[1, 121]	3.04	11.56	0	0.83	0.93
10	Casanare	40.85	41.79	[2, 308]	2.64	9.49	0	0.82	0.01
11	Cauca	11.27	11.6	[1, 96]	3.06	13.01	0	0.86	2.01E-05
12	Cesar	51.74	47.37	[1, 297]	1.64	3.14	0	0.91	6.71E-05
13	Choco	5.7	6.64	[0, 77]	3.4	20.7	0	0	0.00
14	Cordoba	37.35	38.23	[1, 166]	1.46	1.22	0	0.9	8.12E-08
15	Cundinamarca	44.83	42.43	[1, 286]	1.73	3.31	0	0.89	1.31E-07
16	Guainia	2.63	3.24	[0, 22]	2.84	8.8	0	0	0.00
17	Guajira	19.32	20.02	[1, 148]	2.16	6.61	0.48	0	0.14
18	Guaviare	6.96	7.75	[1, 53]	2.22	5.52	0	0	7.69E-08
19	Huila	81.48	72.77	[6, 412]	1.74	3.2	0	0.89	0.01
20	Magdalena	26.05	26.05	[1, 176]	1.95	5.13	0	0.88	0.18
21	Meta	95.46	91.67	[10, 639]	2.69	10.17	0	0.9	0.86
22	Narino	6.68	5.8	[0, 41]	1.42	3.06	0.03	0	1.50E-09
23	Norte Santander	84.52	56.88	[5, 300]	1.08	0.92	0.01	0.9	0.06
24	Putumayo	19.34	17.94	[1, 131]	2.09	5.86	0	0.84	0.09
25	Quindio	34.77	62.56	[1, 598]	5.55	38.19	0	0.91	0.33
26	Risaralda	26.42	73.56	[1, 684]	5.68	35.44	0	0.9	0.00
27	San andres	1.95	2.24	[0, 30]	5.45	44.18	0	0	0.00
28	Santander	142.65	130.42	[8, 756]	1.65	3.33	0.01	0.91	0.56
29	Sucre	42.74	42.8	[1, 251]	2.1	4.86	0	0.88	0.00
30	Tolima	112.87	100.95	[14, 518]	1.56	1.87	0.01	0.9	3.25E-05
31	Valle	210.16	235.2	[1, 1460]	2.17	5.64	0	0.87	0.00
32	Vaupes	1.38	1.66	[0, 19]	6.47	52.64	0.01	0	0.00
33	Vichada	3.46	4.43	[0, 43]	4.14	23.26	0	0	0.44

spatial weight matrices, which define the hierarchical relationship between different locations (such as countries or states) to account for spatial correlation and heterogeneity.

- GSTAR:** The Generalized Space-Time Autoregressive (GSTAR) model (Ruchjana et al. [2012]) is a modeling framework designed to capture spatiotemporal dependencies in multivariate time series. As an extension of the standard STAR model, GSTAR relaxes the assumption of spatial homogeneity by allowing the autoregressive

Table 8: Global characteristics of Hungary’s chickenpox dataset.

Node No.	Node Name	Mean	STD	Range	Skewness	Kurtosis	ADF p-value	Hurst Exponent	Teräsvirta p-value
1	Bács	37.17	36.84	[0, 274]	1.79	5.35	0	0.76	4.28E-13
2	Baranya	34.2	32.57	[0, 194]	1.37	2.25	0	0.77	6.86E-13
3	Békés	28.91	37.62	[0, 271]	2.48	8.12	0	0.83	0.95
4	Borsod	57.08	50.73	[0, 355]	1.39	3.08	0	0.74	4.81E-12
5	Budapest	101.25	76.35	[0, 479]	0.95	1.4	0	0.74	2.07E-14
6	Csongrád	31.49	33.79	[0, 199]	1.66	3.11	0	0.75	0.19
7	Fejér	33.27	31.4	[0, 164]	1.11	0.71	0	0.82	6.36E-11
8	Győr	41.44	36.01	[0, 181]	1.02	0.74	0	0.78	1.04E-08
9	Hajdú	47.1	44.61	[0, 262]	1.4	2.31	0	0.77	3.12E-08
10	Heves	29.69	31.86	[0, 210]	1.94	4.88	0	0.81	0.03
11	Jasz	40.87	37.28	[0, 224]	1.12	1.13	0	0.8	5.26E-07
12	Komárom	25.64	24.47	[0, 160]	1.4	2.75	0	0.8	1.78E-08
13	Nógrád	21.85	22.03	[0, 112]	1.4	2	0	0.83	2.87E-07
14	Pest	86.1	66.77	[0, 431]	0.87	1.13	0	0.76	3.33E-16
15	Somogy	27.61	26.72	[0, 155]	1.41	2.23	0	0.74	6.19E-06
16	Szabolcs	29.85	31.81	[0, 203]	1.89	5.26	0	0.74	3.84E-07
17	Tolna	20.35	23.27	[0, 131]	1.71	2.96	0	0.82	0.01
18	Vas	22.47	25.01	[0, 141]	1.67	3.12	0	0.82	0.00
19	Veszprém	40.64	40.7	[0, 230]	1.57	3.03	0	0.81	0.01
20	Zala	19.87	22	[0, 216]	2.37	12.34	0	0.79	2.41E-13

parameters to vary across different locations. This flexibility makes it particularly effective for modeling phenomena where spatial units exhibit heterogeneous characteristics. The model utilizes location-specific weights (represented through weights matrices W) to account for the proximity and influence of neighboring sites, combining temporal lags and spatial lags into a unified linear system.

7. **STGCN:** The Spatio-Temporal Graph Convolutional Network (STGCN), proposed by [Yu et al. \[2018\]](#), is a novel deep learning framework designed to address the challenges of time series prediction in the traffic domain by modeling multi-scale traffic networks. Unlike traditional approaches that rely on regular convolutional or recurrent units, STGCN is built with a complete convolutional structure on graphs. The architecture consists of several spatio-temporal convolutional blocks, each featuring a sandwich structure where two gated temporal convolution layers flank a spatial graph convolution layer.
8. **DeepAR:** DeepAR ([Salinas et al. \[2020\]](#)) is a probabilistic forecasting methodology that utilizes RNNs to learn a global model from a large collection of related time series. Unlike classical methods that fit parameters to individual series, DeepAR shares information across the dataset, allowing it to capture complex seasonal patterns and provide forecasts for items with little historical data. The architecture employs an encoder-decoder framework where the network’s output parametrizes a chosen likelihood function, such as Gaussian for real-valued data or negative binomial for count data.
9. **Probabilistic iTransformer:** The Inverted Transformer (iTransformer; [Liu et al. \[2023\]](#), [Alexandrov et al. \[2020\]](#)) architecture applies Transformers to multivariate time series forecasting by inverting the standard data modality. Unlike vanilla Transformers that embed multiple variates of a single timestamp into temporal tokens, iTransformer embeds the entire historical sequence of each individual variate into its own variate token. This inverted approach allows the self-attention mechanism to explicitly capture multivariate correlations between variate tokens, while the shared feed-forward network (FFN) learns nonlinear, global temporal representations for each series independently.
10. **GpGp:** The Fast Gaussian Process (GpGp) method ([Guinness \[2018\]](#)), represents a sophisticated refinement of Vecchia’s approximation ([Vecchia \[1988\]](#)), specifically optimized for the analysis of large-scale spatiotemporal datasets. This approach streamlines the computational complexity of traditional Gaussian Process regression by introducing a grouping mechanism for ordered sequences, which allows for highly efficient likelihood evaluation and parameter estimation. A defining advantage of the GpGp framework is its interpolative nature; as a continuous spatial predictor, it can generalize beyond the observed data points to forecast values for specific coordinates (longitude and latitude) that were not originally present in the training set.
11. **DiffSTG:** DiffSTG ([Wen et al. \[2023\]](#)) is a non-autoregressive probabilistic forecasting framework that generalizes denoising diffusion probabilistic models (DDPMs) to spatio-temporal graphs. It utilizes a dedicated denoising

network, UGnet, which integrates a U-Net-based structure for multi-scale temporal modeling with GNNs to capture complex spatial correlations. By implementing a conditional reverse diffusion process, the model learns to reconstruct future graph signals from Gaussian noise, conditioned on historical observations and the underlying graph structure.

12. **Spatiotemporal Echo-State Networks (STESNs):** STESN (Huang et al. [2022]) captures nonlinear spatiotemporal dynamics by mapping inputs to high-dimensional reservoir states. These states evolve via the fixed nonlinear dynamics, where the weight matrices are sparse, random, and fixed. The output is formulated with quadratic interactions to model complex physical processes. Unlike standard RNNs, only the output matrices are trained using a closed-form ridge regression estimator. To ensure computational tractability over large domains, the model is applied to a reduced set of n^* spatial knots and then reconstructed via kriging. Uncertainty quantification is done via empirical calibration by estimating specific quantiles.

E.1 Implementation Details

We implemented the NHITS, Transformers, TCN, and DeepAR models using the Darts library (Herzen et al. [2022]) in Python. The STARMA, GSTAR, and GpGp were built using the `starma`, `gstar`, and `GpGp` packages respectively, in the R statistical software. For STGCN, we utilized the PyTorch implementation in PyTorch Geometric Temporal⁵ (Rozemberczki et al. [2021b]). The probabilistic iTransformer was implemented using GluonTS (Alexandrov et al. [2020]) with a PyTorch backend, and the default implementations were used for DiffSTG⁶ and STESN⁷. The multivariate LSTM and the proposed MVEN, GCEN, and STEN models were implemented using the PyTorch framework in Python, offering seamless training and inference on GPUs.

The proposed and baseline deep learning models were trained on an NVIDIA P100 GPU with 16 GB RAM. For GSTAR, STARMA, and GpGp, we utilized an Intel(R) Xeon(R) CPU with 4 cores and 30 GB RAM. The default STESN implementation is based on NumPy and SciPy, and does not natively support training and inference on GPUs, so we used an Intel(R) Xeon(R) CPU with 20 cores and 126 GB RAM. The time taken by the models for both training and inference (in the evaluation setup of 50 independent runs) is presented in Table 9. Time consumption mainly depends on the training device (whether GPU or CPU), and hyperparameter configuration of the models, such as the number of hidden layers and size of the embedding dimension. The STESN model was the most time-consuming as compared to others, in our evaluation setup. The predictive uncertainty profile was assessed directly from the raw STESN forecast ensembles, bypassing the empirical calibration procedure suggested in the original framework. Furthermore, as the target forecast domain was restricted to the spatial points within the established training grid, all nodes were used in fitting the ESN. The spatial kriging step, typically utilized for interpolation at unobserved locations, was omitted. For DiffSTG, we utilized the same adjacency matrices (Fig. 17) that were used in training GCEN.

Table 9: Total time consumed (in seconds) to train the models and evaluate them across 50 independent evaluation runs. The deterministic models (LSTM-STGCN) are evaluated in a single run only.

Dataset	Horizon	LSTM	NHITS	Transformers	TCN	GSTAR	STARMA	STGCN	DeepAR	Prob-iTransformer	GpGp	DiffSTG	STESN	MVEN	GCEN	STEN
Japan TB	6-month	4.59	6.64	11.4	3.39	2.46	0.16	300	6.53	111.82	1019.35	5266.52	9026.05	15.77	15.4	6.62
	12-month	1.68	6.08	8.93	3.01	2.44	0.15	673	7.18	116.97	1015.88	4776.41	9224.47	26.69	12.4	11.27
	24-month	1.99	5.19	3.25	1.17	2.46	0.15	836	8.6	123.44	783.37	4814.27	461.9	7.96	18.3	38.88
China TB	6-month	0.61	2.41	3.72	1.14	0.35	0.069	56	4.77	110.7	150.61	4740.22	26.14	2.77	5.54	6.18
	12-month	0.42	1.42	3.16	1.2	0.35	0.07	50	5.25	114.01	148.7	4819.17	27.56	3.36	4.75	5.48
USA ILI	4-week	8.17	9.54	14.3	4.68	16.61	0.21	1293	8.31	117.83	1972.37	5569.36	9689.09	20.94	37.07	51.22
	9-week	5.97	8.91	14.4	4.66	15.31	0.21	1244	8.8	120.27	2030.99	5615.99	9694.36	13.31	26.9	11.57
	13-week	22.7	8.8	14.5	4.63	15.37	0.21	1205	9.37	122.87	2105.11	5770.92	9744.84	13.46	12.25	21.81
Belgium COVID-19	30-day	7.69	19.2	27.8	11.4	2.78	0.04	7155	16.33	113.57	713.31	4930.86	10778.94	32	81	10.2
	60-day	5.01	16.2	25.6	9.4	5.4	0.04	9468	17.43	117.28	692.75	4919.1	10869.83	15.1	150	18
	90-day	41.8	14.2	24.5	8.4	8.7	0.044	10838	19.4	120.44	695.07	5037.91	10744.37	8.12	29.2	32.3
Colombia Dengue	4-week	25	23.8	37.4	11.6	12.94	0.24	3473	15.24	127.55	3010.38	4975.49	11304.18	16.71	24.44	93.96
	9-week	7.65	23.4	37.4	11.5	12.37	0.244	3354	15.5	124.95	3079.72	4897.05	11391.19	113.91	41.99	31.61
	13-week	23	23.5	33.4	11.2	12.36	0.24	3320	15.82	126.8	2986.14	4953.34	11317.98	60.02	14.22	106.49
Hungary Chickenpox	4-week	8.79	15.1	21	7.27	2.08	0.14	2143	12.63	125.09	1021.59	4648.87	10090.61	14.07	32.92	9.87
	9-week	4.05	13.6	22.4	7.1	2.22	0.126	2048	10.86	108.2	1001.36	4614.07	10035.31	75.40	23.42	51.04
	13-week	9.66	13.6	22.4	7.11	2.22	0.122	2049	11.22	110.74	985.69	4769.56	10022.03	10.60	13.25	13.12

Hyperparameters for the proposed models were optimized over 100 trials using the Optuna framework (Akiba et al. [2019]) by minimizing the CRPS on the corresponding holdout validation sets. The validation set length for hyperparameter tuning was adjusted according to the forecast term and temporal granularity of the dataset. Specifically, the validation lengths for short, medium, and long-term forecast horizons were set to 60, 90, and 120 days for the daily data; 9, 13, and 26 weeks for the weekly data; and 12, 24, and 36 months for the monthly data, respectively, as shown in Fig. 5. The hyperparameter search space encompassed the output dimensionality of the spatial module, bounded between 1

⁵https://github.com/benedekrozemberczki/pytorch_geometric_temporal

⁶<https://github.com/wenhaomin/DiffSTG>

⁷<https://github.com/hhuang90/KSA-wind-forecast>

and 10; the hidden state dimensionality of the LSTM module, constrained between 2 and 100; the depth of the LSTM network, ranging from 1 to 5 layers; the LSTM dropout rate, sampled continuously from $[0.0, 0.5]$; the learning rate, sampled from $[10^{-5}, 0.1]$; and the decay parameter α and maximum spatial lags L for STEN (see Sec. 4.2) chosen from $\{1, 2, 3\}$. Following optimization, the best-performing hyperparameters were used to train the final models on the combined training and validation data prior to evaluation. The networks were trained via backpropagation using the energy score loss and the Adam optimizer (Kingma and Ba [2014]). With the exception of STGCN, all architectures were trained for 100 epochs. The STGCN was trained for 50 epochs, due to its substantial time consumption.

F Evaluation Metrics

This section provides a comprehensive overview of the performance measures employed to evaluate the proposed models. Our evaluation framework is designed to be nearly exhaustive, as it accounts for both point forecast accuracy and probabilistic calibration. Let $\{\widehat{Y}_t\}_{t=T+1}^{T+q}$ denote the predicted values for $\{Y_t\}_{t=T+1}^{T+q}$, q be the forecast horizon, and $t = \{1, \dots, T\}$ be the time indices for the observed (historical) data $\{Y_t\}_{t=1}^T$.

1. **SMAPE:** The Symmetric Mean Absolute Percentage Error (SMAPE) adjusts for the asymmetry between over-forecasts and under-forecasts and is bounded between 0% and 200%.

$$SMAPE = \frac{100\%}{q} \sum_{t=T+1}^{T+q} \frac{|\widehat{Y}_t - Y_t|}{(|Y_t| + |\widehat{Y}_t|)/2}.$$

2. **MAE:** Mean Absolute Error (MAE) is the average of the absolute differences between the forecasted values (\widehat{Y}_t) and the actual observations (Y_t).

$$MAE = \frac{1}{q} \sum_{t=T+1}^{T+q} |\widehat{Y}_t - Y_t|.$$

3. **RMSE:** Root Mean Squared Error (RMSE) is the square root of the average of squared differences between prediction and observation.

$$RMSE = \sqrt{\frac{1}{q} \sum_{t=T+1}^{T+q} (\widehat{Y}_t - Y_t)^2}.$$

4. **MASE:** Mean Absolute Scaled Error (MASE) scales the MAE by the mean absolute error of a naive forecast produced on the training data.

$$MASE = \frac{\frac{1}{q} \sum_{t=T+1}^{T+q} |\widehat{Y}_t - Y_t|}{\frac{1}{T-1} \sum_{t=2}^T |Y_t - Y_{t-1}|}.$$

5. **RMSSE:** Similar to MASE, the Root Mean Squared Scaled Error (RMSSE) scales the MSE of the forecast by the MSE of a naive baseline, subsequently taking the square root.

$$RMSSE = \sqrt{\frac{\frac{1}{q} \sum_{t=T+1}^{T+q} (\widehat{Y}_t - Y_t)^2}{\frac{1}{T-1} \sum_{t=2}^T (Y_t - Y_{t-1})^2}}.$$

6. **Pinball Loss:** The Pinball loss (Gneiting et al. [2023]) is used to evaluate the accuracy of a quantile forecast. For a target quantile $\tau \in [0, 1]$, the loss is defined as:

$$L_\tau(\mathbf{Y}, \widehat{\mathbf{Y}}) = \frac{1}{q} \sum_{t=T+1}^{T+q} \max \left\{ \tau (Y_t - \widehat{Y}_t), (1 - \tau) (Y_t - \widehat{Y}_t) \right\}.$$

7. **ρ -Risk:** ρ -risk is a normalized version of the Pinball loss, often calculated across a range of quantiles to provide a summary of the distribution's coverage (Seeger et al. [2016], Salinas et al. [2020]).

$$\rho\text{-risk} = \frac{2 \sum_{t=T+1}^{T+q} \max \left\{ \tau (Y_t - \widehat{Y}_t), (1 - \tau) (Y_t - \widehat{Y}_t) \right\}}{\sum_{t=T+1}^{T+q} Y_t}$$

8. **CRPS:** The Continuous Ranked Probability Score (CRPS; [Gneiting and Raftery \[2007\]](#)) generalizes the MAE to the case of probabilistic forecasts. It measures the difference between the predicted cumulative distribution function and the empirical CDF of the observation.

$$CRPS(F, y) = \frac{1}{q} \sum_{t=T+1}^{T+q} \int_{\mathbb{R}} (F_t(y) - \mathbb{I}_{y \geq Y_t})^2 dy$$

where, F_t denotes the predicted probability distribution at time t .

9. **Winkler Score:** The Winkler score ([Winkler et al. \[1996\]](#)) is a strictly proper scoring rule used to assess the quality of predictive confidence intervals by jointly evaluating their width and coverage. For a nominal confidence level $1 - \alpha$, given a prediction interval $[\ell_{\alpha,t}, u_{\alpha,t}]$ at time t and the observed value y_t , the Winkler score $W_{\alpha,t}$ is mathematically defined as:

$$W_{\alpha,t} = \begin{cases} (u_{\alpha,t} - \ell_{\alpha,t}) + \frac{2}{\alpha}(\ell_{\alpha,t} - y_t), & \text{if } y_t < \ell_{\alpha,t} \\ (u_{\alpha,t} - \ell_{\alpha,t}), & \text{if } \ell_{\alpha,t} \leq y_t \leq u_{\alpha,t} \\ (u_{\alpha,t} - \ell_{\alpha,t}) + \frac{2}{\alpha}(y_t - u_{\alpha,t}), & \text{if } y_t > u_{\alpha,t} \end{cases}$$

This formulation assigns the Winkler score as the length of the interval when the true value lies inside it, rewarding narrow intervals. However, when the true value falls outside the interval, the score imposes an additional penalty proportional to the distance the observation lies beyond the interval bounds, scaled by $2/\alpha$. This penalization emphasizes the importance of coverage, discouraging intervals that fail to contain the true values. Consequently, lower Winkler scores indicate better prediction intervals that are simultaneously sharp and well-calibrated.

10. **Probability Integral Transform (PIT):** For every spatiotemporal observation y_{true} in the test set, we compute a PIT value relative to the model's predicted forecast ensemble. Given an ensemble of M generated trajectories, the PIT value is calculated using a rank-based formulation defined as:

$$PIT = \frac{1}{M+1} \sum_{i=1}^M \mathbb{I}(\hat{y}^{(i)} < y_{true})$$

where $\mathbb{I}(\cdot)$ is the indicator function and $\hat{y}^{(i)}$ represents the i -th ensemble member. This formulation interprets the PIT value as the normalized rank of the ground truth relative to the ensemble distribution.

11. **Empirical Coverage:** Empirical coverage is the proportion of times the true values fall within the predicted confidence intervals:

$$\text{Coverage} = \frac{1}{n} \sum_{i=1}^n \mathbb{I}(y_i \in CI_i)$$

where, \mathbb{I} denotes the indicator function, y_i is the true value, and CI_i is the confidence interval for prediction i . For a 95% confidence interval, the best coverage score is 0.95. This metric is often misleading, because a high coverage score, potentially reaching 1.00, can be artificially attained by generating excessively wide intervals (see [Table 13](#)). [Fig. 18](#) illustrates this, where GpGp produces extremely wide intervals and attains 100% coverage on the Belgium dataset. Such results lack sharpness, rendering them impractical for precision-dependent applications such as policy formulation or strategic decision-making. Hence, the intervals are evaluated using the Winkler score in the main text, which simultaneously penalizes both lack of coverage and excessive interval width.

G Tables and Figures

Table 10: Mean forecast performance (along with standard deviations) of the proposed and benchmark models on all six datasets for the short-term forecast horizons (30-day/4-week/6-month). The **best** and **second best** results are highlighted.

Dataset	Metric	Temporal Models				Spatiotemporal Models				Probabilistic Models (Temporal & Spatiotemporal)				ST-Engression Models (Proposed)			
		LSTM	NHTS	Transformers	TCN	GSTAR	STARMA	STGCN	DeepAR	Prob-Transformer	GpCp	DHSTG	STESN	MVEN	GCEN	STEN	
Japan TB	SMAPE	22.04	22.58	22.79	30.26	23.24	27.7	41.16	25.57 (0.42)	35.32 (0.26)	98.26 (3.55)	64.37 (0.99)	23.42 (0.09)	23.99 (0.13)	21.30 (0.14)	23.10 (0.14)	
	MAE	6.09	6.09	5.8	9.08	5.67	6.46	14.99	7.48 (0.20)	10.86 (0.15)	42.81 (3.43)	19.95 (0.38)	5.61 (0.03)	6.82 (0.05)	5.29 (0.05)	6.46 (0.07)	
	RMSE	11.18	7.04	6.28	10.19	8.99	11.11	26.03	13.24 (0.37)	20.67 (0.47)	52.12 (3.02)	26.38 (0.35)	9.18 (0.04)	12.39 (0.12)	9.39 (0.12)	11.78 (0.16)	
	MASE	0.71	0.63	0.63	0.93	0.66	0.75	1.74	0.87 (0.02)	1.26 (0.02)	4.98 (0.40)	2.32 (0.04)	0.65 (0.00)	0.79 (0.01)	0.62 (0.01)	0.75 (0.01)	
	RMSSE	0.84	0.58	0.58	0.84	0.67	0.83	1.95	0.99 (0.03)	1.55 (0.03)	3.90 (0.23)	1.98 (0.03)	0.69 (0.00)	0.93 (0.01)	0.70 (0.01)	0.88 (0.01)	
	Pinball-80	1.82	2.15	2.3	2.58	2.88	2.7	3.09	2.82 (0.05)	3.75 (0.12)	20.44 (0.86)	9.31 (0.13)	2.14 (0.01)	1.99 (0.02)	1.90 (0.02)	2.05 (0.02)	
	Pinball-95	1.21	1.71	2	1.6	2.9	2.43	0.89	1.04 (0.01)	1.28 (0.05)	8.18 (0.25)	3.82 (0.11)	1.56 (0.01)	0.80 (0.01)	0.91 (0.02)	0.85 (0.01)	
	ρ -0.5 Risk	0.19	0.19	0.18	0.28	0.17	0.2	0.46	0.23 (0.01)	0.33 (0.00)	1.32 (0.11)	0.61 (0.01)	0.17 (0.00)	0.21 (0.00)	0.16 (0.00)	0.20 (0.00)	
	ρ -0.9 Risk	0.09	0.11	0.13	0.12	0.18	0.15	0.1	0.11 (0.00)	0.13 (0.01)	0.81 (0.03)	0.38 (0.01)	0.09 (0.00)	0.08 (0.00)	0.08 (0.00)	0.08 (0.00)	
	CRPS	6.09	6.09	5.8	9.08	5.67	6.46	14.99	5.31 (0.11)	7.80 (0.08)	30.81 (1.48)	14.25 (0.21)	5.12 (0.02)	5.97 (0.03)	4.23 (0.03)	5.14 (0.04)	
	Winkler Score	-	-	-	-	-	-	-	48.41 (1.98)	70.02 (1.62)	308.61 (7.42)	132.89 (3.61)	164.18 (1.34)	172.63 (0.89)	79.05 (1.79)	95.13 (2.34)	
	China TB	SMAPE	14.63	14.55	19.06	27.81	21.6	20.86	21.09	19.73 (0.21)	123.04 (0.52)	63.65 (1.12)	65.03 (0.87)	18.93 (0.04)	15.88 (0.10)	12.59 (0.08)	14.73 (0.12)
		MAE	360.46	436.29	475.54	578.56	490.91	292.29	606.41	494.89 (6.21)	1756.88 (2.76)	1217.47 (21.71)	1293.81 (22.18)	468.06 (0.89)	391.07 (3.10)	295.58 (2.07)	342.05 (2.57)
RMSE		816.36	531.64	516.28	618.39	728.55	427.14	1401.16	871.08 (7.57)	2365.15 (2.76)	1677.44 (24.17)	1682.44 (25.83)	803.85 (0.74)	807.22 (5.84)	677.79 (2.65)	794.24 (2.19)	
MASE		1.44	1.2	1.66	2.18	1.96	1.17	2.42	1.98 (0.02)	7.05 (0.01)	5.17 (0.09)	5.17 (0.09)	1.87 (0.00)	1.56 (0.01)	1.18 (0.01)	1.37 (0.01)	
RMSSE		0.95	0.9	1.28	1.66	0.85	0.5	1.63	1.02 (0.01)	2.76 (0.00)	1.96 (0.03)	1.96 (0.03)	0.94 (0.00)	0.94 (0.01)	0.79 (0.00)	0.93 (0.00)	
Pinball-80		164.61	163.04	168.98	293.54	150.69	95.27	194.49	212.44 (1.78)	234.66 (2.85)	530.33 (6.98)	631.04 (8.18)	163.84 (0.22)	172.31 (1.02)	144.95 (0.44)	167.67 (0.77)	
Pinball-95		156.8	135.48	134.59	295.67	103.31	70.89	140.14	124.89 (2.13)	1128.40 (1.84)	243.03 (6.07)	262.48 (5.42)	120.92 (1.48)	125.57 (1.19)	125.05 (0.83)	143.11 (0.96)	
ρ -0.5 Risk		0.18	0.21	0.23	0.28	0.24	0.14	0.29	0.24 (0.00)	0.85 (0.00)	0.59 (0.01)	0.63 (0.01)	0.18 (0.10)	0.19 (0.00)	0.14 (0.00)	0.17 (0.00)	
ρ -0.9 Risk		0.15	0.14	0.14	0.29	0.12	0.08	0.15	0.16 (0.00)	1.19 (0.01)	0.36 (0.01)	0.42 (0.01)	0.14 (0.00)	0.14 (0.00)	0.13 (0.00)	0.15 (0.00)	
CRPS		360.46	436.29	475.54	578.56	490.91	292.29	606.41	402.45 (2.45)	1560.92 (3.68)	925.29 (9.76)	1023.12 (6.67)	448.60 (2.30)	335.04 (2.21)	259.17 (1.26)	303.31 (1.22)	
Winkler Score		-	-	-	-	-	-	-	6767.63 (174.41)	41308.55 (724.21)	10336.87 (364.22)	11141.40 (189.03)	15678.32 (459.52)	8369.24 (123.60)	7600.06 (67.49)	8890.56 (55.77)	
USA ILI		SMAPE	31.33	39.86	53.91	57.62	41.28	36.06	50.65	45.90 (0.57)	81.83 (0.48)	103.79 (1.23)	85.17 (1.25)	28.71 (0.13)	37.17 (0.45)	31.15 (0.24)	32.49 (0.29)
		MAE	89.1	118.65	126.97	177.96	128.32	110.43	151.24	120.80 (1.15)	292.77 (3.19)	410.74 (3.19)	268.10 (1.99)	69.28 (0.32)	119.33 (2.10)	78.06 (1.15)	90.69 (1.34)
	RMSE	187.27	128.46	141.12	185.68	238.04	225.65	303.97	267.24 (4.06)	611.56 (1.00)	657.67 (3.57)	517.34 (3.50)	125.66 (0.89)	245.61 (6.20)	147.83 (2.86)	183.59 (4.34)	
	MASE	2.38	2.87	3.29	4.12	3.43	2.95	4.04	3.23 (0.06)	7.83 (0.02)	10.98 (0.09)	7.17 (0.05)	1.35 (0.01)	3.19 (0.08)	2.09 (0.03)	2.43 (0.04)	
	RMSSE	1.82	1.9	2.15	2.6	2.31	2.19	2.95	2.59 (0.04)	5.94 (0.01)	6.39 (0.03)	5.02 (0.03)	1.22 (0.01)	2.38 (0.06)	1.44 (0.03)	1.78 (0.04)	
	Pinball-80	58.75	91.34	75.89	135.8	101.02	83.95	104.77	60.36 (0.76)	187.13 (0.83)	200.18 (1.27)	155.42 (1.74)	42.52 (0.38)	52.45 (1.91)	38.26 (0.71)	44.76 (1.37)	
	Pinball-95	65.85	107.35	82.09	159.21	119.45	98.32	119.34	42.22 (1.12)	163.26 (2.40)	137.28 (1.78)	122.78 (2.66)	42.25 (0.57)	30.40 (1.67)	27.68 (0.42)	29.15 (1.35)	
	ρ -0.5 Risk	0.23	0.31	0.33	0.46	0.33	0.29	0.39	0.31 (0.01)	0.76 (0.00)	1.07 (0.01)	0.70 (0.01)	0.18 (0.00)	0.31 (0.01)	0.20 (0.00)	0.24 (0.00)	
	ρ -0.9 Risk	0.33	0.53	0.42	0.79	0.59	0.49	0.6	0.27 (0.00)	0.94 (0.01)	0.86 (0.01)	0.74 (0.01)	0.22 (0.00)	0.21 (0.01)	0.17 (0.00)	0.19 (0.01)	
	CRPS	89.1	118.65	126.97	177.96	128.32	110.43	151.24	95.32 (1.19)	251.45 (0.84)	336.26 (1.84)	218.96 (1.81)	63.05 (0.34)	87.82 (1.46)	61.95 (0.61)	69.86 (1.00)	
	Winkler Score	-	-	-	-	-	-	-	1691.99 (43.58)	6160.70 (154.79)	6830.05 (97.82)	4684.26 (127.85)	2011.11 (26.89)	1211.44 (50.65)	1187.96 (21.32)	1122.44 (53.26)	
	Belgium COVID-19	SMAPE	70.71	72.37	97.49	82.72	109.5	97.49	105.22	73.27 (0.64)	78.65 (0.72)	126.89 (25.12)	86.70 (1.36)	62.40 (0.06)	61.60 (0.58)	46.99 (1.08)	68.02 (0.20)
		MAE	81.52	90.76	126.95	177.6	141.8	132.48	343.76	117.87 (2.54)	119.80 (1.14)	232.83 (71.70)	157.74 (5.41)	87.14 (0.12)	86.08 (1.13)	55.13 (0.86)	103.29 (0.54)
RMSE		107.67	115.59	151.97	203.19	207	189.31	421.59	156.11 (2.83)	172.89 (1.22)	293.61 (79.12)	174.38 (5.29)	134.65 (0.12)	144.83 (1.56)	82.02 (1.44)	140.29 (0.68)	
MASE		0.42	0.49	0.66	0.89	0.72	0.68	1.76	0.60 (0.01)	0.61 (0.01)	1.19 (0.37)	0.81 (0.03)	0.44 (0.00)	0.44 (0.01)	0.28 (0.00)	0.53 (0.00)	
RMSSE		0.22	0.27	0.35	0.45	0.42	0.39	0.86	0.32 (0.01)	0.35 (0.00)	0.60 (0.16)	0.36 (0.01)	0.27 (0.00)	0.27 (0.00)	0.22 (0.01)	0.29 (0.00)	
Pinball-80		48.11	35.59	80.64	49.25	93.15	98.06	69.72	47.62 (1.18)	51.68 (0.73)	287.23 (31.08)	59.58 (1.49)	46.05 (0.10)	30.11 (0.71)	22.20 (0.6)	38.30 (0.24)	
Pinball-95		51.79	30.7	89.22	29.47	104.28	113.96	18.64	20.47 (0.58)	24.25 (1.08)	141.83 (10.06)	23.16 (0.55)	45.80 (0.18)	11.85 (0.70)	10.17 (0.32)	20.95 (0.47)	
ρ -0.5 Risk		0.45	0.51	0.72	1	0.8	0.75	1.94	0.67 (0.01)	0.67 (0.01)	1.29 (0.38)	0.90 (0.03)	0.49 (0.00)	0.49 (0.01)	0.33 (0.00)	0.58 (0.00)	
ρ -0.9 Risk		0.55	0.36	0.97	0.41	1.13	1.23	0.4	0.36 (0.01)	0.41 (0.01)	2.49 (1.91)	0.43 (0.01)	0.52 (0.00)	0.22 (0.01)	0.18 (0.00)	0.32 (0.00)	
CRPS		81.52	90.76	126.95	177.6	141.8	132.48	343.76	83.58 (1.52)	90.34 (0.75)	440.50 (25.57)	111.87 (4.05)	84.51 (1.14)	60.71 (0.79)	42.38 (0.59)	81.44 (0.44)	
Winkler Score		-	-	-	-	-	-	-	761.72 (22.68)	1227.73 (39.83)	6796.43 (347.11)	867.90 (52.97)	3160.21 (14.32)	599.41 (20.14)	561.29 (14.58)	1499.49 (37.99)	
Colombia Dengue		SMAPE	32.7	48.98	50.37	73.73	35.89	30.97	82.81	65.61 (0.97)	35.22 (0.57)	105.96 (3.00)	61.42 (0.67)	51.02 (0.75)	43.32 (1.46)	29.24 (1.17)	36.20 (0.99)
		MAE	13.42	16.23	13.29	43.36	12.3	7.99	44.55	26.43 (0.29)	23.25 (0.20)	48.33 (0.85)	24.05 (0.22)	13.41 (0.08)	12.22 (0.33)	8.31 (0.15)	8.24 (0.20)
	RMSE	30.24	17.94	15.05	44.49	24.94	12.73	96.36	55.67 (0.85)	73.55 (0.48)	97.92 (1.04)	62.72 (0.75)	21.74 (0.11)	23.28 (0.29)	13.14 (0.21)	13.22 (0.32)	
	MASE	1.82	2.08	2.02	4.69	1.67	1.08	6.04	3.58 (0.04)	3.15 (0.03)	6.55 (1.02)	3.26 (0.03)	1.82 (0.01)	1.66 (0.04)	1.12 (0.02)	1.12 (0.03)	
	RMSSE	1.98	1.4	1.31	2.88	1.64	0.84	6.32	3.65 (0.06)	4.83 (0.03)	6.43 (0.07)	4.12 (0.05)	1.43 (0.01)	1.53 (0.02)	0.86 (0.01)	0.86 (0.02)	
	Pinball-80	8.23	10.21	7.44	20.78	6.63	4.58	25.72	12.15 (0.20)	12.28 (0.17)	26.96 (0.38)	12.97 (0.18)	5.96 (0.06)	6.22 (0.17)	3.73 (0.08)	3.72 (0.09)	
	Pinball-95	9	11.26	7.83	20.33	6.87	4.88	27.45	8.20 (0.24)	9.35 (0.45)	16.95 (0.32)	10.26 (0.27)	4.87 (0.08)	5.29 (0.08)	2.35 (0.08)	2.12 (0.08)	
	ρ -0.5 Risk	0.26	0.32	0.26	0.84	0.24	0.16	0.87	0.51 (0.01)	0.45 (0.00)	0.94 (0.02)	0.46 (0.00)	0.26 (0.00)	0.24 (0.01)	0.16 (0.00)	0.16 (0.00)	
	ρ -0.9 Risk	0.34	0.42	0.3	0.8	0.26	0.19	1.04	0.39 (0.01)	0.41 (0.01)	0.83 (0.01)						

Table 11: Mean forecast performance (along with standard deviations) of the proposed and benchmark models on all six datasets for the medium-term forecast horizons (60-day/9-week/12-month). The **best** and **second best** results are highlighted.

Dataset	Metric	Temporal Models				Spatiotemporal Models				Probabilistic Models (Temporal & Spatiotemporal)				ST-Engression Models (Proposed)			
		LSTM	NHTS	TCN	Transformers	GSTAR	STARMA	STGCN	DeepAR	Prob-TF	Transformer	GpGp	DiffSTG	STESN	MVEN	GCEN	STEN
Japan TB	SMAPE	23.21	23.53	24	37.48	25.06	25.39	44.43	30.16 (0.29)	37.54 (0.17)	105.99 (4.92)	87.55 (0.99)	23.32 (0.09)	23.79 (0.11)	22.41 (0.11)	22.58 (0.09)	
	MAE	5.79	5.85	6.03	10.72	5.64	5.78	16.21	9.11 (0.14)	9.11 (0.14)	52.60 (7.44)	32.55 (0.57)	5.48 (0.01)	6.12 (0.03)	5.42 (0.02)	5.58 (0.02)	
	RMSE	9.35	6.98	7.19	12.03	8.49	8.76	27.94	15.23 (0.25)	19.42 (0.24)	63.08 (7.95)	40.37 (0.67)	8.29 (0.04)	10.20 (0.06)	8.39 (0.04)	9.29 (0.06)	
	MASE	0.67	0.64	0.65	1.11	0.65	0.67	1.87	1.05 (0.02)	1.31 (0.01)	6.08 (0.86)	3.76 (0.07)	0.63 (0.01)	0.71 (0.00)	0.63 (0.00)	0.64 (0.00)	
	RMSSE	0.7	0.6	0.62	0.98	0.63	0.65	2.08	1.13 (0.02)	1.44 (0.02)	4.69 (0.59)	3.00 (0.05)	0.62 (0.00)	0.76 (0.00)	0.60 (0.00)	0.69 (0.00)	
	Pinball-80	2	2.14	2.1	3.4	2.17	3.22	3.38	3.24 (0.03)	4.16 (0.06)	27.72 (1.97)	19.98 (0.16)	2.01 (0.01)	1.90 (0.01)	1.97 (0.01)	1.93 (0.01)	
	Pinball-95	1.55	1.75	1.64	2.42	1.85	3.38	1.01	1.16 (0.01)	1.42 (0.05)	11.10 (0.62)	8.40 (0.05)	1.37 (0.01)	0.82 (0.01)	1.07 (0.01)	0.92 (0.01)	
	ρ -0.5 Risk	0.18	0.18	0.19	0.33	0.17	0.18	0.5	0.28 (0.00)	0.35 (0.00)	1.65 (0.23)	1.03 (0.02)	0.17 (0.00)	0.19 (0.00)	0.17 (0.00)	0.17 (0.00)	
	ρ -0.9 Risk	0.11	0.12	0.11	0.17	0.12	0.21	0.11	0.12 (0.00)	0.15 (0.00)	1.12 (0.07)	0.84 (0.01)	0.09 (0.00)	0.08 (0.00)	0.09 (0.00)	0.08 (0.00)	
	CRPS	5.79	5.85	6.03	10.72	5.64	5.78	16.21	6.35 (0.10)	8.07 (0.05)	39.05 (3.07)	27.88 (0.20)	4.78 (0.01)	5.10 (0.02)	4.44 (0.01)	4.46 (0.02)	
	Winkler Score	-	-	-	-	-	-	-	53.84 (1.40)	68.41 (1.54)	431.31 (18.03)	344.98 (1.90)	141.29 (0.94)	119.69 (1.18)	97.62 (1.23)	86.96 (1.11)	
China TB	SMAPE	14.96	12.91	15.29	31.01	12.3	29.03	19.39	17.11 (0.14)	122.25 (0.24)	64.06 (0.94)	65.28 (0.66)	15.35 (0.02)	15.51 (0.11)	16.72 (0.07)	17.04 (0.07)	
	MAE	350.56	328.93	368.59	544.52	320.86	601.67	486.08	405.15 (4.61)	1884.40 (1.56)	1269.76 (17.41)	1370.15 (16.83)	363.11 (0.63)	359.42 (1.98)	415.46 (1.95)	404.03 (1.84)	
	RMSE	728.07	440.73	450.99	625.19	451.75	963.32	1226.49	718.91 (5.83)	2470.48 (1.30)	1705.62 (25.34)	1728.10 (17.30)	666.15 (0.61)	743.89 (4.21)	932.84 (5.01)	812.76 (5.40)	
	MASE	1.49	1.21	1.42	2.19	1.36	2.56	2.06	1.72 (0.02)	5.39 (0.07)	5.82 (0.07)	5.82 (0.07)	1.54 (0.00)	1.59 (0.01)	1.76 (0.01)	1.72 (0.01)	
	RMSSE	0.82	1.05	1.22	1.74	1.07	1.08	1.38	0.81 (0.01)	2.78 (0.00)	1.94 (0.03)	1.94 (0.02)	0.75 (0.00)	0.81 (0.02)	1.05 (0.01)	0.91 (0.01)	
	Pinball-80	168.19	151.57	161.44	351.68	139.57	437.17	206.25	173.31 (1.70)	1339.22 (1.72)	517.96 (5.73)	622.62 (7.29)	158.26 (0.51)	157.36 (1.26)	167.72 (0.68)	162.49 (1.11)	
	Pinball-95	164.64	145.13	150.02	391.38	129.13	505.34	187.85	99.45 (1.58)	1301.16 (7.28)	220.75 (4.28)	256.89 (3.50)	135.32 (1.06)	112.32 (1.64)	123.15 (0.84)	112.83 (1.23)	
	ρ -0.5 Risk	0.16	0.15	0.17	0.25	0.14	0.27	0.22	0.18 (0.00)	0.85 (0.00)	0.57 (0.01)	0.62 (0.01)	0.16 (0.00)	0.15 (0.01)	0.19 (0.00)	0.18 (0.00)	
	ρ -0.9 Risk	0.15	0.13	0.14	0.34	0.12	0.44	0.18	0.13 (0.01)	1.24 (0.00)	0.32 (0.00)	0.38 (0.00)	0.13 (0.00)	0.12 (0.00)	0.13 (0.00)	0.12 (0.00)	
	CRPS	350.56	328.93	368.59	544.52	320.86	601.67	486.08	325.87 (2.12)	1704.94 (2.42)	955.18 (10.12)	1062.12 (7.25)	343.40 (1.13)	304.76 (1.32)	361.44 (1.71)	377.77 (2.7)	
	Winkler Score	-	-	-	-	-	-	-	5154.01 (86.01)	4833.51 (542.86)	9957.39 (193.71)	11358.48 (112.90)	11485.91 (175.47)	7294.79 (70.38)	9992.48 (157.22)	8795.67 (202.00)	
USA ILI	SMAPE	38.34	54.78	50.95	58.12	63.11	44.55	60.53	75.56 (1.77)	66.40 (0.43)	105.39 (1.57)	96.98 (1.40)	38.6 (0.09)	38.47 (0.41)	39.50 (0.27)	38.90 (0.28)	
	MAE	73.44	124.71	116.66	153.91	142.27	119.11	128.19	168.66 (2.93)	228.69 (0.53)	320.74 (4.45)	262.60 (2.89)	74.26 (0.32)	97.08 (1.78)	75.29 (0.98)	72.27 (1.62)	
	RMSE	142.72	137.44	131.24	170.97	260.38	266.33	255.1	348.57 (5.33)	511.10 (0.76)	528.00 (3.44)	495.49 (3.09)	143.65 (0.84)	223.87 (4.85)	135.37 (2.96)	131.13 (4.77)	
	MASE	1.96	3.24	2.97	3.39	3.8	3.18	3.42	4.51 (0.08)	6.11 (0.01)	8.57 (0.12)	7.02 (0.08)	1.98 (0.01)	2.59 (0.05)	2.01 (0.03)	1.93 (0.04)	
	RMSSE	1.38	2.12	2.03	2.25	2.51	2.57	2.46	3.37 (0.05)	4.93 (0.01)	5.10 (0.03)	4.78 (0.03)	1.39 (0.01)	2.15 (0.05)	1.31 (0.03)	1.27 (0.05)	
	Pinball-80	39.26	61.72	54.71	112.39	112.83	90.31	80.83	97.27 (3.17)	144.17 (0.54)	172.47 (1.44)	152.81 (1.31)	34.11 (0.22)	47.02 (0.78)	30.64 (0.35)	30.64 (0.35)	
	Pinball-95	40.53	61.41	52.9	130.11	133.67	105.69	89.2	73.74 (5.51)	123.24 (1.50)	99.21 (1.40)	91.30 (1.83)	28.59 (0.38)	35.85 (0.86)	18.09 (0.34)	18.00 (0.21)	
	ρ -0.5 Risk	0.23	0.39	0.37	0.49	0.45	0.38	0.4	0.53 (0.01)	0.72 (0.00)	1.02 (0.01)	0.83 (0.01)	0.24 (0.01)	0.31 (0.01)	0.24 (0.00)	0.23 (0.01)	
	ρ -0.9 Risk	0.25	0.39	0.34	0.78	0.8	0.65	0.55	0.55 (0.03)	0.87 (0.01)	0.84 (0.01)	0.77 (0.01)	0.19 (0.00)	0.26 (0.01)	0.15 (0.00)	0.15 (0.00)	
	CRPS	73.44	124.71	116.66	153.91	142.27	119.11	128.19	136.72 (3.38)	197.32 (0.57)	270.35 (1.82)	226.45 (1.39)	67.18 (0.34)	75.62 (0.93)	56.67 (0.59)	55.72 (0.75)	
	Winkler Score	-	-	-	-	-	-	-	2720.32 (257.44)	4689.32 (90.29)	4439.78 (60.03)	3568.76 (72.75)	2105.99 (24.57)	1432.37 (32.92)	794.90 (20.31)	879.44 (15.03)	
Belgium COVID-19	SMAPE	64.04	75.63	106.21	123.67	123.5	135.81	121.83	84.02 (0.89)	75.77 (0.32)	145.07 (21.67)	120.62 (0.97)	65.99 (0.06)	67.43 (0.67)	57.10 (0.42)	70.99 (0.09)	
	MAE	69.87	103.86	111.21	418.62	291.7	123.68	366.12	94.18 (0.63)	91.53 (0.52)	262.35 (61.50)	302.94 (5.99)	69.07 (0.07)	77.55 (0.47)	58.29 (0.42)	87.54 (0.13)	
	RMSE	100.37	121.33	145.81	439.21	419.51	186.89	424.76	141.92 (1.25)	133.87 (0.71)	326.99 (69.11)	327.39 (6.13)	110.47 (0.10)	111.76 (0.62)	85.91 (0.55)	121.89 (0.11)	
	MASE	0.35	0.49	0.57	1.94	1.45	0.61	1.81	0.47 (0.00)	0.45 (0.00)	1.30 (0.30)	1.50 (0.03)	0.34 (0.00)	0.34 (0.02)	0.29 (0.00)	0.43 (0.00)	
	RMSSE	0.2	0.26	0.33	0.92	0.84	0.37	0.85	0.28 (0.00)	0.27 (0.00)	0.65 (0.14)	0.65 (0.01)	0.22 (0.00)	0.22 (0.00)	0.17 (0.00)	0.24 (0.00)	
	Pinball-80	27.02	24.25	71.26	84.04	87.61	96.08	74.05	44.83 (0.88)	39.70 (0.39)	354.73 (34.89)	124.04 (1.53)	36.10 (0.10)	29.79 (0.28)	23.97 (0.18)	37.72 (0.10)	
	Pinball-95	23.06	10.41	79.09	21.41	58.49	113.21	19.55	25.80 (1.68)	19.58 (0.47)	174.00 (11.56)	48.16 (0.54)	35.62 (0.18)	16.14 (0.25)	14.43 (0.27)	30.74 (0.22)	
	ρ -0.5 Risk	0.5	0.75	0.8	3.03	2.11	0.89	2.65	0.68 (0.00)	0.66 (0.00)	1.85 (0.42)	2.22 (0.04)	0.50 (0.00)	0.56 (0.00)	0.42 (0.00)	0.63 (0.00)	
	ρ -0.9 Risk	0.35	0.22	1.11	0.61	0.99	1.55	0.55	0.50 (0.02)	0.41 (0.01)	3.93 (0.29)	1.16 (0.01)	0.52 (0.00)	0.32 (0.00)	0.27 (0.00)	0.49 (0.00)	
	CRPS	69.87	103.86	111.21	418.62	291.7	123.68	366.12	70.40 (0.89)	69.08 (0.34)	533.06 (23.97)	201.96 (3.61)	66.80 (0.09)	61.99 (0.33)	48.13 (0.25)	81.24 (0.15)	
	Winkler Score	-	-	-	-	-	-	-	913.66 (77.80)	993.36 (21.10)	8312.55 (369.09)	1362.17 (15.46)	2481.60 (9.53)	1229.14 (18.58)	979.99 (26.68)	2708.76 (17.32)	
Colombia Dengue	SMAPE	37.06	54.03	74.49	75.94	44.15	37.83	76.53	56.30 (0.68)	38.03 (0.51)	105.81 (2.21)	65.02 (0.87)	54.14 (0.82)	39.14 (1.56)	37.01 (1.01)	39.07 (1.32)	
	MAE	13.1	26.35	26.53	42.55	17.87	14.03	40.69	24.94 (0.28)	24.20 (0.16)	45.31 (0.63)	27.77 (0.25)	16.36 (0.10)	16.35 (0.27)	15.86 (0.18)	15.79 (0.16)	
	RMSE	31.16	28.18	28.8	43.84	46.27	33.12	83.37	58.37 (0.63)	74.15 (0.43)	92.72 (0.73)	73.00 (0.46)	29.37 (0.20)	43.26 (0.78)	43.08 (0.79)	43.56 (0.56)	
	MASE	1.78	3.05	3.24	4.51	2.43	1.9	5.52	3.38 (0.04)	3.28 (0.02)	6.15 (0.09)	3.77 (0.03)	2.22 (0.01)	2.22 (0.04)	2.15 (0.02)	2.14 (0.02)	
	RMSSE	2.05	1.99	2.15	2.81	3.04	2.17	5.47	3.83 (0.04)	4.87 (0.03)	6.09 (0.05)	4.79 (0.03)	1.93 (0.01)	2.84 (0.05)	2.83 (0.05)	2.86 (0.04)	
	Pinball-80	9.32	16.25	19.61	22.58	12.21	8.87	22.18	12.42 (0.19)	12.43 (0.15)	24.79 (0.21)	16.30 (0.19)	7.91 (0.07)	7.89 (0.23)	8.33 (0.24)	8.33 (0.13)	
	Pinball-95	10.7	17.76	22.78	23.24	13.85	9.8	23.1	8.70 (0.25)	9.21 (0.41)	16.13 (0.20)	15.62 (0.29)	6.62 (0.09)	5.39 (0.26)	6.22 (0.28)	6.85 (0.23)	
	ρ -0.5 Risk	0.26	0.52	0.52	0.84	0.35	0.28	0.8	0.49 (0.01)	0.47 (0.00)	0.89 (0.01)	0.55 (0.00)	0.32 (0.00)	0.32 (0.01)	0.31 (0.00)	0.31 (0.00)	
	ρ -0.9 Risk	0.4	0.68	0.86	0.91	0.53</											

Table 12: Mean forecast performance (along with standard deviations) of the proposed and benchmark models on all six datasets for the long-term forecast horizons (90-day/13-week/24-month). The **best** and **second best** results are highlighted.

Dataset	Metric	Temporal Models			Spatiotemporal Models				Probabilistic Models (Temporal & Spatiotemporal)				ST-Egression Models (Proposed)			
		LSTM	NHITS	Transformers	TCN	GSTAR	STARMA	STGCN	DeepAR	Prob-iTransformer	GpGp	DiffSTG	STESN	MVEN	GCEN	STEN
Japan TB	SMAPE	25.37	23.88	19.06	27.81	26.33	26.33	39.24	30.79 (0.24)	47.01 (0.12)	125.67 (5.23)	92.02 (0.69)	23.16 (0.03)	23.24 (0.06)	22.38 (0.06)	22.45 (0.04)
	MAE	7.54	6.72	475.54	578.56	6.58	6.07	14.54	9.91 (0.10)	15.40 (0.88)	106.12 (14.70)	36.54 (0.39)	6.09 (0.01)	6.37 (0.03)	5.99 (0.02)	6.00 (0.01)
	RMSE	13.04	8.06	516.28	618.39	10.31	9.21	27.57	16.51 (0.18)	24.11 (0.18)	127.24 (16.56)	45.95 (0.40)	10.31 (0.02)	11.01 (0.07)	10.51 (0.05)	10.45 (0.03)
	MASE	0.86	0.68	1.66	2.18	0.75	0.69	1.66	1.13 (0.01)	1.76 (0.01)	12.12 (1.68)	4.17 (0.04)	0.70 (0.00)	0.74 (0.00)	0.69 (0.01)	0.70 (0.00)
	RMSSE	0.96	0.65	1.28	1.66	0.76	0.68	2.03	1.21 (0.01)	1.77 (0.01)	9.35 (1.22)	3.38 (0.03)	0.76 (0.00)	0.82 (0.01)	0.79 (0.00)	0.78 (0.00)
	PInball-80	1.04	1.99	168.98	295.54	2.26	3.38	3.38	3.44 (0.03)	5.55 (0.04)	48.96 (3.26)	22.86 (0.12)	2.11 (0.01)	1.94 (0.01)	2.05 (0.01)	2.11 (0.01)
	PInball-95	1.03	1.31	134.59	295.67	1.74	3.55	1.43	1.21 (0.01)	1.86 (0.05)	18.74 (1.08)	9.45 (0.05)	1.48 (0.01)	0.97 (0.01)	1.06 (0.01)	1.08 (0.02)
	$\rho=0.5$ Risk	0.22	0.2	0.19	0.36	0.2	0.18	0.43	0.30 (0.00)	0.46 (0.00)	3.21 (0.44)	1.11 (0.01)	0.18 (0.00)	0.19 (0.00)	0.18 (0.00)	0.18 (0.00)
	$\rho=0.9$ Risk	0.08	0.09	0.14	0.1	0.11	0.21	0.12	0.13 (0.00)	0.20 (0.00)	1.87 (0.11)	0.93 (0.00)	0.09 (0.00)	0.08 (0.00)	0.08 (0.01)	0.09 (0.00)
	CRPS	7.54	6.72	475.54	578.56	6.58	6.07	14.54	6.97 (0.07)	11.15 (0.05)	70.39 (6.79)	32.04 (0.13)	5.78 (0.01)	5.69 (0.02)	5.08 (0.01)	5.36 (0.01)
	Winkler Score	-	-	-	-	-	-	-	61.03 (1.28)	103.48 (1.42)	650.09 (41.34)	395.52 (1.72)	205.30 (0.87)	169.59 (1.18)	129.10 (0.61)	157.69 (0.93)
USA ILI	SMAPE	41.72	50.84	53.97	60.72	104.89	52.87	52.22	86.24 (1.40)	70.79 (0.28)	106.61 (1.56)	95.28 (1.09)	43.33 (0.18)	48.66 (0.49)	43.92 (0.22)	41.56 (0.30)
	MAE	73.2	102.91	104.94	146.24	179.33	136.7	115.36	173.18 (1.62)	208.71 (0.34)	283.65 (5.44)	237.80 (2.72)	89.42 (0.47)	110.15 (1.27)	70.39 (0.70)	65.88 (0.90)
	RMSE	149.72	118.53	121.45	160.45	322.39	303.15	249.15	361.28 (2.54)	466.74 (0.55)	473.18 (3.14)	435.99 (2.37)	186.83 (0.99)	250.69 (3.42)	124.26 (1.80)	119.07 (1.70)
	MASE	1.95	2.69	2.57	3.44	4.77	3.64	3.07	4.61 (0.04)	5.55 (0.01)	7.54 (0.14)	6.32 (0.07)	2.38 (0.01)	2.93 (0.03)	1.87 (0.02)	1.75 (0.02)
	RMSSE	1.44	1.84	1.78	2.25	3.1	2.91	2.39	3.47 (0.02)	4.48 (0.01)	4.54 (0.03)	4.19 (0.02)	1.79 (0.01)	2.41 (0.03)	1.19 (0.02)	1.14 (0.02)
	PInball-80	42.27	56.45	74.36	77.85	143.22	106.23	76.91	113.00 (1.67)	131.98 (0.41)	161.14 (1.60)	135.38 (1.07)	40.23 (0.24)	54.30 (1.21)	29.62 (0.34)	29.33 (0.34)
	PInball-95	45.1	58.94	85.3	80.21	170	125.17	86.53	105.51 (2.92)	112.02 (1.15)	85.77 (0.85)	82.06 (1.17)	33.95 (0.41)	38.19 (1.37)	17.44 (0.38)	18.96 (0.20)
	$\rho=0.5$ Risk	0.26	0.36	0.37	0.51	0.63	0.48	0.4	0.60 (0.01)	0.73 (0.00)	1.00 (0.02)	0.83 (0.01)	0.31 (0.00)	0.38 (0.00)	0.25 (0.00)	0.23 (0.00)
	$\rho=0.9$ Risk	0.31	0.41	0.57	0.55	1.12	0.83	0.58	0.78 (0.02)	0.88 (0.01)	0.85 (0.01)	0.76 (0.01)	0.25 (0.00)	0.32 (0.01)	0.16 (0.00)	0.16 (0.00)
	CRPS	73.2	102.91	104.94	146.24	179.34	136.7	115.36	151.28 (1.97)	179.31 (0.44)	245.18 (1.61)	193.91 (1.30)	81.79 (0.48)	84.32 (1.07)	57.76 (0.47)	53.17 (0.50)
	Winkler Score	-	-	-	-	-	-	-	41.38 (05 (162.95)	421.21 (76.86)	3596.55 (47.90)	3088.02 (51.80)	2636.71 (36.95)	1504.60 (47.28)	957.69 (18.21)	1039.84 (16.75)
Belgium COVID-19	SMAPE	101.51	90.45	119.99	127.66	96.48	163.31	121.48	82.84 (2.14)	77.40 (0.27)	151.75 (16.27)	122.36 (0.69)	67.17 (0.06)	69.29 (0.47)	69.72 (0.23)	81.37 (0.37)
	MAE	242.15	165.5	195.33	457.57	190.85	140.64	374.97	134.57 (9.08)	102.53 (0.45)	283.38 (68.24)	351.98 (5.25)	75.10 (0.15)	90.09 (0.88)	90.13 (0.48)	97.53 (0.50)
	RMSE	304.01	184.3	232.09	473.9	310.3	208.02	430.97	174.57 (10.21)	156.61 (0.66)	355.68 (73.95)	385.31 (5.34)	125.58 (0.12)	124.67 (1.14)	120.75 (0.59)	144.28 (0.48)
	MASE	1.18	0.78	0.95	2.13	0.93	0.68	1.82	0.65 (0.04)	0.50 (0.00)	1.38 (0.33)	1.71 (0.03)	0.38 (0.00)	0.44 (0.00)	0.40 (0.00)	0.47 (0.00)
	RMSSE	0.6	0.39	0.5	0.98	0.61	0.41	0.85	0.34 (0.02)	0.31 (0.00)	0.70 (0.15)	0.76 (0.01)	0.24 (0.00)	0.24 (0.00)	0.24 (0.00)	0.28 (0.00)
	PInball-80	51.44	38.71	90.45	91.94	50.08	112.27	75.92	86.29 (10.85)	47.01 (0.31)	347.10 (30.83)	175.37 (1.30)	38.19 (0.08)	31.39 (0.36)	30.76 (0.10)	40.45 (0.84)
	PInball-95	16.63	16.69	86.84	23.51	27.41	133.25	20.13	45.78 (2.93)	23.00 (0.46)	173.37 (9.59)	71.45 (0.43)	36.51 (0.17)	12.38 (0.36)	16.52 (0.16)	12.68 (0.69)
	$\rho=0.5$ Risk	1.6	1.09	1.29	3.03	1.26	0.93	2.48	0.90 (0.06)	0.68 (0.00)	1.81 (0.42)	2.37 (0.03)	0.52 (0.00)	0.60 (0.01)	0.60 (0.00)	0.65 (0.00)
	$\rho=0.9$ Risk	0.37	0.32	1.16	0.61	0.46	1.67	0.51	0.91 (0.08)	0.44 (0.00)	3.56 (0.22)	1.55 (0.01)	0.49 (0.00)	0.27 (0.00)	0.29 (0.00)	0.30 (0.02)
	CRPS	242.15	165.5	195.33	457.57	190.85	140.64	374.97	112.08 (9.24)	77.24 (0.33)	546.12 (23.61)	243.25 (2.53)	75.75 (0.17)	65.78 (0.62)	72.34 (0.47)	71.36 (0.69)
	Winkler Score	-	-	-	-	-	-	-	1324.40 (60.61)	1106.11 (23.78)	8465.70 (313.41)	2400.48 (13.87)	2830.95 (123.33)	713.64 (23.65)	1361.05 (21.84)	638.55 (29.30)
Colombia Dengue	SMAPE	40.68	61.2	68.89	78.16	44.21	44.77	47.49	59.61 (0.88)	42.11 (0.55)	107.44 (2.65)	62.59 (0.71)	55.56 (0.39)	41.78 (1.15)	42.06 (0.69)	47.54 (0.84)
	MAE	18.07	27.31	22.97	44.02	19.15	16.59	39.27	23.53 (0.20)	23.01 (0.20)	42.81 (0.42)	25.02 (0.23)	18.04 (0.10)	18.02 (0.28)	18.48 (0.22)	20.17 (0.36)
	RMSE	48.76	29.87	26.35	45.97	47.17	44.46	78.05	54.64 (0.63)	68.45 (0.37)	85.45 (0.71)	65.34 (0.46)	34.19 (0.21)	51.89 (0.48)	49.43 (0.55)	55.49 (1.09)
	MASE	2.45	3.3	2.92	4.59	2.6	2.25	5.33	3.19 (0.03)	3.12 (0.03)	5.81 (0.06)	3.39 (0.03)	2.46 (0.01)	2.45 (0.04)	2.50 (0.03)	2.74 (0.05)
	RMSSE	3.2	2.13	2.91	3.1	2.92	5.12	3.59 (0.04)	4.47 (0.02)	5.61 (0.05)	4.29 (0.03)	2.24 (0.01)	3.41 (0.03)	3.24 (0.02)	3.64 (0.07)	
	PInball-80	12.65	13.55	14.25	21.73	11.59	11.74	21.42	11.76 (0.20)	12.01 (0.13)	22.89 (0.22)	14.46 (0.16)	9.45 (0.08)	10.82 (0.18)	11.15 (0.11)	11.78 (0.14)
	PInball-95	14.45	13.2	15.64	21.59	12.59	13.46	22.31	8.22 (0.25)	8.24 (0.30)	14.41 (0.20)	11.86 (0.22)	3.51 (0.12)	8.20 (0.30)	9.93 (0.13)	11.15 (0.17)
	$\rho=0.5$ Risk	0.38	0.57	0.48	0.91	0.4	0.34	0.81	0.49 (0.00)	0.47 (0.00)	0.88 (0.01)	0.51 (0.00)	0.38 (0.01)	0.39 (0.01)	0.38 (0.00)	0.42 (0.01)
	$\rho=0.9$ Risk	0.57	0.55	0.63	0.9	0.51	0.53	0.91	0.41 (0.01)	0.42 (0.01)	0.76 (0.01)	0.54 (0.01)	0.36 (0.00)	0.41 (0.01)	0.44 (0.00)	0.48 (0.01)
	CRPS	18.07	27.31	22.97	44.02	19.15	16.59	39.27	18.49 (0.19)	18.91 (0.12)	38.18 (0.29)	20.65 (0.18)	16.12 (0.11)	15.62 (0.20)	18.88 (0.12)	17.22 (0.18)
	Winkler Score	-	-	-	-	-	-	-	308.33 (11.06)	332.72 (18.32)	627.78 (9.30)	463.00 (9.97)	491.81 (6.12)	346.33 (12.66)	412.48 (5.31)	459.42 (6.81)
Hungary Chickenpox	SMAPE	86.76	92.3	98.06	104.74	136.13	107.16	103.33	93.02 (0.63)	84.54 (0.48)	99.63 (2.94)	107.29 (0.88)	96.69 (0.46)	83.83 (1.40)	83.40 (0.55)	82.74 (0.74)
	MAE	12.97	16.25	20.15	24.95	20.9	15.71	23.85	17.63 (0.36)	16.60 (0.08)	16.60 (0.30)	26.07 (0.37)	18.97 (0.06)	13.73 (0.13)	13.90 (0.10)	13.39 (0.09)
	RMSE	23.03	20.89	24.19	28.11	35.23	32.08	31.19	25.99 (0.42)	25.46 (0.19)	31.13 (0.41)	34.76 (0.36)	26.78 (0.05)	23.29 (0.11)	23.43 (0.12)	23.74 (0.07)
	MASE	0.67	0.82	1.02	1.23	1.08	0.81	1.23	0.91 (0.02)	0.70 (0.00)	0.86 (0.02)	1.35 (0.02)	0.98 (0.00)	0.71 (0.01)	0.72 (0.01)	0.69 (0.00)
	RMSSE	0.73	0.67	0.78	0.9	1.1	1	0.97	0.81 (0.01)	0.79 (0.01)	0.97 (0.01)	1.09 (0.01)	0.84 (0.00)	0.72 (0.00)	0.72 (0.00)	0.74 (0.00)
	PInball-80	6.78	6.62	6.33	7.34	12.45	12.18	6.8	7.14 (0.12)	6.29 (0.06)	9.43 (0.20)	12.53 (0.13)	6.68 (0.02)	5.70 (0.04)	5.93 (0.03)	6.13 (0.04)
	PInball-95	6.92	5.87	4.45	4.77	13.44	14.34	4.24	2.93 (0.10)	3.66 (0.14)	5.03 (0.10)	5.67 (0.08)	4.59 (0.03)	3.32 (0.05)	3.90 (0.08)	4.34 (0.07)
	$\rho=0.5$ Risk	0.66	0.83	1.03	1.28	1.07	0.81	1.22	0.91 (0.02)	0.69 (0.00)	0.84 (0.02)	1.34 (0.02)	0.97 (0.00)	0.71 (0.01)	0.71 (0.01)	0.69 (0.00)
	$\rho=0.9$ Risk	0.69	0.63	0.52	0.58	1.34	1.4	0.52	0.49 (0.01)	0.48 (0.01)	0.71 (0.01)	0.88 (0.01)	0.53 (0.00)			

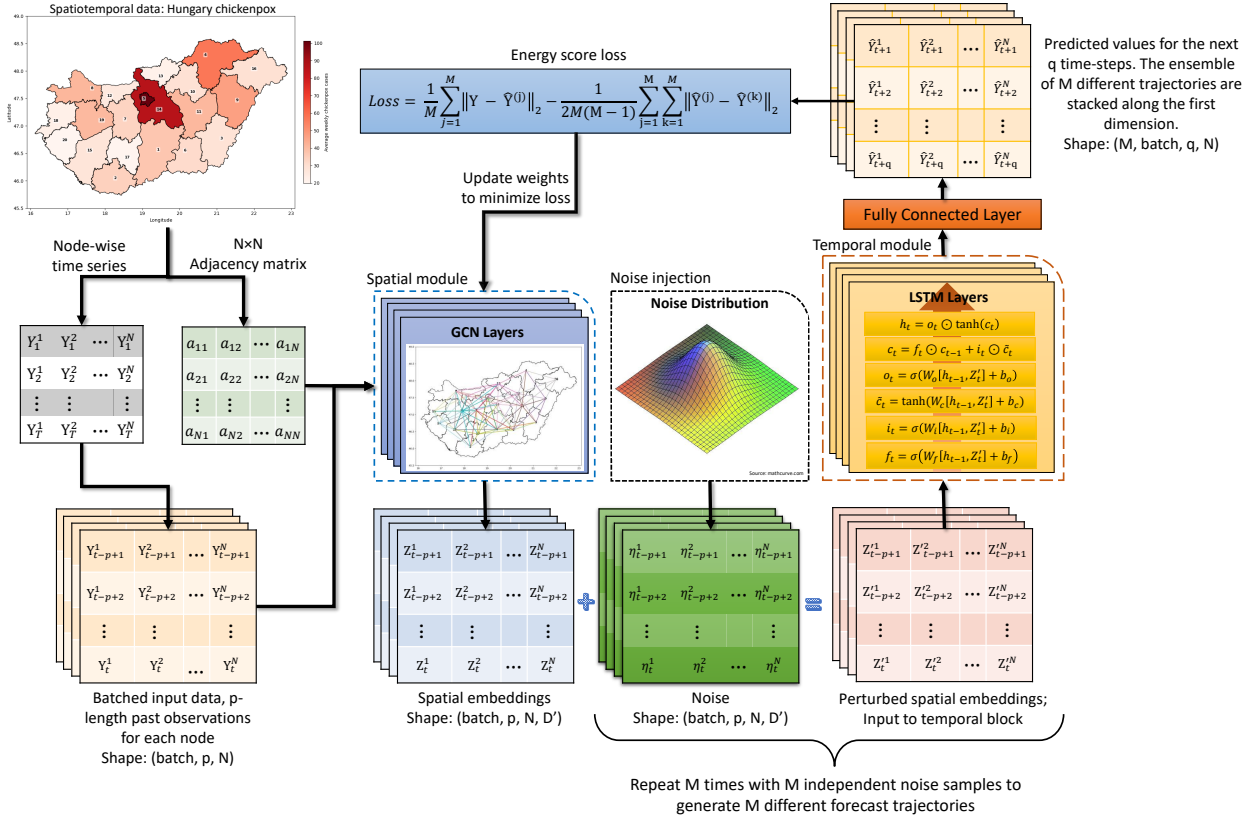


Fig. 13: A visual representation of the end-to-end training loop of the proposed GCEN architecture. Batches of input sequences along with the static adjacency matrix is first processed by the spatial module consisting of GCN layers to produce the spatial embeddings. Noise is sampled from a pre-determined distribution and added to the spatial embeddings, which are then passed to the temporal module consisting of LSTM layers, followed by a fully connected layer. The process is repeated with M independent noise samples to generate an ensemble of M forecasts for the next q time-steps for each node. The network is trained by minimizing the energy score loss function.

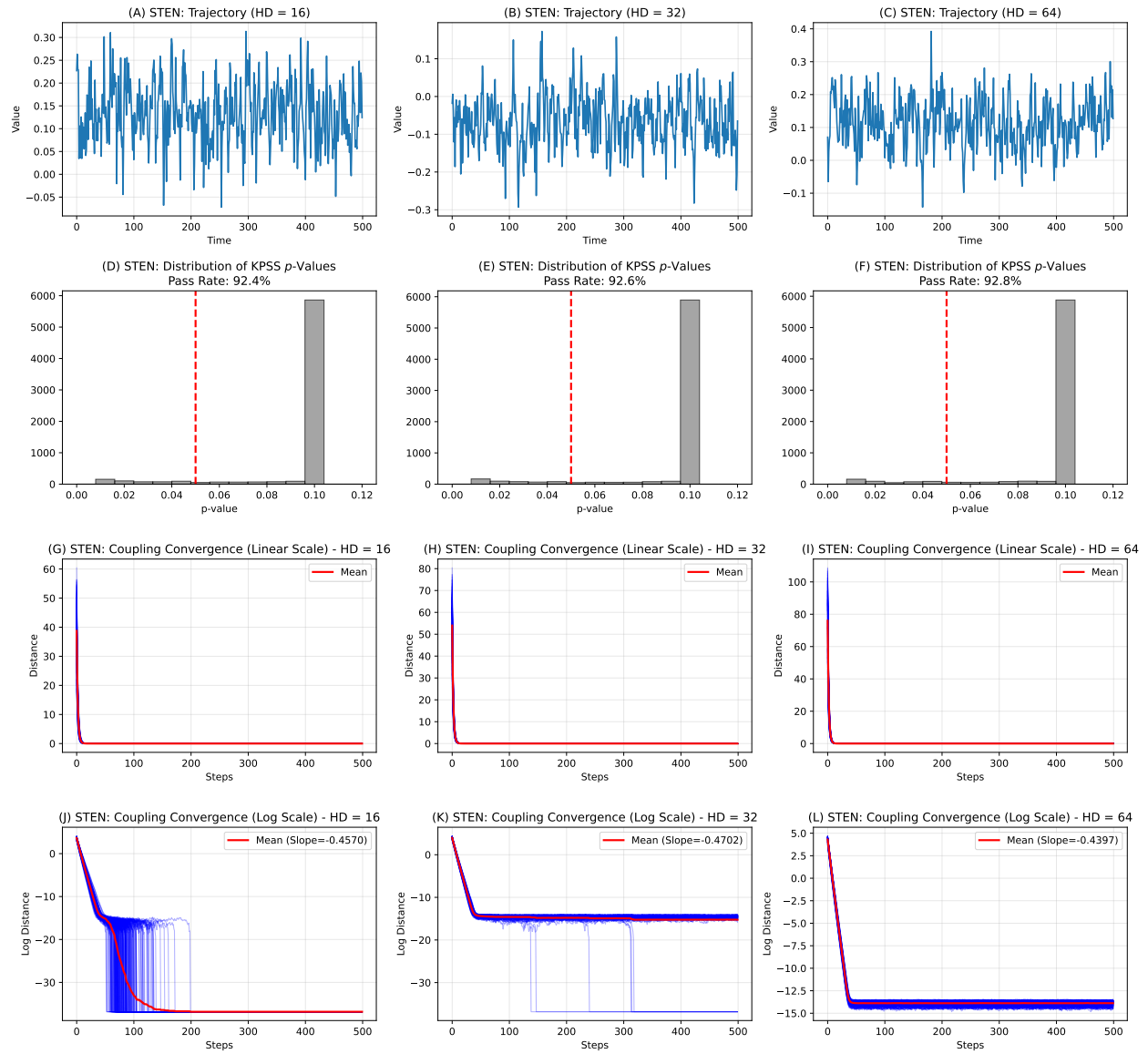


Fig. 14: Simulation results for STEN. For details, refer to Sec. 5.3.

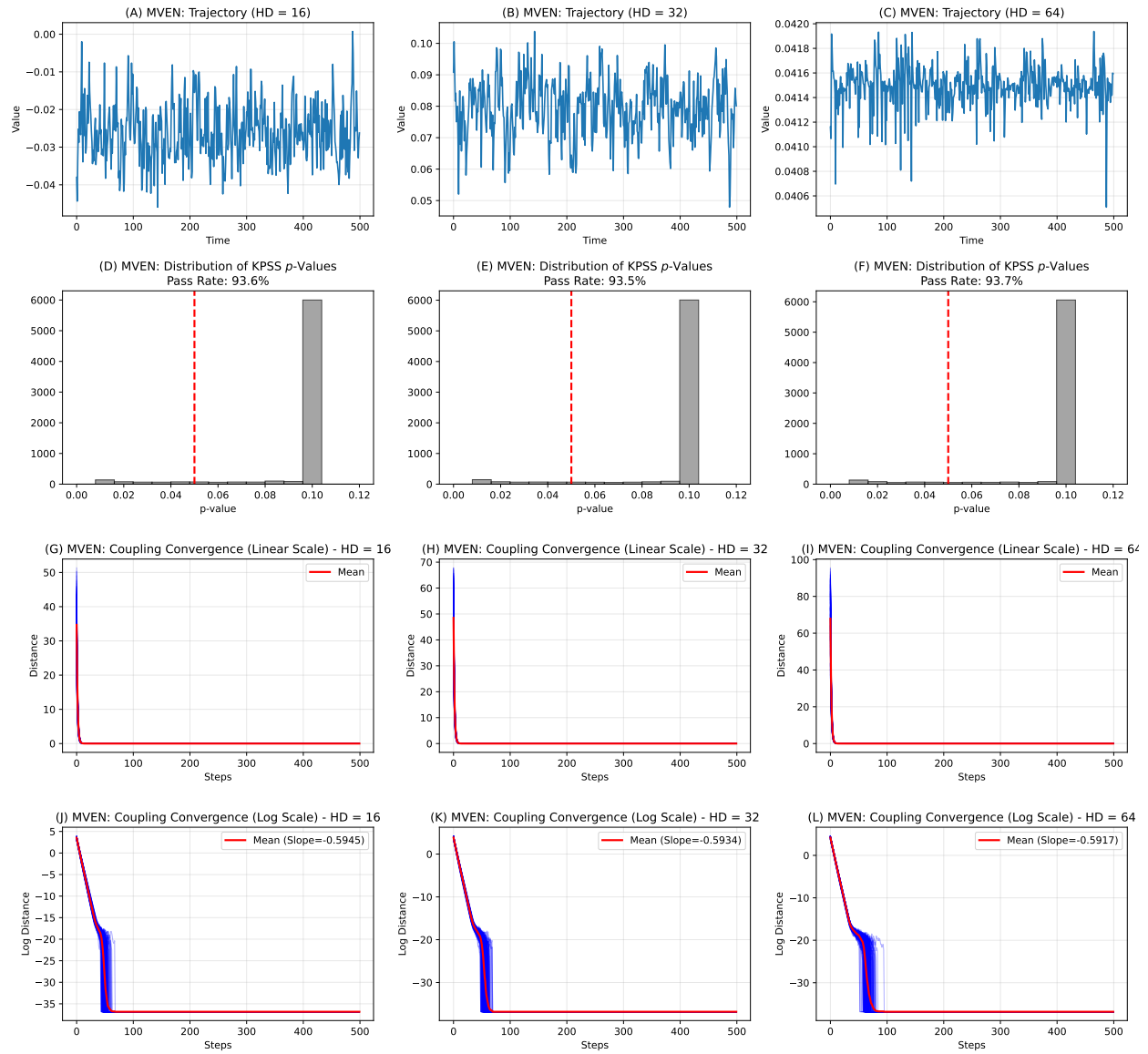


Fig. 15: Simulation results for MVEN. For details, refer to Sec. 5.3.

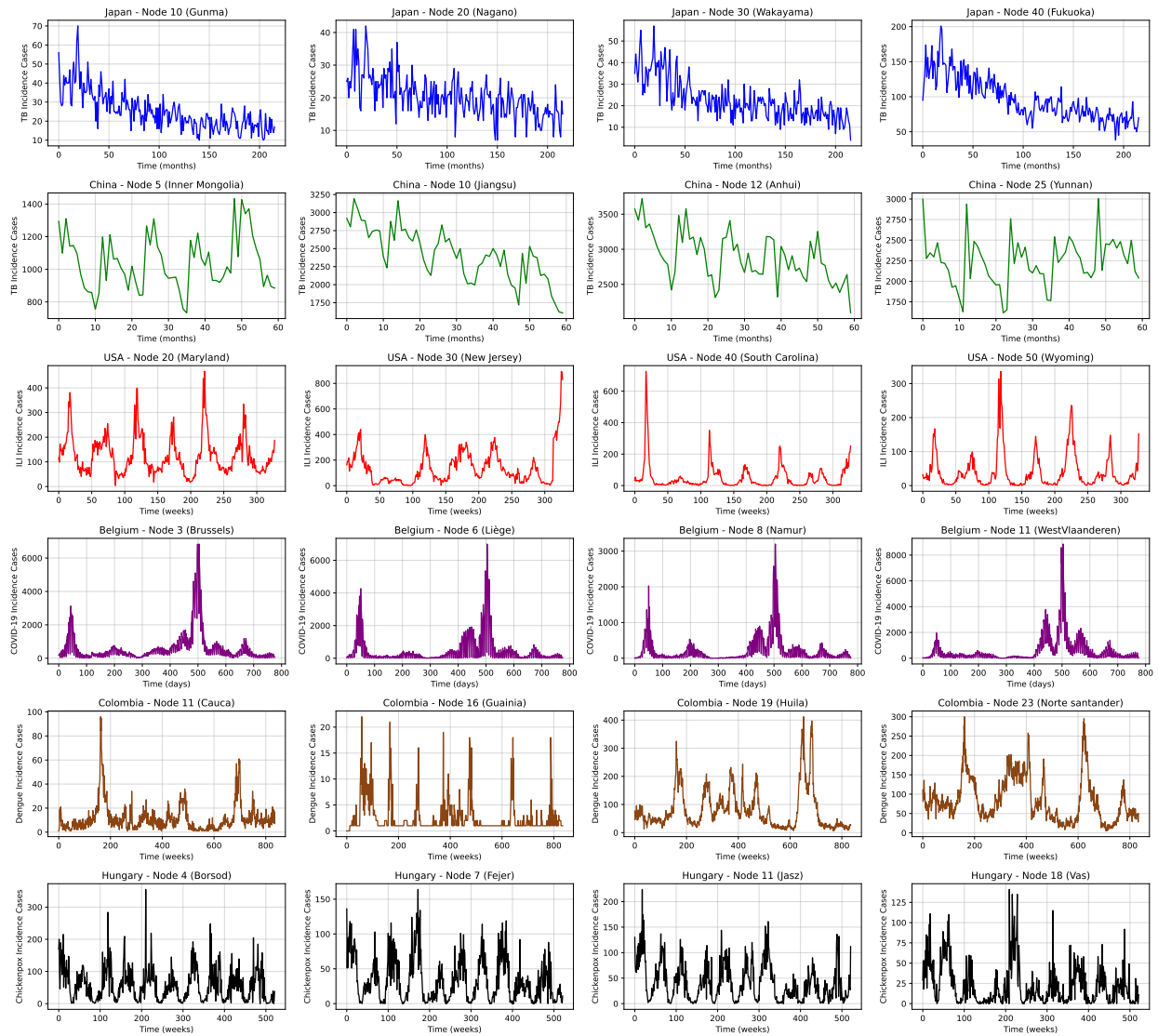


Fig. 16: Historical data of disease incidence for each dataset at the following nodes: Gunma, Nagano, Wakayama, and Fukuoka in Japan; Inner Mongolia, Jiangsu, Anhui, and Yunnan in China; Maryland, New Jersey, South Carolina, and Wyoming in USA; Brussels, Liège, Namur, and West Flanders in Belgium; Cauca, Guainia, Huila, and North Santander in Colombia; Borsod, Fejér, Jász, and Vas in Hungary.

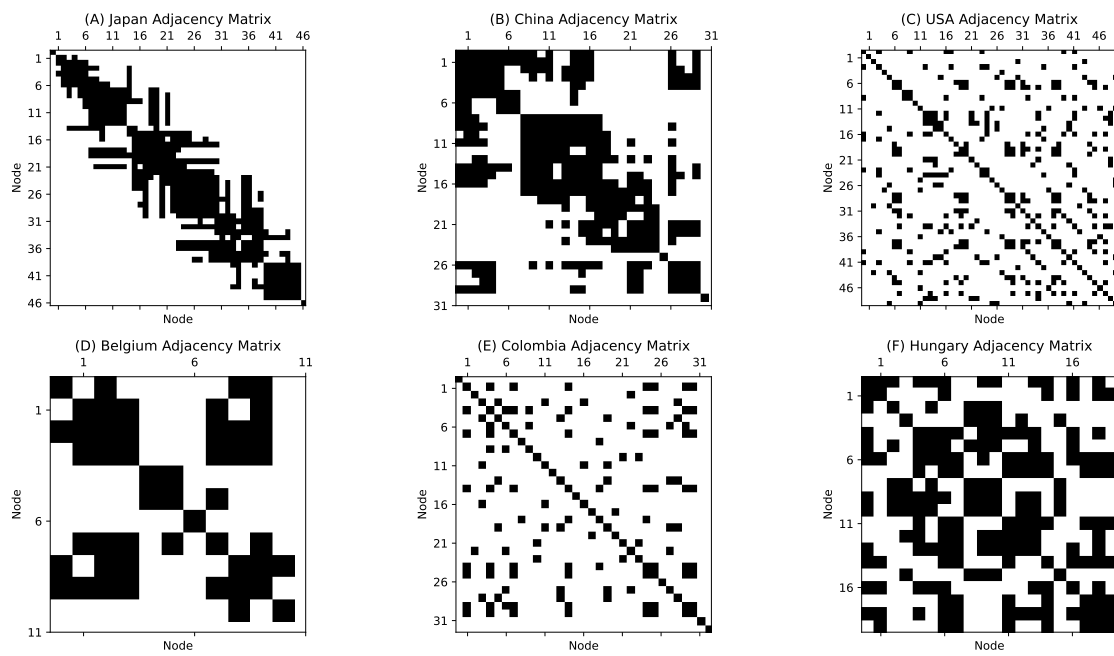


Fig. 17: Adjacency matrices of the countries, representing connectivity and structure of the nodes (states or provinces) used in training GCEN and DiffSTG.

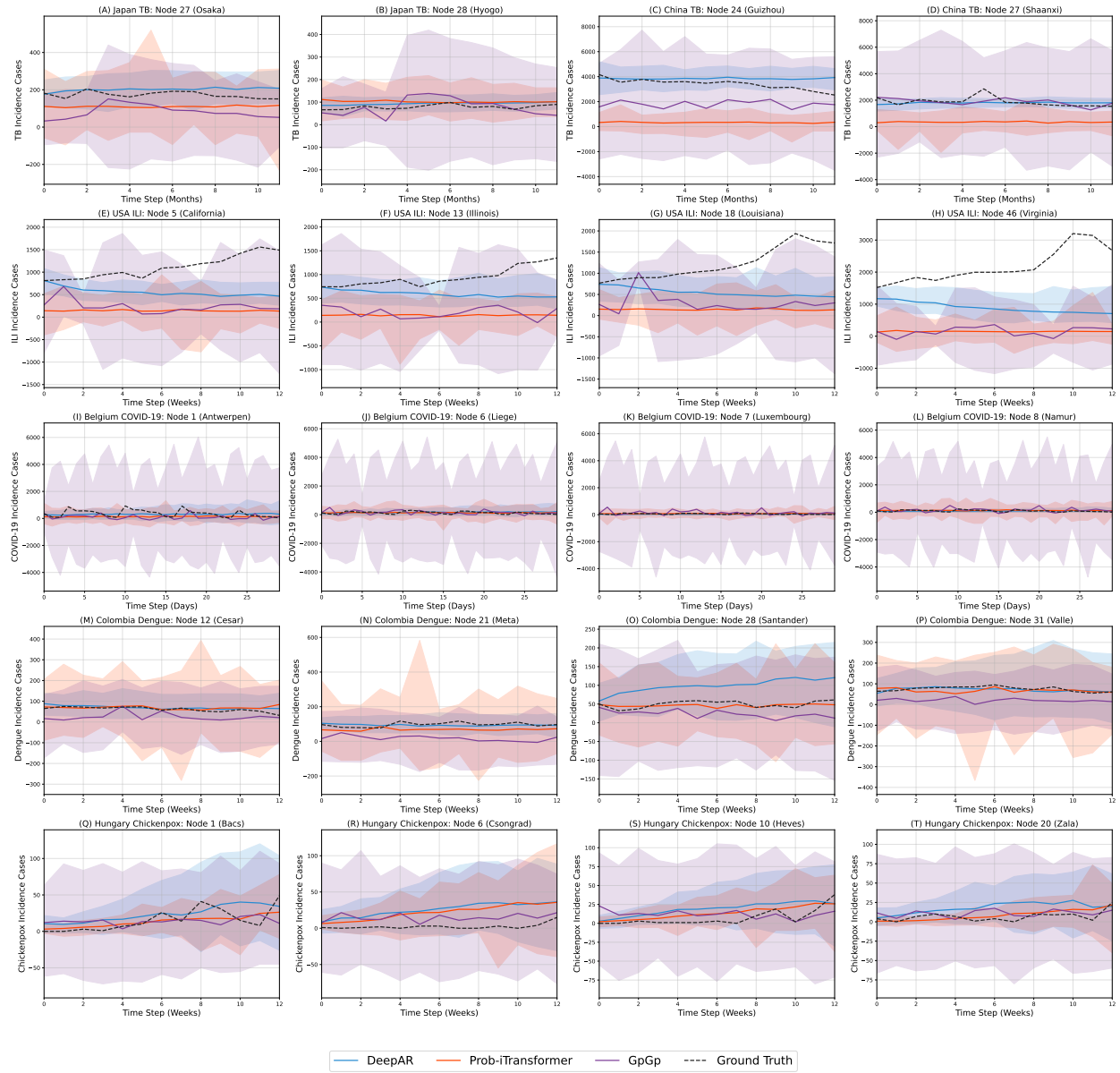


Fig. 18: Forecasts along with 95% PIs, produced by DeepAR, Prob-iTransformer, and GpGp on selected nodes (same as in Fig. 7) of the six datasets.